الجمهورية الجزائرية الديموقراطية الشعبية
République Algérienne Démocratique et Populaire
وزارة التعليم العالي والبحث العلمي
Ministère de l’enseignement supérieur et de la recherche scientifique

Université Mohamed Khider - Biskra
Faculté des Sciences et de la Technologie
Département de Génie Civil et Hydraulique
Référence: ………

جامعة محمد خيضر - بسكرة
كلية العلوم و التكنولوجيا
قسم الهندسة المدنية و الري
المرجع : ....

Thèse présentée en vue de l’obtention du diplôme de

Doctorat LMD en Travaux Publics

Option: Voies et Ouvrages d’art

Contribution à l'étude du comportement mécanique des structures courbées en matériaux avancés

Contribution to the study of the mechanical behavior of curved structures made of advanced materials

Présentée par

Soufiane BENOUNAS

Soutenue publiquement le **: 06/ 04/ 2025**

Devant le jury composé de :

Mr. Abdelouahab Tati	Professeur	Président	Université de Biskra
Mr. Mohamed-Ouejdi BELARBI	Professeur	Rapporteur	Université de Biskra
Mr. Mohamed Guenfoud	Professeur	Examinateur	Université de Guelma
Mr. Mohammed Sid Ahmed Houari	Professeur	Examinateur	Université de Mascara
Mr. Messaoud Bourezane	Professeur	Examinateur	Université de Biskra
Mr. Abdelhak Khechai	MCA	Examinateur	Université de Biskra

"One important idea is that science is a means whereby learning is achieved, not by mere theoretical speculation on the one hand, nor by the undirected accumulation of practical facts on the other, but rather by a motivated iteration between theory and practice."

George E. P. Box

Dedication

As Friedrich Nietzsche wisely stated:

"*In family life, love is the oil that eases friction, the cement that binds closer together, and the music that brings harmony.*"

To my beloved parents, *you are the driving force behind all my achievements. Your unwavering support has transformed my life into a beautiful journey. Thank you for the love, guidance, and wisdom you have shared with my brothers, my sister, and me. May God bless you with good health and keep you by our side throughout our lives.*

To my amazing siblings, *Youcef, Abdennour, and Safaa, I wish you boundless joy, good health, and remarkable success in all your pursuits.*

To my dear aunt *Prof. Naïma KHAZZER and* **her husband**, *Prof. Sadok BENMEBAREK, whose unwavering support has been instrumental in my education. Your guidance, encouragement, and kindness have made all the difference, and I am deeply grateful.*

To all my teachers and mentors*, from my first days in kindergarten to my doctoral studies, my success reflects your dedication and guidance.*

And to everyone *who has supported and encouraged me along this journey, thank you for believing in me.*

Acknowledgments

First and foremost, I express my heartfelt gratitude to the Almighty **ALLAH** for blessing me with the strength, wisdom, and resilience to comprehend, learn, and successfully complete this thesis. His guidance has been a constant source of inspiration and motivation throughout my academic journey, empowering me to overcome the many challenges I encountered along the way.

I want to extend my deepest appreciation to my thesis supervisor, **Mr. Mohamed Ouejdi BELARBI**, Associate Professor at Mohamed Khider University in Biskra. His guidance has been invaluable, consistently offering me not only technical insights but also encouragement that has sustained me in moments of doubt. Working under his supervision has not only enriched my scientific understanding but has also profoundly shaped my personal growth, inspiring me through his dedication, patience, and wisdom. I am truly grateful for all he has done, and I hold immense respect and admiration for him, both as a mentor and a trusted guide.

I am equally grateful to **Mr. Hicham HIRANE**, lecturer at Houari Boumediene University of Science and Technology, whose unwavering support and guidance have been a cornerstone of my research. His conscientious supervision, the autonomy he has granted me, and his consistent scientific and moral support have been crucial in helping me refine my work. I deeply appreciate the trust he has shown in my abilities and the encouragement he has provided, which have been instrumental in the smooth progression of my research.

I would also like to express my appreciation to my fellow PhD students, **Salah GUETTALA**, **Hamed Aboulkacem MOUTIE**, and **Akram KHELAIFIA**. Your support, collaboration, and shared insights have made this experience even more enriching. Thank you for being part of this journey with me.

Finally, I would like to express my sincere appreciation to **the jury members** for their gracious dedication of time and expertise in evaluating my work. Their insightful feedback, careful consideration, and high standards have not only enhanced the quality of my thesis but also honored me deeply. I am humbled by their involvement and am immensely grateful for their invaluable contributions, encouragement, and support throughout this journey.

Publications and Conferences contributions

- **International Publications (Classe A)**

1. **S. Benounas,** M. O. Belarbi, P. V. Vinh, A. A. Daikh, “Precise analysis of the static bending response of functionally graded doubly curved shallow shells via an improved finite element shear model”, *Engineering Structures*, **(2024)**, 319, 118829. https://doi.org/10.1016/j.engstruct.2024.118829 **IF: 5.6** **(Elsevier)**

2. **S. Benounas,** M. O. Belarbi, P. V. Vinh, A. A. Daikh, N. Fantuzzi, “Finite element model for free vibration analysis of functionally graded doubly curved shallow shells by using an improved first-order shear deformation theory”, *Structures*, **(2024)**, 64, 106594. https://doi.org/10.1016/j.istruc.2024.106594 **IF: 4.1** **(Elsevier)**

3. M. O. Belarbi, **S. Benounas,** A. Khechai, P. V. Vinh, L. T. Son, E. Ruocco, A. Garg, S. Gohari, " A comprehensive investigation of the bending and vibration behavior of size-dependent functionally graded nanoplates via an enhanced nonlocal finite element shear model”, *Mechanics Based Design Of Structures And Machines*, **(2024),** 1-40, https://doi.org/10.1080/15397734.2024.2366530. **IF: 3.9** **(Taylor & Francis)**

4. M. O. Belarbi, A. Karamanli, **S. Benounas,** A. A. Daikh, "Bending, free vibration and buckling finite element analysis of porous functionally graded plates with various porosity distributions using an improved FSDT”, *Mechanics Based Design Of Structures And Machines*, **(2024),** 1-45, https://doi.org/10.1080/15397734.2024.2366530. **IF: 3.9** **(Taylor & Francis)**

5. **S. Benounas,** M. O. Belarbi, S. J. Salami, A. Khechai, M. S. A. Houari, A. A. Daikh, “Finite element analysis of the free vibration characteristics of power-law, exponential, and sigmoid functionally graded plates under different boundary conditions and material grades’’ *Journal of Vibration Engineering & Technologies,* (2024), https://doi.org/10.1007/s42417-024-01696-3**.** **IF: 2.7** **(Springer)**

6. M. O. Belarbi, **S. Benounas**, L. Li, P.V. Vinh, A. Garg " Vibration of a functionally graded doubly curved shallow nanoshell: An improved FSDT model and its nonlocal finite element implement”, *Journal of Vibration Engineering & Technologies,* (2024), https://doi.org/10.1007/s42417-024-01733-1**.** **IF: 2.7** **(Springer)**

7. M. O. Belarbi**, S. Benounas**, S. J. Salami, A. Khechai, A. A. Daikh, M.S. A. Houari, S. Bezzina, “ An enhanced finite element model for static bending analysis of functionally graded plates with power-law, exponential, and sigmoid material gradients”, *Archive of*

Applied Mechanics, (2024), https://doi.org/10.1007/s00419-024-02727-x. **IF: 2.2 (Springer)**

International Conferences

1. **S. Benounas**, M. O. Belarbi, H. Hirane, "Bending analysis of functionally graded cylindrical shell under a uniform load", The Second Arab Conference on Mechanics and Engineering "ARCME'23", Biskra, Algeria, December 10-12, 2023.

2. **S. Benounas**, M. O. Belarbi, H. Hirane, "Buckling analysis of functionally graded plate using an improved first-order shear deformation theory", The Second Arab Conference on Mechanics and Engineering "ARCME'23", Biskra, Algeria, December 10-12, 2023.

3. **S. Benounas,** M. O. Belarbi, S. Guettala, "Free vibration analysis of functionally graded sandwich hyperbolic paraboloid shells with different boundary conditions", 4th International Conference on Innovative Academic Studies "ICIAS 2024", Konya, Turkey, March 12-13, 2024.

4. **S. Benounas**, M. O. Belarbi, "Free vibration analysis of functionally graded spherical shells with different boundary conditions", 3rd International Workshop on Structural Mechanics and Material "IWSMM'24", Batna, Algeria, April 23-24, 2024.

5. **S. Benounas**, M. O. Belarbi, "Free vibration analysis of functionally graded nanoplates", 4th International Conference on Scientific and Academic Research "ICSAR 2024", Konya, Turkey, July 19-20, 2024.

6. **S. Benounas**, M. O. Belarbi, "Bending analysis of functionally graded nanoplates", 4th International Conference on Scientific and Academic Research "ICSAR 2024", Konya, Turkey, July 19-20, 2024.

7. **S. Benounas**, M. O. Belarbi, "Bending analysis of functionally graded sandwich hyperbolic paraboloid shells with different boundary conditions", 4th International Conference on Scientific and Academic Research "ICSAR 2024", Konya, Turkey, July 19-20, 2024.

8. S. Guettala, **S. Benounas**, A. Khelaifia, "Seismic performance of infill walls: analyzing in-plane and out-of-plane behavior with advanced modeling techniques'', 3rd International Conference on Scientific and Innovative Studies "ICSIS 2024", Konya, Turkey, September 11-12, 2024

National Conferences

1. **S. Benounas**, M. O. Belarbi, H. Hirane, “The impact of porosity distribution on the bending of a porous functionally graded square plate under a uniform load”, 1st National Conference on Mechanics and Materials (CNMM2023), Boumerdes, Algeria, December 06-07, 2023.

2. **S. Benounas,** M. O. Belarbi, H. Hirane, “Free vibration analysis of power-law, exponential, and sigmoid functionally graded plates using an improved first-order shear deformation theory”, 2nd National Conference on Materials Sciences and Engineering (MSE’23), Maghnia, Algeria, December 12-13, 2023.

Abstract

Doubly curved shallow shells (DCSSs), frequently encountered in advanced engineering such as aerospace, civil, and mechanical engineering, present substantial challenges in predicting mechanical responses due to their complex geometry and material properties. Moreover, research on functionally graded doubly curved shallow shells (FG DCSs) is very limited, with most studies relying on analytical methods, highlighting the need for a novel and efficient approach to improve predictive analysis. Therefore, to address this gap, the aim of this research work is to develop an efficient and simple finite element model to investigate the bending deflection, stress distribution, and free vibration behavior of FG DCSSs. A new eight-node quadrilateral isoparametric element, named SQ8-IFSDT, with five degrees of freedom per node, is formulated based on improved first-order shear deformation theory (IFSDT). The present IFSDT simplifies the assumptions related to transverse shear stresses, replacing the conventional shear correction factor. As a result, it accurately predicts the parabolic shear stress distribution across the thickness of the shell while maintaining free traction conditions on both surfaces. In the present study, five types of DCSSs, namely flat plates, cylindrical shells, spherical shells, hyperbolic paraboloid shells, and elliptical paraboloid shells, are considered for the analysis. The material properties of FG DCSS change continuously across the thickness according to a power-law function. A variety of comparative studies is conducted to assess the accuracy and robustness of the developed finite element model. A comparison study shows that the proposed model is: (a) accurate and comparable with the literature; b) of fast rate of convergence to the reference solution; c) excellent in terms of numerical stability; and d) valid for both thin and thick FG DCSs. Moreover, comprehensive numerical results are presented and discussed in detail to examine the effects of material properties, power-law index, radius-to-thickness ratio, radius-to-side ratio, radii of curvature, loading, vibration modes, and boundary conditions on the bending and free vibration response of FG DCSSs. Finally, the outcomes of this research provide a robust benchmark for the design, testing, and manufacture of DCSSs and will inform future investigations into shell structures.

Keywords: Functionally graded materials, Bending, Free vibration, Curved shallow shells, Finite element model.

ملخص

تُعد القشور السطحية مزدوجة الانحناء (DCSSs)، التي تُستخدم بشكل شائع في الهندسة المتقدمة مثل هندسة الفضاء، والهندسة المدنية، والهندسة الميكانيكية، من الهياكل التي تشكل تحديات كبيرة في التنبؤ بالاستجابات الميكانيكية بسبب هندستها المعقدة وخصائص المواد التي تتكون منها. علاوة على ذلك، فإن البحوث حول القشور السطحية مزدوجة الانحناء ذات التدرج الوظيفي (FG DCSs) محدود للغاية، حيث تعتمد معظم الدراسات على الأساليب التحليلية، مما يبرز الحاجة إلى نهج جديد وفعال لتحسين التنبؤ بالتحليل. لذلك، يهدف هذا البحث إلى تطوير نموذج عنصر محدود بسيط وفعال للتحقيق في انحراف الانحناء، وتوزيع الإجهادات، وسلوك الاهتزاز الحر للـ FG DCSSs. تم صياغة عنصر رباعي الأضلاع مكون من ثمانية عقد، يسمىSQ8-IFSDT ، مع خمسة درجات من الحرية لكل عقدة استنادًا إلى نظرية التشوه القصي من الدرجة الأولى المحسنة (IFSDT). تقوم الـ IFSDT الحالية بتبسيط الافتراضات المتعلقة بالإجهادات القصية العرضية، حيث تستبدل معامل تصحيح القص التقليدي. ونتيجة لذلك، يتنبأ النموذج بدقة بتوزيع الإجهادات القصية التربيعية عبر سمك القشرة مع الحفاظ على ظروف الشد الحرة على كلا السطحين. في هذه الدراسة، تم اعتبار خمسة أنواع من الـ DCSSs للتحليل، وهي الألواح المسطحة، والقشور الأسطوانية، والقشور الكروية، والقشور الزائدية المفرطحة، والقشور البيضاوية المفرطحة. تتغير خصائص المواد لـ FG DCSS بشكل مستمر عبر السمك وفقًا لدالة القوة. تم إجراء مجموعة متنوعة من الدراسات المقارنة لتقييم دقة وقوة النموذج الذي تم تطويره. تُظهر دراسة المقارنة أن النموذج المقترح: (أ) دقيق وقابل للمقارنة مع المراجع؛ (ب) يتمتع بسرعة تقارب عالية نحو الحل المرجعي؛ (ج) ممتاز من حيث الاستقرار العددي؛ (د) صالح لكل من الـ FG DCSs الرقيقة والسميكة. علاوة على ذلك، تم تقديم ومناقشة نتائج عددية شاملة بالتفصيل لدراسة تأثيرات خصائص المواد، ومعامل القوة، ونسبة نصف القطر إلى السمك، ونسبة نصف القطر إلى الجانب، وأنصاف أقطار الانحناء، والأحمال، وأنماط الاهتزاز، والظروف الحدية على استجابة الانحناء والاهتزاز الحر لـ FG DCSSs. أخيرًا، توفر نتائج هذا البحث معيارًا قويًا لتصميم واختبار وتصنيع الـDCSSs ، وستسهم في الدراسات المستقبلية المتعلقة بالهياكل القشرية.

الكلمات المفتاحية: المواد المتدرجة وظيفيًا، الانحناء، الاهتزاز الحر، القشرور السطحية المنحنية، نموذج عنصر محدود.

Table of contents

List of Figures

List of Tables

List of Symbols

A	Surface of the structure.
a, b	Length and width of the DCS.
$[A]$, $[B]$, $[D]$, $[S]$	Membrane, Coupling, Bending, and Shear matrices, respectively.
A_{ij}, B_{ij}, D_{ij}, S_{ij}	Reduced elastic matrix coefficients.
$[B_m]$, $[B_b]$, $[B_s]$	Strain-displacement matrices for membrane, bending, and shear strains, respectively.
E	Young's modulus.
E_c, E_m	Young's modulus of ceramic and metal, respectively.
$\{d\}^e$	Displacement vector of the element.
$\{d\}$	The global displacement vector.
$f(z)$	Shear function.
$g(z)$	The derivative of the shear function.
h	The thickness of the structure.
I	The moment of inertia.
I_k	The inertia matrix.
J	Jacobian matrix.
J_{11}, J_{12}, J_{21}, J_{22}	Components of the Jacobian matrix.
$J_{11}^*, J_{12}^*, J_{21}^*, J_{22}^*$	Components of the inverse Jacobian matrix.

k	Power-law and Sigmoid-law index.
k_s	Shear correction factor.
$[K]^e$	The element elastic stiffness matrix.
$[K]$	The global stiffness matrix.
$\{f\}^e$	Element force vector.
$\{f\}$	The global force vector.
$[M]^e$	The element mass matrix.
$[M]$	The global mass matrix.
N_i, M_i, Q_i	Axial force, Bending moment, and Shear force.
$[N]$	The shape function matrix.
N_i	Lagrange shape function associated with node i.
N_w	The external force matrix.
n	Exponential-law index.
$P(z)$	The effective property.
P_c, P_m	The properties of the ceramic and metal, respectively.
q	Transverse distributed load.
R_x, R_y	Radii of curvature of the DCS in the x- and y-directions, respectively.
t	Time.
δT	The variation of the kinetic energy.

u_0, v_0, w_0	The displacements of the mid-surface in the *x*-, *y*-, and *z*-directions, respectively.
$\dot{u}$, $\dot{v}$, $\dot{w}$	The velocities in the *x*-, *y*-, and *z*-directions, respectively.
δU	The variation of the strain energy.
V	Volume of the structure.
V_c, V_m	Volume fractions of the ceramic and metal, respectively.
w	Transverse displacement.
δW	The variation of the work performed by the external forces.
$\{\varepsilon^0\}$, $\{\varepsilon^1\}$, $\{\gamma^0\}$	Membrane, Bending, and Shear strain vectors, respectively.
ε_z	Transverse normal strain.
ν	Poisson's ratio.
ν_c, ν_m	Poisson's ratio of the ceramic and metal, respectively.
ρ	Mass density.
ρ_c, ρ_m	The mass density of the ceramic and metal, respectively.
σ, τ	Normal and shear stress.
σ_z	Transverse normal stress.
ϕ_x, ϕ_y	The rotations of the normal to the mid-surface about the *x*- and *y*-axes, respectively.
$\dot{\phi}_x$, $\dot{\phi}_y$	The rotational velocities about the *x*- and *y*-axes, respectively.
χ	Mode shape vector.
ω	Natural frequency.

Λ Component of the material stiffness matrix.

Π The total potential energy.

List of Abbreviations

2D	Two-dimensional
3D	Three-Dimensional
BCs	Boundary conditions
CNTR	Carbon nanotubes reinforced
CPT	Classical plate theory
CST	Classical shell theory
CUF	Carrera's unified formulation
CY	Cylindrical
DCS	Doubly curved shell
DCSS	Doubly curved shallow shell
DFF	Dimensionless fundamental frequency
DOF	Degrees of freedom
DTD	Dimensionless transverse displacement
ELP	Elliptical paraboloid
ES-FEM	Edge-based smoothed finite element method
ESL	Equivalent single-layer theory
FEM	Finite element method
FL	Flat

FG-CNTRC	Functionally graded carbon nanotube-reinforced composite
FGM	Functionally graded material
FSDT	First-order shear deformation theory
HYP	Hyperbolic paraboloid
GDQ	Generalized differential quadrature method
FG-GRC	Functionally graded graphene-reinforced composite
HSDT	Higher-order shear deformation theory
NS-FEM	Node-based smoothed finite element method
RPT	Refined plate theory
RHSDT	Refined Higher-order shear deformation theory
ROM	Rule of mixture
SCSDT	Second-order shear deformation theory
SCF	Shear correction factor
SL	Sinusoidally distributed load
SP	Spherical
STA	The Science and Technology Agency
TSDT	Third-order shear deformation theory
UL	Uniformly distributed load

General introduction

General introduction

Materials science is a cornerstone of innovation and research across diverse engineering domains. The exploration of new materials has historically been driven by two key motivations. It addresses practical challenges affecting human life while fulfilling our deep-seated curiosity about the natural world. This pursuit has led to the development of specialized materials like composites, which combine the best parts of different substances to solve specific problems. By using these advanced materials, we are fixing today's challenges and opening the door to new inventions that will greatly affect our lives in the future.

Composite materials, engineered by combining two or more distinct materials, are designed to achieve properties that individual components cannot offer alone. Typically, they consist of a matrix, such as a polymer, metal, or ceramic, which binds the reinforcement phase, usually fibers or particles, to enhance strength, stiffness, and durability. However, traditional composites encounter several challenges, primarily due to the abrupt changes in properties and stresses at the interfaces separating various layers. This abrupt transition in material composition leads to high-stress concentrations, resulting in localized weaknesses. The stress concentrations often cause matrix cracking and significantly increase the risk of delamination, especially in high-temperature environments where the mismatch in thermal expansion between layers intensifies the problem.

To overcome these limitations, a significant advancement in materials science has been achieved with the development of a new composite material known as functionally graded materials (FGMs). Unlike traditional composites, which have distinct and abrupt interfaces between layers, FGMs exhibit a smooth, continuous variation in composition and structure. This gradual transition in material properties, typically accomplished by adjusting volume fractions, enables FGMs to combine the advantages of different materials effectively. A typical FGM may shift from metal, which provides mechanical strength, to ceramic, which offers heat resistance, thus improving performance under extreme thermal or mechanical loads. Initially developed for the aerospace and nuclear sectors, FGMs are now widely used across various industries, including biomedical engineering, civil engineering, automotive design, electronics, and energy-efficient structures. Their ability to minimize stress concentrations, improve thermal stress resistance, and enhance overall durability makes them ideal for demanding applications where conventional materials fall short.

In recent years, the finite element method (FEM) has emerged as a powerful and versatile tool for analyzing structures made of advanced materials. Its ability to handle complex geometries, irregular boundary conditions, and geometric non-linearity makes it the preferred approach for analyzing functionally graded doubly curved shallow shells (FG DCSS). By offering detailed insights into stress distribution, deformation, and vibrational response, FEM has greatly enhanced the design, manufacturing, and application of FGMs across various engineering fields.

Structural elements made of FGMs can be effectively analyzed using either 3D or 2D theoretical approaches. While the 3D approach provides higher accuracy, its complexity and computational cost make it a less suitable choice compared to the 2D approach. The 2D approach, often employed in the analysis of FGMs, includes various theories such as classical plate theory (CPT), first-order shear deformation theory (FSDT), and higher-order shear deformation theory (HSDT), each offering distinct advantages. CPT is the simplest method and is generally used for thin structures where shear deformation is negligible. FSDT, on the other hand, accounts for a constant transverse shear deformation, making it more suitable for thicker structures, but it requires a shear correction factor (SCF). HSDTs offer greater precision by incorporating higher-order terms, eliminating the need for SCF, and providing a more accurate representation of shear stresses across the structure's thickness.

Thesis objectives

A review of the literature reveals a significant gap in studies on FG doubly curved shells, particularly spherical, hyperbolic paraboloid, and elliptical paraboloid shells. The dominant approach remains analytical, with limited use of the FEM. This highlights the need for further research utilizing numerical methods, especially the FEM, to provide more comprehensive and versatile analysis of these complex shell structures.

The aim of this thesis is to present a detailed analysis of the bending and free vibration behavior of FG doubly curved shallow shells (FG DCSSs) using the FEM. To achieve this, a new 2D C^0 eight-node isoparametric quadrilateral element with five degrees of freedom per node is developed based on an improved first-order shear deformation theory (IFSDT). This formulation strikes an optimal balance between accuracy and computational efficiency, offering a valuable tool for researchers and engineers seeking precise yet cost-effective solutions in the field.

Thesis organization

The thesis is organized into four chapters, as outlined below:

Chapter provides a comprehensive overview of FGMs, covering their fundamental concepts, types of material gradients, and historical development. It explores various fabrication methods and highlights the diverse applications of FGMs across multiple fields. The chapter also examines homogenization techniques and gradation laws used to model the variation of material properties. Additionally, key theoretical frameworks, including CPT and FSDT, are discussed, along with the importance of SCF. HSDT is also explored in detail. The chapter concludes with an extensive literature review, focusing on the application of these theories in analyzing the static and vibrational behaviors of FG plates and shells.

Chapter Two present the theoretical formulation for analyzing the mechanical behavior of FG DCSs. Five distinct types of FG curved shells have been analyzed, including Flat plate, cylindrical shells, spherical shells, hyperbolic paraboloid shells, and elliptical paraboloid shells. The material properties are vary continuously through the thickness, following a power-law distribution. The kinematic description incorporates an enhanced displacement field that accounts for curvature effects. Constitutive relations, strain-displacement equations, and stress resultants are established. The presented theoretical framework extends beyond the traditional by integrating a parabolic shear stress distribution function g(z), satisfying the traction conditions on the top and bottom surfaces of the shell. The governing equations of motion are derived using the Hamilton principle, resulting in formulations that encompass stiffness, load, and mass matrices for both static and free vibration analyses of FG DCSSs. The chapter introduce a novel 2D C^0-continuous isoparametric eight-node isoparametric quadrilateral element (SQ8-IFSDT), incorporating five degrees of freedom per node based on IFSDT. The chapter also outlines the FE procedure in detail, including the assembly of global matrices, the solution of equilibrium equations for static analysis, and the implementation of a generalized eigenvalue problem of the free vibration analysis.

Chapter Three evaluates the accuracy and efficiency of the developed FE model, QS8-IFSDT, in predicting the bending response of functionally graded doubly curved shells (FG DCSSs). The chapter presents detailed results for transverse displacement, normal stress, and shear stress, while examining the influence of key parameters—including the power-law index (k), side-to-thickness ratio (a/h), radius-to-thickness ratio (R/h), radius-to-length ratio (R/a), boundary conditions, and loading types. A convergence study is conducted to assess the model's numerical efficiency, followed by comprehensive validation against existing studies. Additionally, the chapter introduces new numerical findings not previously reported in the literature.

Chapter Four evaluates the efficiency and accuracy of the proposed finite element model, QS8-IFSDT, in analyzing the free vibration behavior of FG DCSSs. A comprehensive parametric study is conducted to investigate the effects of key parameters, including the power-law index (k), side-to-thickness ratio (a/h), radius-to-length ratio (R/a), and boundary conditions. To ensure numerical stability and reliability, a convergence analysis is first performed. The resulting natural frequencies are validated through comparison with established solutions from the literature. Moreover, the chapter introduces new numerical findings not previously reported, contributing original insights to the field. Mode shapes are also illustrated to deepen the understanding of the dynamic response of FG DCSSs.

Finally, a general conclusion is presented, summarizing the challenges addressed and emphasizing the key findings related to the static and free vibration behavior of FG DCSSs. Additionally, potential avenues for future research are outlined, building on the insights gained from this study.

Chapter 01

Functionally Graded Materials: An overview

Chapter 01

Functionally Graded Materials: An overview

1.1 Introduction

The demand for materials with exceptional technical performance and superior mechanical properties is rapidly increasing across various industries, including aerospace and civil engineering. These materials are essential for constructing structures that are not only strong and durable but also capable of withstanding harsh conditions over long periods. To meet these demands, advanced materials such as laminate composites have been developed. Composites laminate combine distinct materials to achieve enhanced properties, including high strength-to-weight ratios, excellent fatigue resistance, and improved thermal and electrical performance. As a result, they have gained widespread use in a variety of applications, ranging from aircraft and automotive components to sporting equipment and infrastructure projects.

Composite laminate materials involve joining two different materials, where the interface between them represents a sudden transition from one material to another. Their anisotropic nature can lead to stress concentrations and geometric discontinuities, which result in damage mechanisms such as delamination, matrix cracking, and interfacial separation. These issues ultimately degrade the mechanical properties of the structure. Additionally, composite laminates often struggle in high-temperature environments, limiting their applicability in extreme conditions.

To address these challenges, researchers have turned to functionally graded materials (FGMs), an advanced class of composites characterized by a gradient in composition throughout their volume [1]. This gradual variation optimizes mechanical and thermal performance, enabling FGMs to better withstand high temperatures and enhance mechanical properties compared to traditional composites [2]. Often regarded as “smart” materials, FGMs are designed with embedded functions that allow their composition to be tailored to meet specific application requirements and environmental conditions.

The advantages of FGMs are numerous, including improved stiffness, fatigue resistance, corrosion resistance, and thermal conductivity [3]. Their graded properties facilitate precise control over performance metrics, such as minimizing localized stresses and enhancing heat transfer efficiency, making FGMs highly suitable for a wide range of applications [4]. The groundbreaking concept of FGMs has sparked a revolution in materials science and mechanics. Originally conceived and developed in Japan, FGMs have garnered increasing global interest, as evidenced by the growing number of high-quality conferences and publications dedicated to their analysis, design, and fabrication.

Today, the application of FGMs has expanded significantly, providing innovative solutions to a wide array of engineering challenges. Their ability to seamlessly integrate varying material properties within a single structure makes them invaluable across industries such as aerospace, automotive, biomedical, civil engineering, and energy. The growing adoption of FGMs in these sectors underscores their potential to enhance performance, durability, and efficiency in complex systems. As research continues to evolve, the versatility and adaptability of FGMs are driving further innovations, opening new opportunities for their integration into advanced technologies and industrial applications.

1.2 The concept of FGMs

FGMs, also known as "gradient materials," represent a novel approach to material design and manufacturing. This approach involves the continuous variation of material constituents' volume fractions across different spatial positions based on a predefined gradient or law. This gradual transition in composition results in a spatial distribution of material properties such as physical, mechanical characteristics specifically tailored to meet the unique demands of a given application [5].

FGMs were first proposed in 1984 by Japanese scientists as a solution for producing thermal barrier coatings for a space plane project [6, 7]. This composite material offered the advantage of reducing thermal stresses, which were problematic in traditional laminate composites [8].

FGMs are characterized by their distinct compositional gradient, where one material transitions smoothly and continuously into another. This sets them apart from traditional composite materials, which are typically homogeneous mixtures that require a compromise in material properties, or laminate composite materials that involve joining two or more different materials together [8], as shown in **Figures 1.1** and **1.2**.

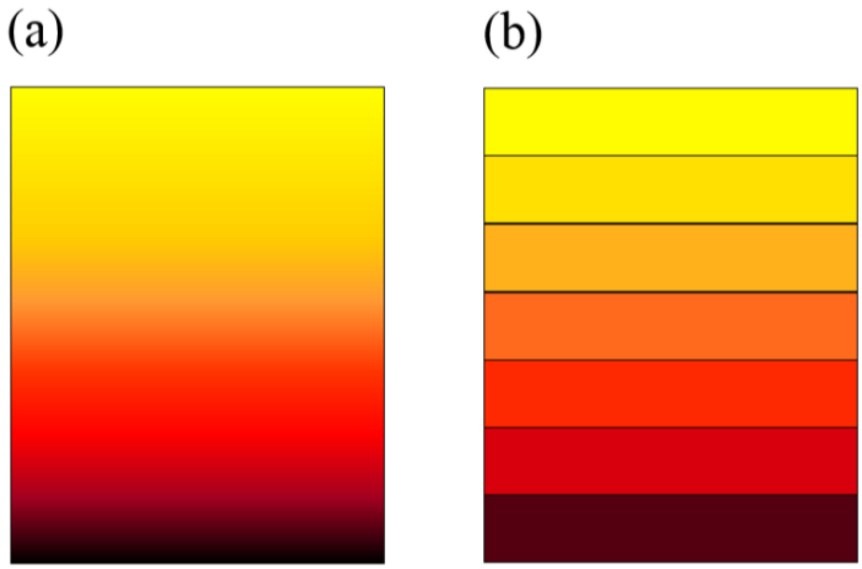

Figure 1.1 Schematic representation of (a) FGM and (b) Composite laminate.

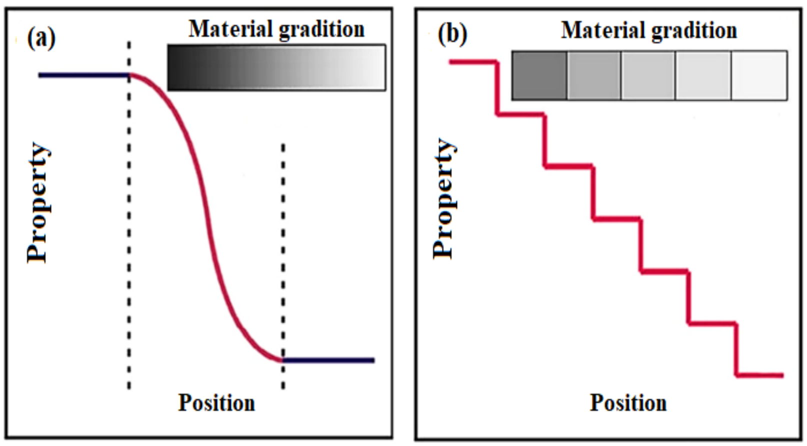

Figure 1.2 (a) continuous and (b) discrete types of FGM. [9]

FGMs typically consist of a combination of ceramics and metal. The inclusion of a brittle ceramic component with low thermal conductivity provides resistance to high temperatures, while the metal component prevents crack initiation at stress concentration sites, especially when subjected to a rapid increase in temperature gradient. **Table 1.1** Outlines the benefits associated with ceramic and metal components.

Table 1.1 The advantages of ceramic and metal components.

High-temperature face	Ceramic	▪ Excellent thermal resistance ▪ High oxidation resistance ▪ Low thermal conductivity
Middle layers	Ceramic-metal	▪ Mitigates interface issues ▪ Relieves thermal stresses
Low-temperature face	Metal	▪ High thermal conductivity ▪ Excellent toughness

FGMs have an advantage due to the absence of clear internal boundaries, as illustrated in **Figure 1.3**. This reduces the risk of failures often associated with interface stress concentrations, which is a common problem in traditional components.

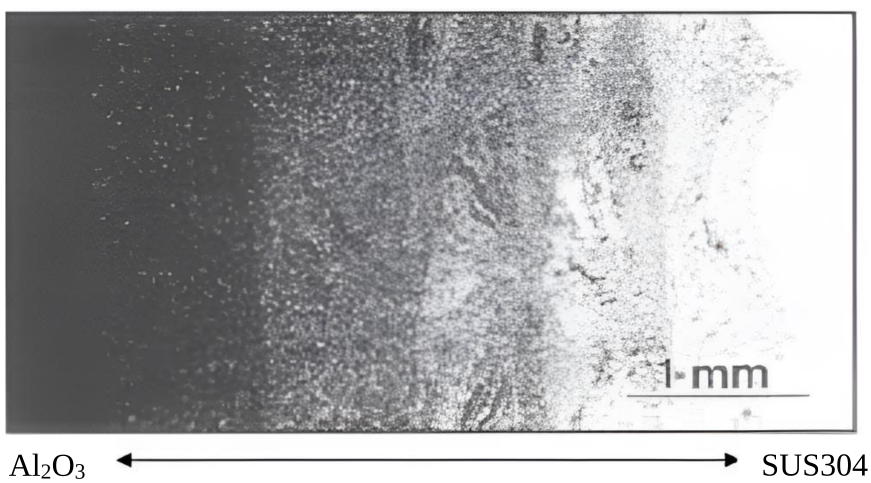

Figure 1.3 A scanning electron microscope image capturing the cross-sectional view of an FG (Al_2O_3/SUS_{304}). [10]

FGMs exhibit gradual transitions in both microstructure and composition, enabling them to address specific functional requirements based on the position within a structural component. This design approach aims to optimize the overall performance of the component by adapting to its varying needs.

1.3 The history of research and development

The idea of FGMs may seem like a modern engineering innovation, but its roots can be traced back to the design principles of nature. Natural materials like bones, tooth enamel, skin, and bamboo [8, 11] exhibit graded characteristics that have inspired the development of FGMs, as presented in **Figure 1.4**. For example, bones demonstrate a gradient in stiffness from the outer cortical bone to the inner trabecular bone, providing both strength and resilience [12]. Tooth enamel shows a gradient in hardness, with the outer layer being harder to withstand chewing forces, while the inner layer is softer to absorb shock and prevent cracking [13]. Human skin exhibits varying toughness, tactile properties, and elasticity across its layers, offering protection and flexibility [14]. Bamboo's structure exhibits a natural gradient in stiffness and strength along its length, with denser and more rigid outer layers providing structural support and more flexible inner layers allowing the bamboo to bend without breaking [15]. These natural examples highlight the effectiveness of gradient structures in optimizing material properties for specific functions, inspiring the development of engineered FGMs for various technological applications.

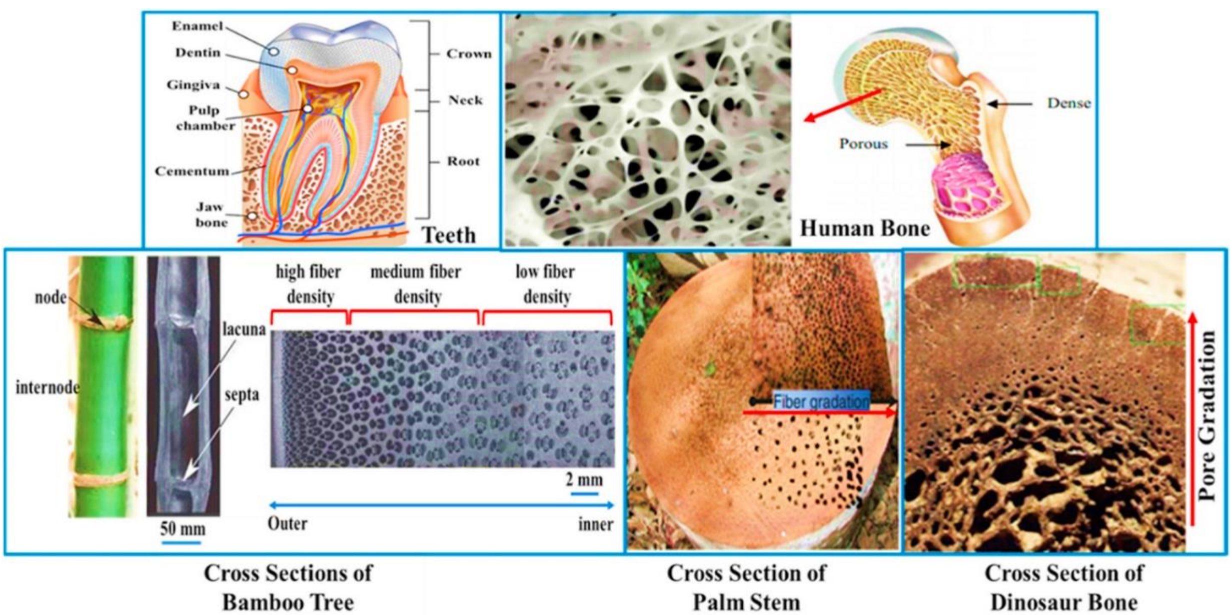

Figure 1.4 Examples of FGM in nature. [16]

The original idea of incorporating compositional and structural gradients into material microstructures was proposed in 1972 for composites and polymeric materials. This concept aimed to mimic the structure and behavior of natural materials such as bones, teeth [17], and bamboo trees [18]. Bever and Duwez [19] examined various composites with spatially graded material properties. Subsequently, Shen and Bever [20] analyzed graded polymers. They proposed different models for gradients in composition, filament concentration, and polymerization, along with potential applications for the resulting graded structures. However, it was not until the 1980s that actual investigation into the design, fabrication, and evaluation of graded structures occurred.

In 1984, FGMs were explored in Japan during a space plane project [21], where a combination of materials was fabricated to create a thermal barrier capable of withstanding surface temperatures ranging from 1700 °C to 700 °C through a 10 mm thickness, as illustrated in **Figure 1.5**. At that time, no single material could uniformly resist such conditions. Consequently, the researchers proposed a method to fabricate a material by gradually changing its composition, enhancing both thermal resistance and mechanical behavior.

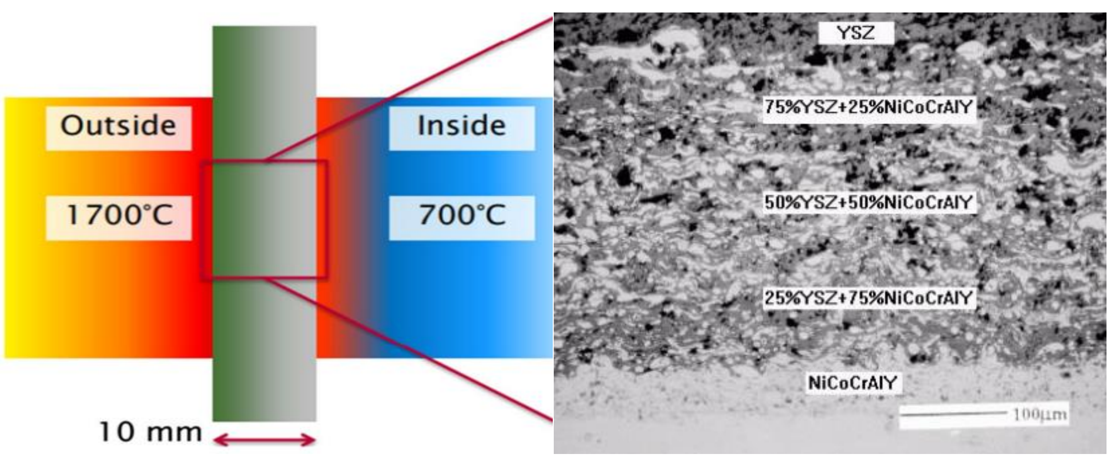

Figure 1.5 Plasma sprayed of FG (ZrO_2/NiCoCrAlY) used in the thermal barrier coating. [22]

In 1986, this advanced material was referred to as “functionally gradient material,” later abbreviated as “FGM.” However, following discussions at the third International Symposium on FGMs in Lausanne in 1994, it was decided in 1995 to change the term to “functionally graded material” for improved descriptive clarity and grammatical accuracy.

The first national project, known as “Research On The Basic Technology For Relaxation Of Thermal Stress” or “FGM Part I” began in 1987 as a five-year research program with dedicated coordination funds from the Science and Technology Agency (STA) [23]. Its goal was to develop advanced heat-shielding materials, including a thermal barrier coating for potential space program applications. This project concluded in 1992, making significant progress in the design, production, and analysis of FGMs to reduce thermal stress. In 1992, FGMs were recognized as one of the 10 most advanced technologies in Japan.

Throughout the 1990s, the scope of applications for FGMs expanded beyond high-temperature structural materials to include fields like sensor technology, biomechanics, optics, and more.

Another national project, named “Development of Energy Conversion Materials Through Formation of Gradient Structures” aimed to apply the FGM concept to enhance the efficiency of energy conversion materials. This project was initiated in 1993 with support from STA and concluded in March 1998. Notable outcomes of this project include advancements in thermoelectric and thermionic conversion efficiency through the incorporation of gradient structures in material and element design [24].

In 2001, a global workshop chaired by Prof. Naotake Ooyama highlighted recent trends and prospects in the field. It covered topics such as modeling, automated manufacturing systems, residual stress measurement, ultrasonic imaging, and the biocompatibility of FG implant materials. This event marked the beginning of regular research programs, international symposiums, and workshops worldwide [25].

Since 2006, a transregional collaborative research center has been funded in Germany to explore the capacity of grading monomaterials like steel, aluminum, and polypropylene. This exploration involves using thermo-mechanically coupled manufacturing processes [26].

The 17th “International Symposium on Functionally Graded Materials” was held in Braga, Portugal, at the International Iberian Nanotechnology Laboratory from September 29 to October 2, 2024.

Figure 1.6 depicts a timeline showing the historical development of FGM. The timeline effectively charts key milestones in the conceptualization, development, and international recognition of FGMs, beginning with early research in the 1970s and continuing through to present-day advancements and global conferences.

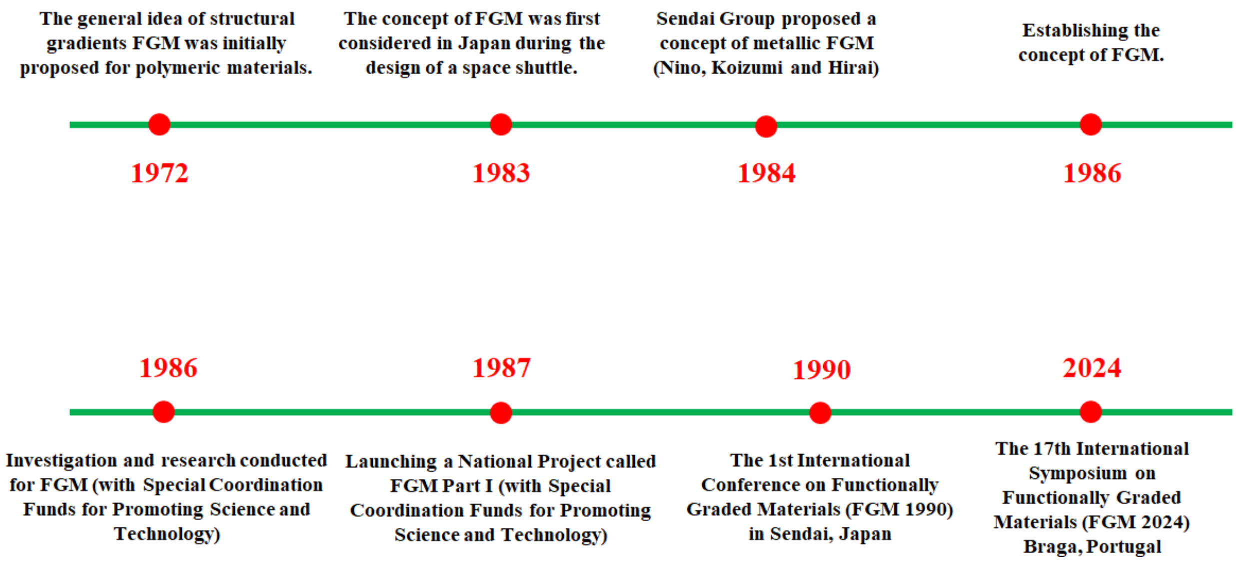

Figure 1.6 The historical evolution of FGMs.

1.4 Gradient types

FGMs were developed to address the limitations of traditional composites, which often had abrupt interfaces between different materials. FGMs introduce a gradual variation in properties, such as chemical composition, porosity, or microstructure, across the material's volume, as depicted in **Figure 1.7**. This design approach aims to optimize material performance by reducing stress concentrations at interfaces and improving overall structural integrity. The gradual transition in properties in FGMs helps to improve their compatibility, leading to enhanced mechanical, thermal, and chemical properties compared to traditional composites.

1.4.1 Chemical composition gradient

FGMs exhibit a gradual variation in their chemical composition, typically transitioning from one material to another within the bulk volume. There are two main types: single-phase and multiphase FGMs.

1.4.1.1 Single-phase

Single-phase FGMs are formed from one phase, allowing the chemical elements of one phase to gradually dissolve into the other phase during the manufacturing process, typically through sintering [27]. This gradual change in chemical composition within the single phase results in the development of a material with unique and tailored properties along its gradient.

1.4.1.2 Multiphase

Multiphase FGMs are more commonly used, offering great flexibility in material design. These materials are designed to vary in phases and chemical compositions throughout their volume [28, 29]. By carefully controlling the composition gradient from one material to another, different phases with distinct chemical compositions are created within the material, each tailored to perform specific functions. The resulting phases depend on various factors, such as the initial composition of the materials, the amount and type of reinforcing material used, and the specific manufacturing conditions (cooling rate, heat treatment process).

1.4.2 Porosity gradient

The variation in porosity within FGMs is achieved through the manipulation of pore sizes or shapes or a combination of both factors. This can be accomplished by adjusting the sizes of powder particles used in different parts of the material during the fabrication process. Alternatively, it can be achieved by modifying production and sintering parameters to create the desired porosity gradient [30, 31].

The application of pore size gradation is notable in bone implants, where larger pores within FG implants are designed to be implanted in the bone to promote bone ingrowth, while smaller pores are beneficial for cartilage growth [30]. Porosity-graded FGMs serve several functions, including facilitating shock absorption across the material, providing thermal insulation, reducing electrical and thermal stresses, and enhancing catalytic efficiency.

1.4.3 Microstructure gradient

Microstructural gradient FGMs are distinguished by a gradual variation in microstructure across the volume of material. This variation is often achieved through processes such as solidification or controlled heat treatment. These materials find extensive use in applications requiring a blend of surface hardness for wear resistance and inner toughness for high-impact durability. Notable applications include bearings, case-hardened steel, camshafts, and turbine components [32, 33].

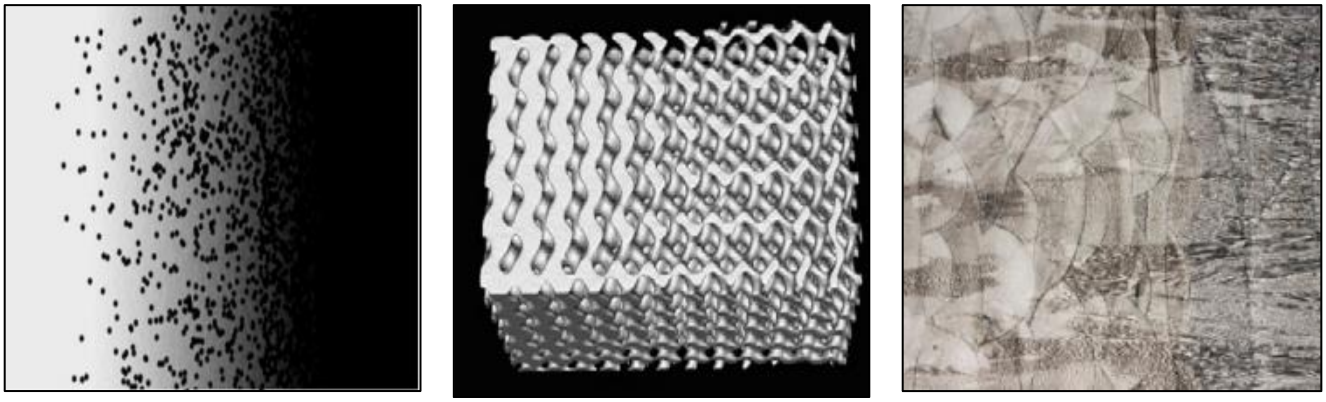

Composition [34] Porosity [35] Microstructure [36]

Figure 1.7 Gradient types of FGMs.

Each of these three types offers distinct advantages and is tailored to meet specific application requirements. The selection of a particular FGM type depends on the targeted properties and performance characteristics required for the intended application.

1.5 Fabrication techniques

The idea of using composites with property gradients was first introduced in 1972 [19, 20]. However, their impact was limited due to the lack of suitable production methods at that time. It took another 15 years for systematic research on manufacturing processes for property-graded materials to be conducted as part of a national research program on FGMs in Japan. Since then, a significant portion of research has focused on processing these materials, leading to the development of a wide range of production methods [24, 37]. The choice of production method is primarily influenced by factors such as the combination of materials, the type of transition function required, and the geometry of the desired component [38].

FGMs can be found in two primary forms: as thin coatings applied to a material's surface to improve surface characteristics, or as bulk materials where properties change throughout the entire volume.

1.5.1 Thin FGMs

These materials are commonly used as surface coatings. The selection of the deposition technique is influenced by the particular service requirements of the process [28]. They are typically produced using various methods such as plasma spraying, vapor deposition, and self-propagating high-temperature synthesis. However, for coating applications, the most significant methods are deposition-based, including vapor deposition, thermal spray, and electrophoretic deposition [39].

Vapor deposition is particularly crucial for producing thin graded layers, where materials are transformed into solid material during the vapor cycle [40]. This method encompasses techniques like chemical vapor deposition, physical vapor deposition, and sputter deposition, all of which are employed to deposit FG surface coatings [41], as shown in **Figure 1.8**.

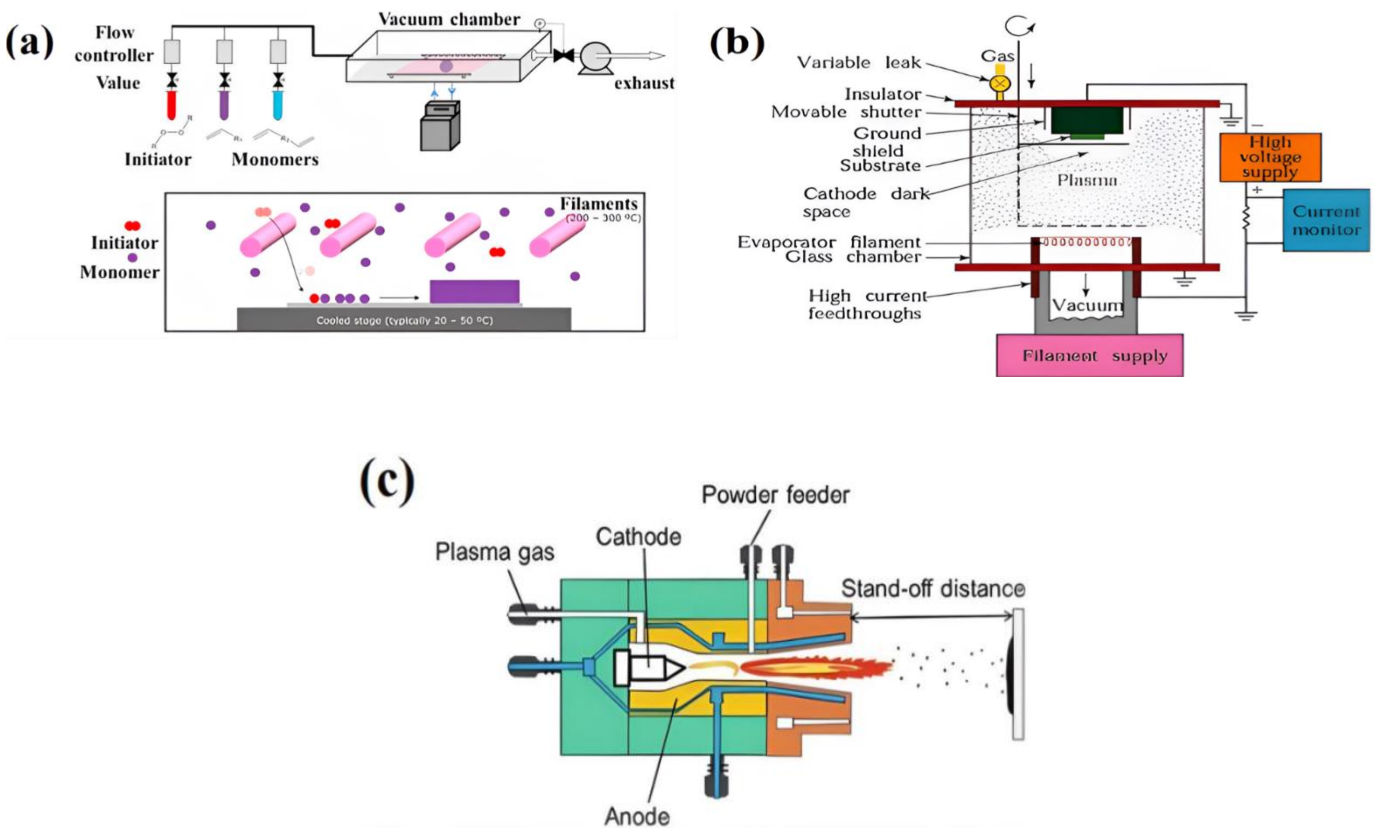

Figure 1.8 (a) Chemical vapor deposition [42] (b) Physical vapor deposition [43] (c) Plasma spraying [44]

Despite their ability to produce excellent coatings microstructures, these techniques are energy-intensive and create toxic gases [45].

1.5.2 Bulk FGMs

The mentioned methods above are unsuitable for bulk FGM production due to their slow and energy-intensive nature, making them economically impractical. Several alternative fabrication methods have been proposed for bulk functionally graded materials, including:

1.5.2.1 Powder metallurgy method

The powder metallurgy is a long-established technique for component production and has recently gained popularity for producing FGMs due to its versatile characteristics [46]. It has become one of the most widely used methods in the field [47], particularly for producing bulk FGMs with discontinuous gradient characteristics [48]. The process involves four essential steps: mixing, stacking, compaction, and sintering, as presented in **Figure 1.9**.

The process begins with mixing powders and carefully selecting materials to achieve the required graded properties. The weight of each powder and the thoroughness of mixing are important to ensure that each component in the mixture is uniformly dispersed. This dispersion greatly influences the characteristics of the product [49].

In the next step, the mixed powder is stacked layer by layer in the mold according to the desired spatial distribution of materials. The composition of each layer is carefully controlled to achieve the desired properties at each step.

Following stacking, the powder is compacted to give the structure strength and integrity. This step is essential for ensuring that the layers adhere properly and form a solid structure [50].

In the final step, the compressed structure is sintered by heating it to a temperature below the melting point of the main component. This process causes the particles to bond together, forming a solid material [51].

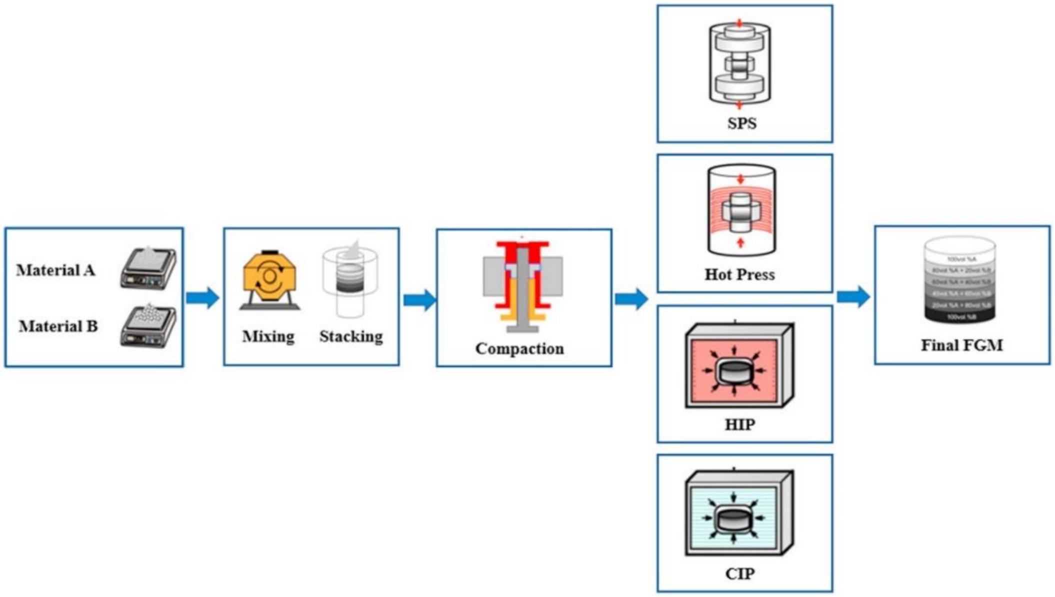

Figure 1.9 The sequential stages of the powder metallurgy process used in the fabrication of FGMs. [51]

1.5.2.2 Centrifugal method

In this method, the molten metal is poured into a rotating mold. The combination of gravity and rotation shapes the material into a bulk FG form [52]. The graded structure is achieved because of the varying material densities and the mold's rotation [53], as shown in **Figure 1.10**.

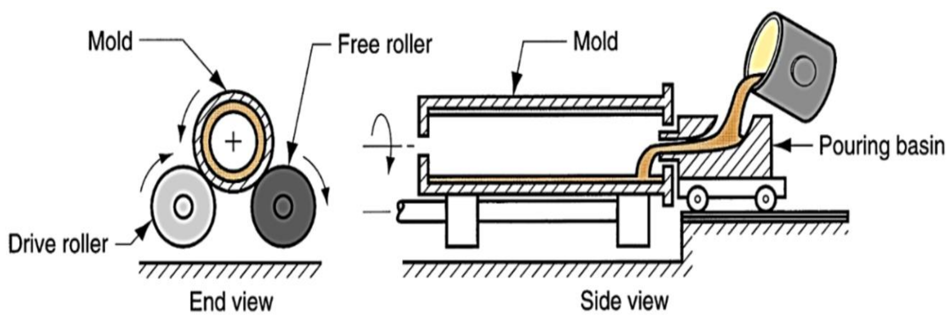

Figure 1.10 Centrifugal casting. [54]

While the centrifugal method is effective for achieving continuous grading, it is restricted to forming CY shapes. Another limitation is the type of gradient that can be produced, which is determined by the natural processes involved, such as centrifugal force and density differences [11]. To overcome these challenges, researchers are exploring a different manufacturing approach known as solid freeform [55].

1.5.2.3 Solid freedom method

Solid freeform is an additive manufacturing technique that provides numerous benefits, such as increased production speed, reduced energy consumption, optimal material usage, and the capability to produce complex shapes. Furthermore, it provides design flexibility as parts can be produced directly from CAD data (e.g., AutoCAD) [56], as shown in **Figure 1.11**. The process consists of five steps as follows [57]:

1. Generation of CAD data using software such as AutoCAD or Solid Edge.
2. Conversion of the CAD data to a standard triangulation language file.
3. Slicing the standard triangulation language file into 2D cross-section profiles.
4. Building the component layer by layer.
5. Removal of excess material and finishing.

The solid freeform method encompasses a range of advanced technologies, particularly laser-based processes, widely utilized in the production of FGMs [58]. These include laser cladding methods [59], selective laser sintering [60], 3D printing [61], and selective laser melting [62].

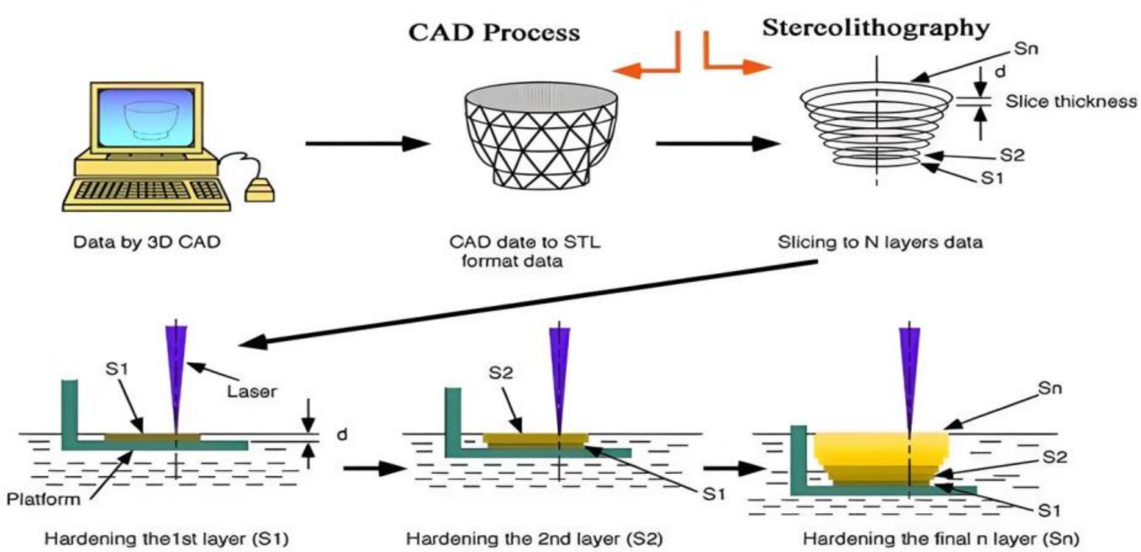

Figure 1.11 Solid freedom fabrication steps. [9]

While solid freeform fabrication offers manufacturing flexibility compared to other processes, it often results in poor surface finish, requiring secondary finishing processes. There are also alternative fabrication methods that provide detailed discussions of processing techniques for FGM [53, 63].

1.6 Applications

FGMs are used in various industries, with applications expanding across aerospace, automobile, civil engineering, medicine, defense, energy, optoelectronics, and more [64], as demonstrated in **Figure 1.12**.

1.6.1 Aerospace

FGMs are extensively used in the aerospace industry due to their ability to withstand extremely high thermal gradients. Various parts of spacecraft and aircraft now utilize FGMs, including rocket engines, spacecraft gear structures, heat exchange plates, and structural components including reflectors, solar panels, camera bunks, turbine wheels, turbine blade coatings, and space shuttles [65].

1.6.2 Automobile

The employment of FGMs in the automobile industry is very limited due to their high production cost. However, they are used in critical parts where the high cost is justified. These include engine cylinder liners for diesel engine pistons, leaf springs, spark plugs, combustion chambers, drive shafts, flywheels, window glass, and racing car brakes [26]. Additionally, FGMs are used in advanced body coatings for cars, featuring graded coatings with particles like dioxide/mica [11].

1.6.3 Medicine

Living tissues, like bones and teeth, are naturally characterized as FGMs [66]. To replace these tissues, a suitable material that can effectively mimic the original biological structure is required. FGMs have found widespread use in dental and orthopedic fields for the replacement of teeth and bones [67, 68].

1.6.4 Defense

One of the key characteristics of FGM is its ability to impede crack propagation. This quality renders them valuable in defense applications, where they are utilized as materials resistant to penetration, such as in armor plates and bulletproof vests [32]. The composition of the material transitions from titanium diboride to a mixture of titanium and titanium diboride combining the energy-absorbing properties of ceramics with the toughness of metals, making it well-suited for use in vehicle armor solutions [69].

1.6.5 Energy

FGMs are widely utilized in energy conversion devices for their ability to function as effective thermal barriers, enhancing energy efficiency by reducing thermal stresses. Additionally, they are applied as protective coatings on turbine blades in gas turbine engines, where they help withstand extreme temperatures and improve durability. This protective layer extends the lifespan of turbine components by minimizing thermal fatigue and oxidation [70, 71].

1.6.6 Optoelectronics

FGMs are used in optoelectronics as materials with graded refractive indices. They are also utilized in audio-video discs, magnetic storage media, highly efficient photodetectors, solar cells, and tunable photodetectors [72].

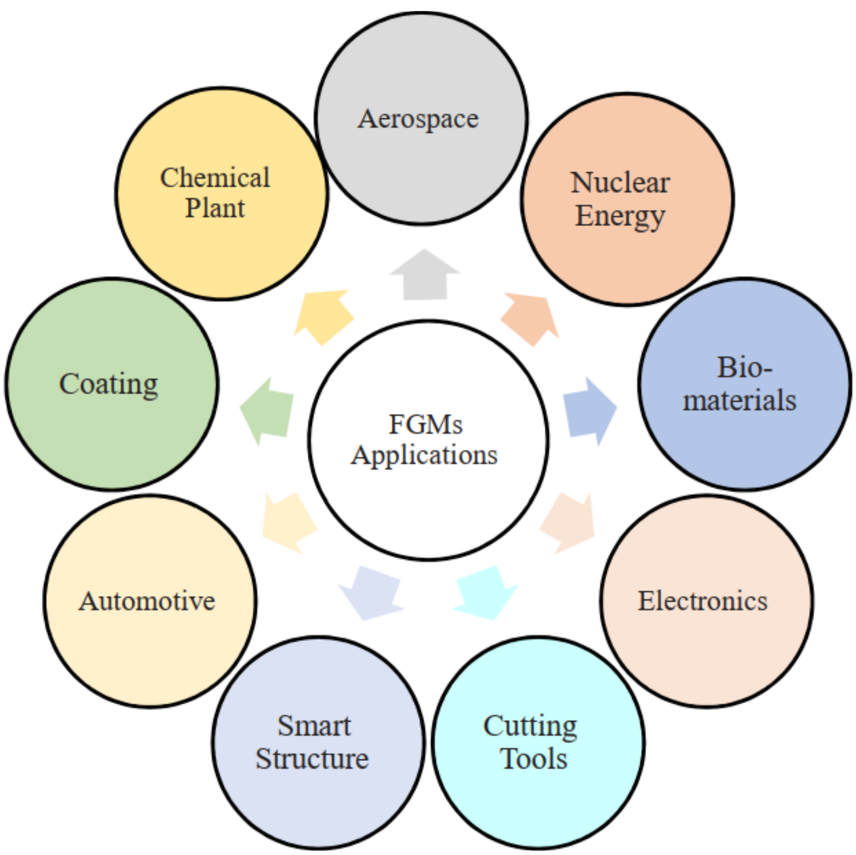

Figure 1.12 Practical applications of FGM. [16]

1.7 Homogenization techniques

Various methods are used to determine the effective properties at specific locations within composite materials. These include the rule of mixtures, the Mori-Tanaka approach, and the self-consistent method, among others. Nowadays, these techniques are frequently applied to estimate the effective properties of FGMs, allowing for precise characterization of their graded structure. [73].

1.7.1 The rule of mixture (ROM)

The mechanical material properties of an FGM can be determined by the rule of mixture, also known as the Voigt model [74]. According to this rule, the effective properties of an FGM are calculated as a weighted average of the properties of its constituent materials based on their volume fractions. This relationship is expressed as:

$$P(z) = P_m V_m + P_c V_c \tag{1.1}$$

P represents the effective material property, such as Young's modulus E, Poisson's ratio v, and Mass density ρ. P_m, P_c, V_m, and V_c denote material properties and the volume fraction of the upper (metal) and the lower (ceramic) faces of the structure, respectively. The sum of the volume fractions of the constituent materials should equal one.

$$V_m + V_c = 1 \tag{1.2}$$

1.7.2 Mori-Tanaka scheme

This scheme was introduced in 1973 [75] to calculate materials' average stress and elastic energy. About fifteen years later, a modified version was used in advanced composite materials [76]. It is well suited for analyzing a graded composite microstructure with a clearly defined, continuous, isotropic matrix phase reinforced by a random distribution of isotropic particles from a particulate phase. The microstructure is illustrated in **Figure 1.13**.

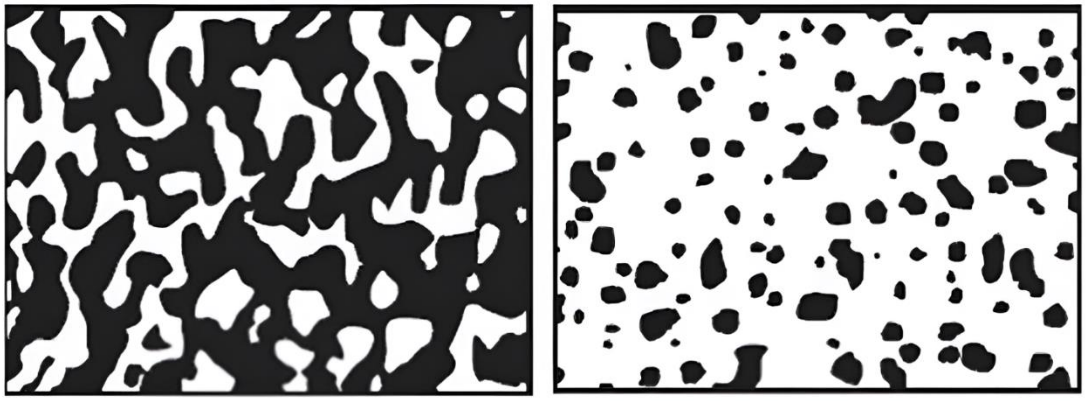

Figure 1.13 Two-phase material with (a) skeletal microstructure and (b) particulate microstructure. [77]

For the Mori–Tanaka scheme [78], the effective material properties of an FGM are defined in the equation below:

$$P(z) = P_m + (P_c - P_m)\frac{V_2}{1 + V_m(\frac{P_c}{P_m} - 1)\frac{1+\nu}{3-3\nu}} \tag{1.3}$$

Given that the effects of Poisson's ratio (ν) on the response of FG structure are minimal, they are assumed to remain constant for all functionally graded layers.

1.8 Gradation laws

The variation of material properties in FGMs is typically described using power-law, exponential-law, or sigmoid-law distributions. These formulations allow for a smooth transition of material composition along the thickness direction, from a metal-rich bottom face to a ceramic-rich top face, as shown in **Figure 1.14**, ensuring optimal mechanical and thermal performance tailored to design requirements.

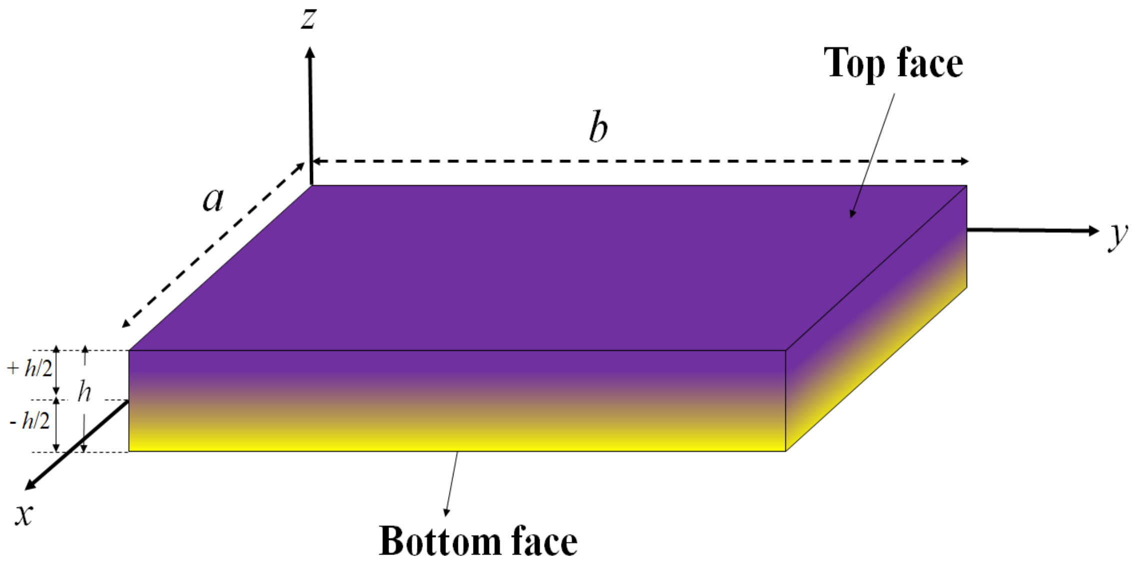

Figure 1.14 FGM plate geometry.

1.8.1 Power-law function (P-FGM)

The power-law model is widely employed as a prominent approach for describing the variation of material properties in a specific direction, and it is more common in the stress analysis of FGM [79].

The variation in material properties of FG plate along thickness direction according to the power-law distribution is given by:

$$P(z) = P_m + (P_c - P_m)V(z) \tag{1.4}$$

The volume fraction is described as:

$$V(z) = \left(\frac{1}{2} + \frac{z}{h}\right)^k \tag{1.5}$$

Where $0 \leq k \leq +\infty$ is the power-law index.

Figure 1.15 depicts the variation of volume fraction along the thickness of the plate. It is evident from the figure that when $k < 1$, the volume fraction decreases significantly near the lower surface, whereas for $k > 1$, it increases markedly near the upper surface.

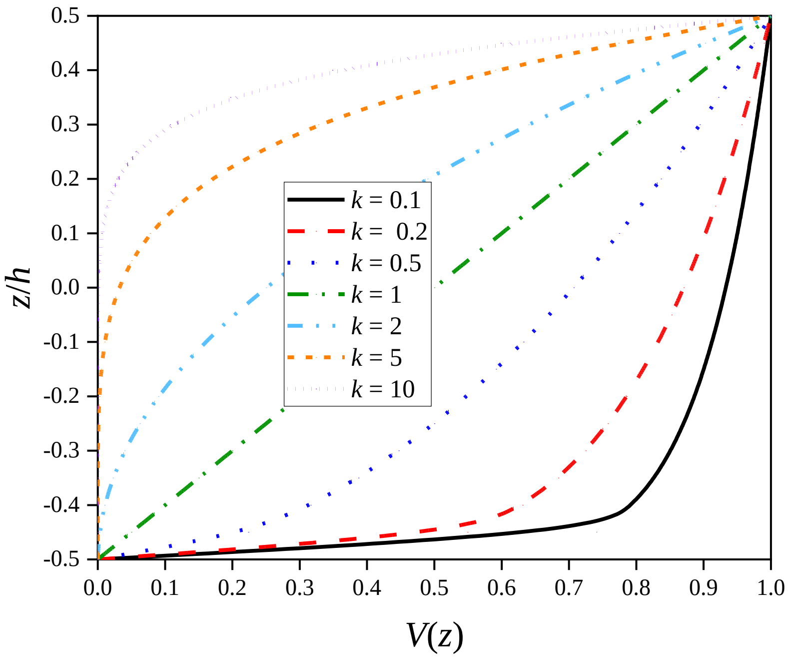

Figure 1.15 The volume fraction variation throughout the thickness of the P-FGM plate.

1.8.2 Exponential-law function (E-FGM)

This model is extensively employed in analyzing the fracture mechanics of FGM [80]. The effective properties within the E-FGM plate are assumed to vary continuously along the thickness direction following the exponential expression, as shown in **Figure 1.16**, with

$$P(z) = P_1 e^{n\left(\frac{1}{2}+\frac{z}{h}\right)}, P_2 = e^n, n \neq 0 \tag{1.6}$$

n is the exponential index.

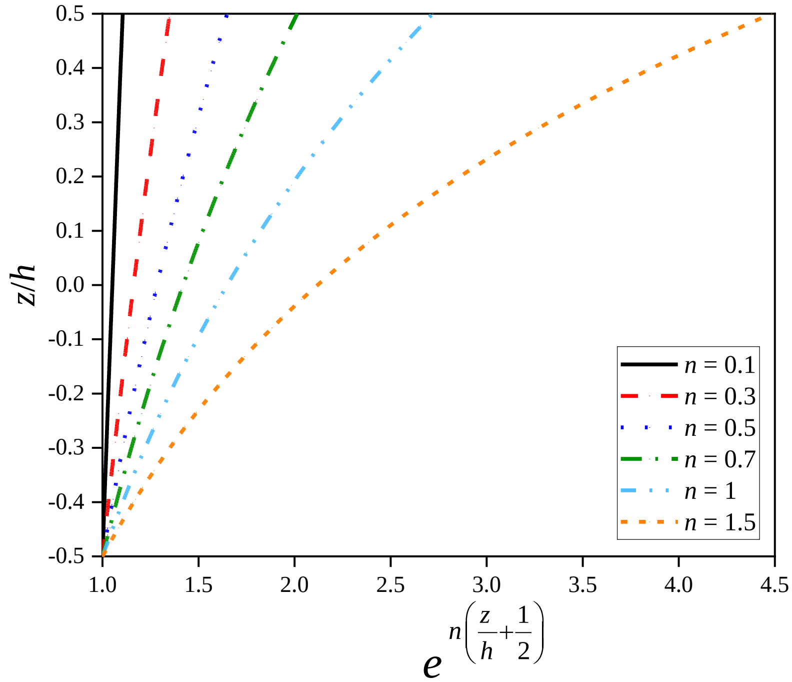

Figure 1.16 The exponential function variation throughout the thickness of the E-FGM plate.

1.8.3 Sigmoidal-law function (S-FGM)

In both power-law and exponential gradation models, stress concentrations tend to develop at interfaces where the material changes rapidly, despite being continuous. To address this issue, Chung and Chi [81] introduced the sigmoid FGM, which utilizes two power-law functions to define a modified volume fraction. Later, Chi and Chung [82] demonstrated that employing a sigmoid FGM could notably decrease the stress intensity factors in structures with cracks. The two power-law functions are defined by:

$$V(z) = \frac{1}{2}\left(1 + \frac{2z}{h}\right)^k \quad \text{for } 0 \leq z \leq \frac{h}{2} \tag{1.7}$$

$$V(z) = 1 - \frac{1}{2}\left(1 - \frac{2z}{h}\right)^k \quad \text{for } -\frac{h}{2} \leq z \leq 0 \tag{1.8}$$

k is the sigmoid index.

Figure 1.17 displays the variation of volume fraction described in Eqs. (1.7) and (1.8) across the thickness of the S-FGM plate.

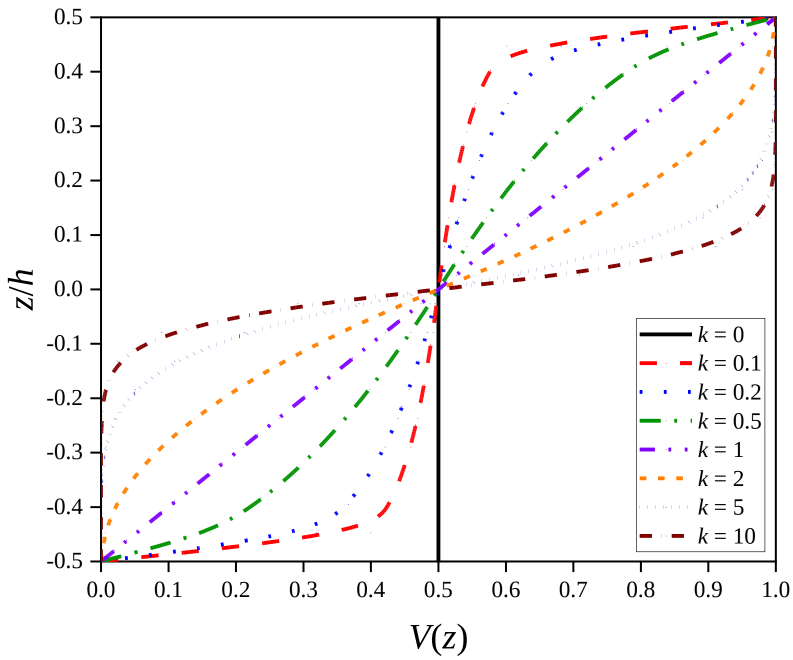

Figure 1.17 The volume fraction variation throughout the thickness of the S-FGM plate.

1.9 Theories for analyzing FGM structures

The structural analysis of FGMs can be approached through either three-dimensional (3D) elasticity theory or simplified models known as equivalent single-layer (ESL) theories. While 3D elasticity provides the most accurate representation of stress and deformation, it is often computationally intensive. ESL theories, on the other hand, offer a more practical alternative by introducing reasonable assumptions about how deformation occurs through the structure's thickness. These theories vary in complexity based on how they handle shear and normal deformations. The most basic among them is the classical plate theory (CPT), also referred to as Kirchhoff theory. CPT assumes that plane sections remain plane and perpendicular to the mid-surface, effectively ignoring both transverse shear and normal deformations. As a result, it is only valid for very thin FG structures. To extend applicability to moderately thick plates, the first-order shear deformation theory (FSDT), developed by Mindlin, was introduced. This model accounts for shear deformation by allowing in-plane displacements to vary linearly through the thickness. However, FSDT requires the use of a shear correction factor to compensate for the simplified shear strain distribution—an aspect that complicates its implementation, as the correction factor is influenced by geometry, boundary conditions, and loading types. To overcome this limitation, higher-order shear deformation theories (HSDTs) were developed. These advanced models expand the displacement fields into higher-order terms with respect to the thickness coordinate. Unlike FSDT, HSDTs naturally capture the shear strain distribution without needing a correction factor, and their accuracy can be improved systematically by including additional terms in the expansion.

1.9.1 Classical plate theory (CPT)

Classical plate theory has a long history, dating back to the eighteenth century. The CPT is based on Cauchy [83], Poisson [84], and Kirchhoff [85] assumptions, which extend the principles of the Euler-Bernoulli beam theory to the plate. The fundamental assumptions of CPT are:

- The plate is considered thin, typically defined by the condition that its thickness is small relative to its other dimensions ($a/h \geq 10$).
- The deflections of the plate are small compared to its overall dimensions.
- Normal lines to the mid-surface before deformation remain straight, normal, and inextensible after deformation (**Figures 1.18** and **1.19**).
- Deformations due to transverse shear are neglected ($\tau_{xz} = \tau_{yz} = 0$).
- Normal strains and stresses in the out-of-plane direction are also assumed negligible ($\sigma_z = 0$, $\varepsilon_z = 0$).

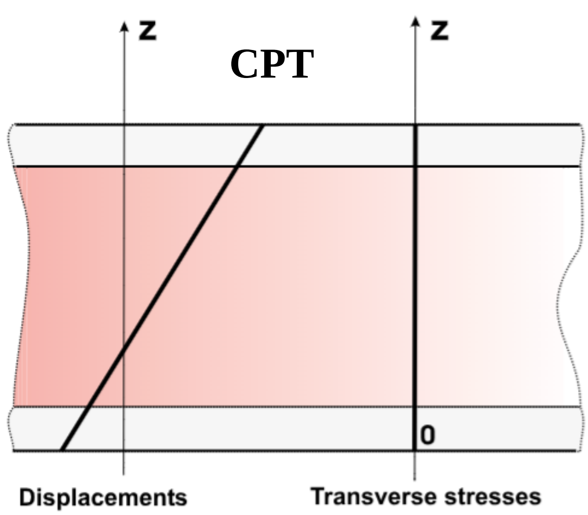

Figure 1.18 Analysis of displacements and transverse stresses in CPT. [86]

These simplifications make the classical theories more suited for thin structures. However, it yields inaccurate results for thick structures, where shear deformation effects are more notable [87].

The deformation in classical theories can be described by the deformation of the mid-surface, reducing the theory to a 2D description with three variables. The displacement field in the CPT is expressed as follows [88]:

$$\begin{aligned} u(x,y,z) &= u_0(x,y) - z\frac{\partial w_0(x,y)}{\partial x}, \\ v(x,y,z) &= v_0(x,y) - z\frac{\partial w_0(x,y)}{\partial y}, \\ w(x,y,z) &= w_0(x,y) \end{aligned} \tag{1.9}$$

where u_0, v_0, and w_0 represent the displacements along the x, y, and z directions of a point located at the mid-surface ($z = 0$). Note that u_0 and v_0 correspond to the extensional deformations of the plate, while w_0 refers to the bending deformation.

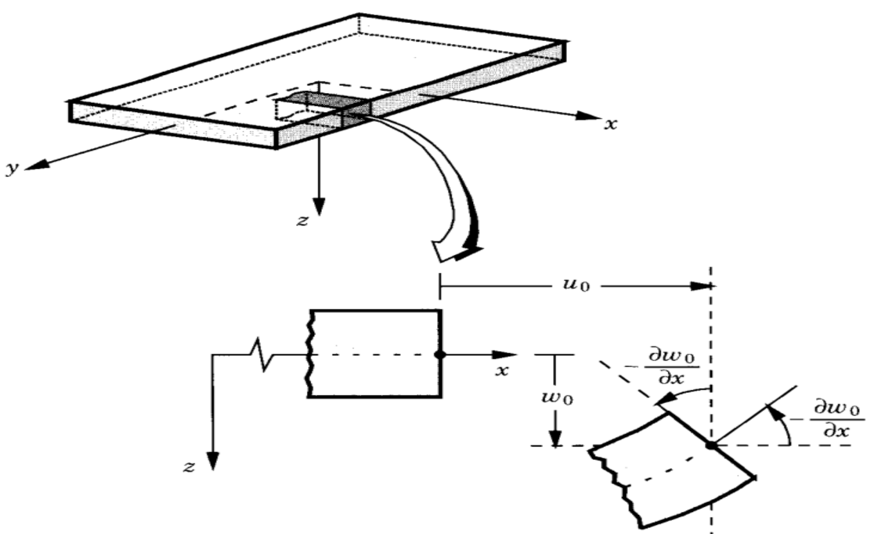

Figure 1.19 Analysis of plate edge deformation based on Kirchhoff assumptions. [88]

Aron [89] applied the Poisson-Kirchhoff plate hypothesis to develop a classical shell theory (CST), deriving equations for shell bending under small strains and finite displacements. However, Love [90] later identified and corrected errors in Aron's theory. CST shares similar assumptions with CPT but is specifically designed for thin shells, characterized by the criterion ($h/R_{min} \leq 1$) where R_{min} is the smallest radius of curvature.

1.9.2 First-order shear deformation theory (FSDT)

The first-order shear deformation theory (FSDT) provides a refinement over the CPT by incorporating the effects of transverse shear deformation, which become significant in moderately thick plates. Developed by Reissner [91, 92] and Mindlin [93], FSDT assumes that transverse shear strains remain constant through the plate's thickness. However, this simplification violates the free traction conditions at the top and bottom surfaces of the plate. To address this inconsistency, a shear correction factor (SCF) is introduced, allowing for more accurate estimation of shear stresses and compliance with boundary conditions. According to this theory:

- The transverse normal stress is negligible ($\sigma_z = 0$).
- Transverse normal to the mid-surface before deformation remains inextensible after deformation.
- The transverse normal remains straight but not perpendicular to the mid-surface after deformation (**Figure 1.20** and **1.21**).

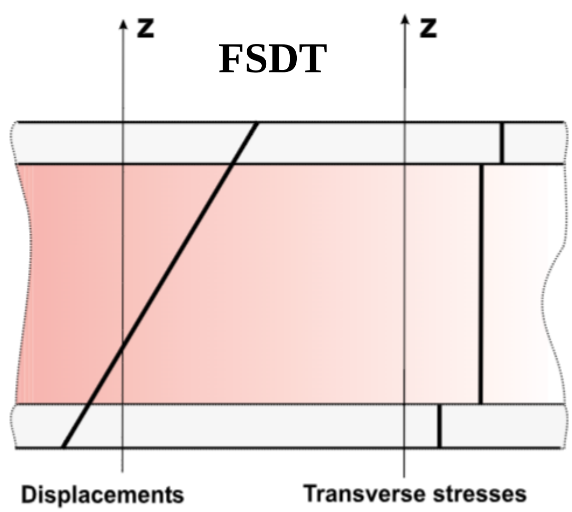

Figure 1.20 Analysis of displacements and transverse stresses in FSDT. [86]

The displacement field in the FSDT is expressed as follows [88]:

$$u(x,y,z) = u_0(x,y) + z\emptyset_x(x,y),$$
$$v(x,y,z) = v_0(x,y) + z\emptyset_y(x,y), \quad (1.10)$$
$$w(x,y,z) = w_0(x,y)$$

where u_0, v_0, and w_0 represent the mid-surface displacements along the *x, y*, and *z* directions, respectively, while ϕ_x and ϕ_y and represent the rotations of a transverse normal to the mid-surface about the respectively. In the case of the CPT, these rotations are directly related to the slope of the transverse displacement, given by:

$$\emptyset_x = -\frac{\partial w_0(x, y)}{\partial x}, \quad \emptyset_y = -\frac{\partial w_0(x, y)}{\partial y} \tag{1.11}$$

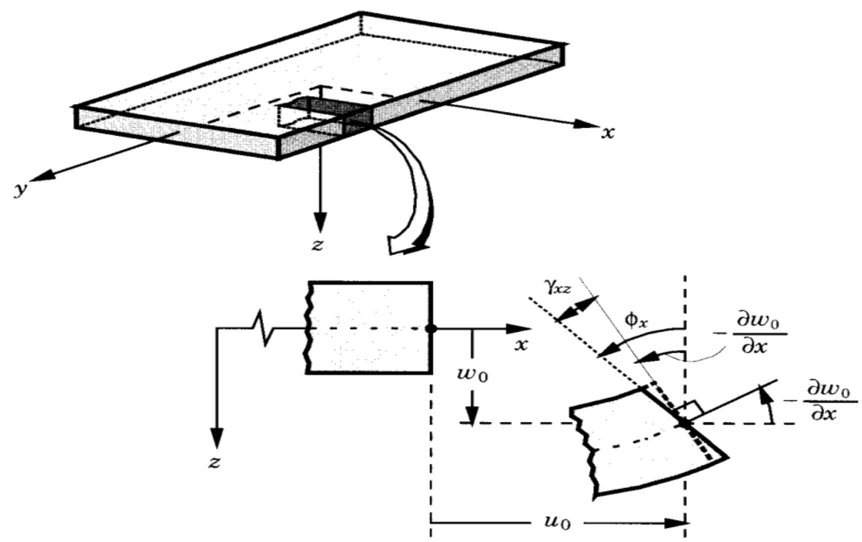

Figure 1.21 Analysis of plate edge deformation based on FSDT assumptions. [88]

While FSDT provides a reasonably accurate description of the overall response of thin and moderately thick plates, calculating the shear correction factor can be challenging, especially for complex geometries [94]. Additionally, FSDT may experience shear-locking phenomena when the thickness-to-length ratio decreases significantly [95].

1.9.2.1 Shear correction factor (SCF)

The shear correction factor, denoted as k_s, is added to correct the discrepancy between the actual distribution of 3D transverse shear stresses and those assumed in the FSDT. This factor is introduced as a parameter in the constitutive relations between the transverse shear forces and the transverse shear strains. For isotropic homogeneous materials, the initial SCF was introduced by Reissner [91, 96, 97]. He proposed a value of 5/6, which has been widely adopted, based on a calculation method that considers static equilibrium and energy equivalence. Later, Mindlin [93] proposed a value of $\pi^2/12$ utilizing dynamic analysis, equating the approximate first antisymmetric thickness-shear vibration frequency to the exact solution. Ayad [98] introduced an alternative approach for determining the SCF. It involves comparing the shear energy calculated using equilibrium equations with that obtained by the FSDT. Noor et al. [99-101] suggested a method using predictor-corrector procedures to adjust SCF through an iteration process. However, this method depends on specific boundary conditions, geometry, and loading conditions, making it unsuitable for other analyses.

In general, the value of SCF utilized for analyzing isotropic homogeneous structures is 5/6. Nevertheless, this value may not be suitable for FGM analyses due to the continuous variation of material properties through the structure's thickness.

1.9.3 Higher-order shear deformation theory (HSDT)

Unlike the CPT, which neglects shear deformations, and the FSDT, which assumes a linear variation of in-plane displacements and constant transverse shear strains through the plate's thickness, higher-order shear deformation theories (HSDTs) incorporate a nonlinear distribution of displacements. This enables HSDTs to accurately capture the parabolic variation of transverse shear stresses through the thickness, satisfying the free traction conditions on the top and bottom surfaces without requiring a SCF, as illustrated in **Figure 1.22**.

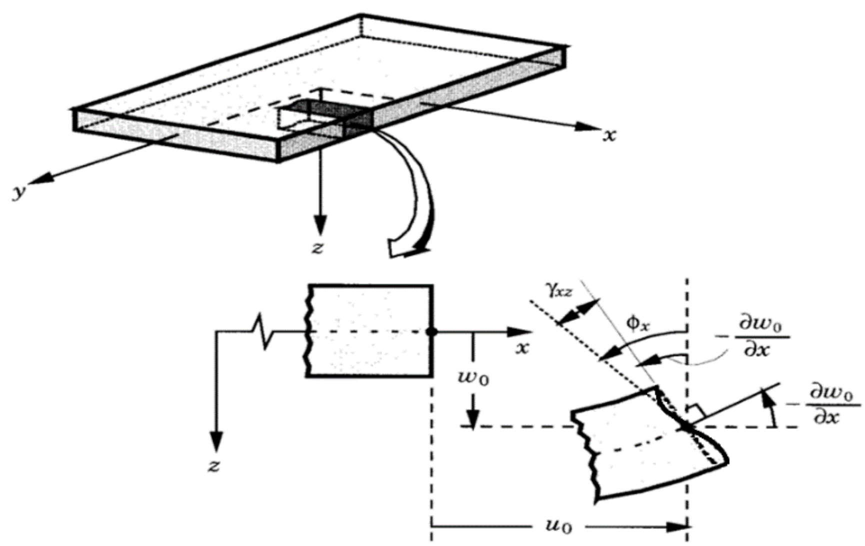

Figure 1.22 Analysis of plate edge deformation based on HSDT assumptions. [88]

The majority of HSDTs rely on the Taylor series expansion of displacement fields to approximate the 3D theory [102]. This assumption leads to the following form for the displacement:

$$u_i(x,y,z) = u_i(x,y) + z\emptyset_i^{(1)}(x,y) + \ z^2\emptyset_i^{(2)}(x,y) + \ldots + z^j\emptyset_i^{(j)}(x,y) \tag{1.12}$$

Where i = 1, 2, 3 and j represents the order applied in the theory.

The FSDT is equivalent to the Taylor series expansion up to the order j = 1, and $\phi_3^{(1)} = 0$. The second-order shear deformation theory (SCSDT) [103-106] presents superior results to the FSDT, yet shares the same limitations, necessitating correction factors. The displacement filed in this theory is formulated as:

$$\begin{aligned} u(x,y,z) &= u_0(x,y) + z\emptyset_x(x,y) + z^2\psi_x(x,y), \\ v(x,y,z) &= v_0(x,y) + z\emptyset_y(x,y) + z^2\psi_y(x,y), \\ w(x,y,z) &= w_0(x,y) + z\emptyset_z(x,y) + z^2\psi_z(x,y) \end{aligned} \tag{1.13}$$

Where ψ_x, ψ_y, ψ_z are the second-order functions.

The third-order shear deformation theory (TSDT), which was developed by Reddy [107] for laminated composite plates, incorporates the transverse shear deformation effect and fulfills the zero-traction conditions on both the top and bottom surfaces of a plate. The displacement field for TSDT is expressed as:

$$\begin{aligned} u(x,y,z) &= u_0(x,y) + z\emptyset_x(x,y) + z^2\psi_x(x,y) + z^3\zeta_x(x,y), \\ v(x,y,z) &= v_0(x,y) + z\emptyset_y(x,y) + z^2\psi_y(x,y) + z^3\zeta_y(x,y), \\ w(x,y,z) &= w_0(x,y) \end{aligned} \tag{1.14}$$

Where ψ_x, ψ_y, ζ_x, ζ_y are the third-order functions.

As the order of expansion increases, so does the number of additional functions, which can become challenging to interpret. To simplify this, adjustments have been made to reduce the number of displacement parameters. One approach is to truncate the last terms of the Taylor series by introducing a "transverse shear function." Then, the general displacement field for HSDT is written as follows:

$$u(x,y,z) = u_0(x,y) - z\frac{\partial w_0(x,y)}{\partial x} + f(z)\theta_x(x,y)$$

$$v(x,y,z) = v_0(x,y) - z\frac{\partial w_0(x,y)}{\partial y} + f(z)\theta_y(x,y), \tag{1.15}$$

$$w(x,y,z) = w_0(x,y)$$

Where u_0, v_0, and w_0 represent the membrane displacements. while

$$\theta_x = \frac{\partial w_0}{\partial x} + \phi_x, \qquad \theta_y = \frac{\partial w_0}{\partial y} + \phi_y \tag{1.16}$$

with ϕ_x, ϕ_y are the rotations along the x, and y-axes, respectively.

$f(z)$ is the shear function, which determines the distribution of transverse shear strains and stresses across the plate's thickness h.

The CPT is derived by setting $f(z) = 0$, and FSDT is derived by setting $f(z) = z$. Furthermore, Reddy's TSDT displacement field is obtained by employing the subsequent function [107]:

$$f(z) = z - \frac{4z^3}{3h^2} \tag{1.17}$$

Various researchers have made notable advancements in HSDT models, particularly in defining the shear function $f(z)$. These models are characterized by a nonlinear distribution of displacement fields through the thickness and are capable of representing the warping of the cross-section in its deformed state. **Table 1.2** demonstrates various transverse shear functions that have been proposed to approximate the mechanical response of structures to the exact 3D elasticity solution as closely as possible.

Table 1.2 The transverse shear function models.

HSDT Models	**Reference**	***f(z)***
Polynomial functions	Ambartsumain [108] Panc [109], Reissner [110] Levinson [111], Murthy [112], Reddy [107] Nguyen-Xuan et al. [113]	$f(z)=\frac{h^2}{8}z-\frac{z^3}{6}$ $f(z)=\frac{5z}{4}-\frac{5z^3}{3h^2}$ $f(z)=z-\frac{4z^3}{3h^2}$ $f(z)=\frac{7z}{8}-\frac{2z^3}{h^2}+\frac{2z^5}{h^4}$
Trigonometric functions	Levy [114], Stein [115], Touratier [116] Arya et al. [117] Thai et al. [118]	$f(z)=\frac{h}{\pi}\sin\left(\frac{\pi z}{h}\right)$ $f(z)=\sin\left(\frac{\pi z}{h}\right)$ $f(z)=-z+htan^{-1}\left(\frac{2z}{h}\right)$
Hyperbolic functions	Soldatos [119] El Meiche et al. [120] Akavci and Tanrikulu [121]	$f(z)=hsinh\left(\frac{z}{h}\right)-zcosh(\frac{1}{2})$ $f(z)=\frac{\frac{h}{\pi}\sinh\left(\frac{\pi z}{h}\right)-z}{\cosh\left(\frac{\pi}{2}\right)-1}-z$ $f(z)=\frac{3\pi h}{2}\tanh\left(\frac{\pi}{h}\right)-\frac{3\pi z}{2}sech^2\left(\frac{1}{2}\right)$
Exponential functions	Karama et al. [122] Aydogdu [123] Mantari et al. [124]	$f(z)=ze^{-2(\frac{z}{h})^2}$ $f(z)=z\times\alpha^{\frac{-2}{\ln(\alpha)}(\frac{z}{h})^2},\alpha>0$ $f(z)=z\times 2.85^{-2(\frac{z}{h})^2}+0{,}028z$
Combination functions	Mantari et al. [125] Thai et al. [126] Thai et al. [126]	$f(z)=\sin\left(\frac{\pi z}{h}\right)\times e^{\frac{1}{2}\cos\left(\frac{\pi z}{h}\right)}+\frac{\pi z}{2h}$ $f(z)=tan^{-1}\left[\sin(\frac{\pi z}{h})\right]$ $f(z)=sinh^{-1}\left[\sin(\frac{\pi z}{h})\right]$

While HSDTs do not require a shear correction factor, their equations of motion are more complex and laborious than those of FSDTs. To simplify the analysis, Shimpi [127] developed a refined plate theory (RPT), which separates the transverse displacement into bending and shear components. This theory involves only four unknowns, does not need an SCF, and provides a parabolic distribution of shear through the plate's thickness. Additionally, it shares many similarities with the CPT in terms of equations of motion, boundary conditions, and stress resultant expressions. The displacement field in the RPT is represented as follows:

$$u(x,y,z) = u_0(x,y) - z\frac{\partial w_b(x,y)}{\partial x} - f(z)\frac{\partial w_s(x,y)}{\partial x},$$

$$v(x,y,z) = v_0(x,y) - z\frac{\partial w_b(x,y)}{\partial y} - f(z)\frac{\partial w_s(x,y)}{\partial y}, \tag{1.18}$$

$$w(x,y,z) = w_b(x,y) + w_s(x,y)$$

where w_b and w_s represent the bending and shear components of transverse displacement, respectively.

The after-mention theories ignore the thickness stretching effect (i.e., ε_z = 0) because they assume a constant transverse displacement throughout the thickness. This effect becomes significant in moderately thick and thick structures and should be considered. Quasi-3D theories are advanced shear deformation theories that incorporate higher-order variations of both in-plane and transverse displacements through the thickness. As a result, they account for both the shear deformation effect and the thickness stretching effect [128]. The displacement field in the quasi-3D theory is given by:

$$u(x,y,z) = u_0(x,y) - z\frac{\partial w_0(x,y)}{\partial x} + f(z)\varphi_x(x,y)$$

$$v(x,y,z) = v_0(x,y) - z\frac{\partial w_0(x,y)}{\partial y} + f(z)\varphi_y(x,y), \tag{1.19}$$

$$w(x,y,z) = w_0(x,y) + g(z)\varphi_z(x,y)$$

The six unknown displacements of the midplane of the plate are denoted by u_0, v_0, w_0, φ_x, φ_y, and φ_z. Additionally, $f(z)$ and $g(z)$ are shear functions with

$$g(z) = \frac{df(z)}{dz} \tag{1.20}$$

1.9.4 Literature reviews on the analysis of FG plates and shells

With the rising interest in FGMs in recent years, extensive research has been conducted to predict the bending and dynamic response of FG plates and shells [129, 130]. Various analytical and numerical methods have been developed, offering different levels of complexity and accuracy depending on factors such as boundary conditions, loading types, and material gradation profiles. These methods range from simplified analytical solutions for basic cases to advanced numerical approaches capable of handling complex geometries, making them essential tools for accurately assessing FGM behavior in practical applications.

For a precise FG structures analysis, 3D elasticity theory is generally preferred. However, applying the theory to doubly curved shells (DCSs) is challenging due to the effects of curvature and the complexity of the mathematical calculations involved. To overcome these difficulties, researchers have developed approximate shell theories based on specific kinematic assumptions, transforming 3D problems into 2D problems. These theories are typically categorized into three main types: equivalent single-layer, layerwise, and zig-zag theories. Numerous studies have demonstrated that equivalent single-layer theories can effectively capture the bending and dynamic behavior of FG structures without the need for complex computational efforts. Hence, this review focuses exclusively on the literature related to equivalent single-layer theories.

Classical plate theory (CPT) is one of the earliest and simplest approaches. CPT assumes that transverse shear deformation is negligible, making it ideal for thin structures. Loy et al. [131] explored the vibration characteristics of FG cylindrical shells utilizing the Rayleigh-Ritz method. Reddy et al. [132] studied the axisymmetric bending response of FG circular and annular plates, using exact solutions through CPT. Pradhan et al. [133] investigated the natural frequency of FG cylindrical shells under various boundary conditions using the Rayleigh method. Later, Naeem et al. [134] revisited this work through the Ritz method. Ng et al. [135] examined the dynamic stability of FG rectangular plates subjected to harmonic in-plane loading using Bolotin's method. Wo and Meguid [136] explored the large deflections of FG plates and shells subjected to transverse loading and temperature variations by employing the Fourier series. Yang and Shen [137] combined the differential quadrature approximation, the Galerkin procedure, and the modal superposition method to analyze the vibration and transient response of initially stressed thin FG plates subjected to an impulsive lateral patch load and lying on an elastic foundation. Najafizadeh and Eslami [138] presented a closed-form solution to analyze the buckling of FG circular plates under radial loading. Ma and Wang [139] explored the axisymmetric large deflection bending and post-buckling behavior of FG circular plates considering mechanical, thermal, and combined thermal-mechanical loadings using shooting method. Tsukamoto [140] analyzed the transient thermal stresses of FG plates subjected to heat flow, integrating micromechanical and macromechanical approaches. Woo et al. [141] investigated the natural frequency of FG plates under thermal conditions utilizing a mixed Fourier series. Arshad et al. [142] examined the vibration characteristics of FG cylindrical shells using the Rayleigh-Ritz method in conjunction with three different volume fraction laws.

Ebrahimi and Rastgo [143] studied the free vibration behavior of thin FG circular plates embedded with two uniformly distributed piezoelectric (PZT4) actuator layers via CPT. Alinia and Ghannadpour [144] minimized the total potential energy to examine the nonlinear responses of FG plates subjected to transverse pressure. Alijani et al. [145] explored the nonlinear vibrations of FG shallow shells using multi-modal Galerkin discretization. Hu and Zhang [146] studied the vibration and stability of the FG plate under in-plane excitation by employing both the Galerkin method and the multiscale method. Ebrahimi and Najafizadeh [147] investigated the vibrational behavior of FG cylindrical shells by applying the generalized differential quadrature and generalized integral quadrature methods. Du and Li [148] investigated the natural frequency of FG cylindrical shells exposed to thermal conditions using the multiple-scale method. In a related study, Du et al. [149] examined the nonlinear forced vibration of infinitely long FG cylindrical shells. Chakraverty and Pradhan [150] employed the Rayleigh-Ritz method to analyze the vibration characteristics of FG plates resting on an elastic foundation under different boundary conditions. Subsequently, they [151] extended their work by incorporating the effects of thermal conditions. Ruan et al. [152] examined the transverse vibrations and stability of a moving skew FG plate. Davar and Azarafza [153] developed a novel mathematical model based on the physical neutral surface to determine the natural frequencies of FG annular circular plates. It is important to recognize that stretching–bending coupling occurs in FG structures due to the variation of material properties through their thickness. As a result, the neutral surface of an FG structure does not align with its middle surface. This coupling could be removed if the governing equations were formulated based on the neutral surface. Zhang and Zhou [154] validated this by reformulating CPT for FG plates concerning the neutral surface. Damanpack et al. [155] employed the boundary element method alongside the physical neutral surface for the static analysis of FG plates.

While CPT offers fast computational solutions, it fails to account for the effects of transverse shear stresses, therefore provides inaccurate results of displacements, and stresses for thick structures. To enhance the performance upon CPT, Reissner [110] and Mindlin [93] introduced the first-order shear deformation theory (FSDT). Models based on FSDT predict a uniform transverse shear stress distribution through the thickness, as they assume a constant transverse displacement field. Chen [156] studied the fundamental frequency of FG plates using the Galerkin method and the Runge–Kutta method. Liew et al. [157] formulated eigenvalue equation to investigate the natural frequencies of cylindrical shells composed of a coating-FGM-substrate structure. Ferreira et al. [158] employed the Mori–Tanaka and multiquadric radial basis functions to analyze the free vibration behavior of FG plates. Sheng and Wang [159] combined the normal mode expansion and the Bolotin method to analyze the vibration and buckling response of FG cylindrical shells embedded in an elastic medium. Zhang and Zhou [154] investigated FG thin plates' bending, vibration, and buckling behavior using the physical neutral surface approach. Tornabene and Viola [160] investigated the free vibration behavior of FG shells by combining the FSDT with the GDQ method. Later, Tornabene [161] analyzed the natural frequencies of FG conical, cylindrical shells, and annular plates. Tornabene and Viola [162] employed four types of power-law distribution to determine the natural frequencies and the mode shapes of FG parabolic shells. Zhao et al. [163, 164], and Zhao and Liew [165, 166] developed a meshless model using FSDT and the element-free kp-Ritz method. The model was applied to FG plates and shells for various analyses, including vibration [167], bending [166], and thermal bending [168]. Hosseini-Hashemi et al. [169] proposed an analytical solution to examine the natural frequency of FG plates resting on Winkler or Pasternak elastic foundations. Later on, Hosseini-Hashemi et al. [170] proposed an exact closed-form solution for the free vibration analysis of FG plates. Zhang and Hao [171] employed the Galerkin method to analyze the frequency of FG cylindrical shells subjected to thermal loadings and external excitations. Alijani et al. [172] presented a multi-modal energy approach to analyze the effect of temperature on the nonlinear frequency of FG plates. Fallah et al. [173] analyzed the effect of boundary conditions and Winkler parameters on the natural frequency of FG plates via the extended Kantorovich method. Kiani et al. [174] employed an analytical hybrid Laplace–Fourier transformation to analyze the center deflection and frequency of FG panels subjected to mechanical and thermal loadings. Banijamali and Jafari [175] studied the frequencies and critical speeds of FG rotating truncated conical shells reinforced with anisogrid lattice structures using GDQ. Thai and Choi [176] presented Navier solution based on a refined FSDT plate theory to investigate the bending, stresses, and free vibration of FG plates. Memar Ardestani et al. [177] investigated the static behavior of concentrically and eccentrically FG stiffened plates subjected to transverse loadings using the reproducing kernel particle method.

Isvandzibaei et al. [178] combined the Ritz method and FSDT to analyze the impact of pressure loading on the vibration properties of FG cylindrical shells subjected to pressure loading. Su et al. [179] studied the vibration characteristics of cylindrical, conical, and spherical shells, using a modified Fourier series combined with the Rayleigh-Ritz method. Xiang et al. [180] analyzed the fundamental frequencies of FG cylindrical shells utilizing local collocation meshless. Rezaei et al. [181] examined the free vibration characteristics of porous FG plates by employing the variational method in conjunction with a four-variable FSDT. Zhang et al. [182] introduced a modified Fourier cosine series method to analyze the free vibration behavior of moderately thick FG cylindrical shells. Duc et al. [183] applied the Runge-Kutta method to explore the nonlinear behavior of porous FG plates on an elastic foundation under thermal and mechanical conditions. Fan et al. [184] utilized the Walsh series method to conduct a vibration characteristics analysis of FG cylindrical shells. Awrejcewicz et al. [185] applied the variational Ritz method combined with the R-functions method to investigate the natural frequencies of FG shallow cylindrical shells. Chen et al. [186] investigated the bending and buckling behavior of porous FG plates using the Chebyshev-Ritz method. Trinh et al. [187] utilized the Bubnov–Galerkin approach to investigate the natural frequencies and nonlinear dynamic responses of FG porous sandwich shells subjected to thermomechanical loading. Babaei et al. [188] employed a two-step perturbation technique to analyze the natural frequencies of FG cylindrical panels resting on a nonlinear elastic foundation. Shahbaztabar et al. [189] derived the eigenvalue equation to investigate the natural frequencies of fluid-filled FG cylindrical shells embedded in a Pasternak elastic foundation. Baghlani et al. [190] investigated the vibration characteristic of partially fluid-filled FG cylindrical shells embedded in Pasternak elastic foundations within a thermal environment using the Fourier series and finite strip element. Liu et al. [191] used the wave-based method to analyze the fundamental frequency of FG cylindrical shells under various boundary conditions. Cao et al. [192] examined the impact of external pressure on the vibration and buckling behavior of FG spherical panels supported by an elastic medium, utilizing the Ritz formulation. Anamagh and Bediz [193] analyzed the eigenvalue buckling and vibration properties of FG porous plates reinforced with graphene platelets via the spectral Chebyshev method. Bagheri et al. [194] investigated the natural frequency of a FG joined conical-spherical shell using a semi-analytical approach that combines the Fourier series with the

GDQ method. Vinh et al. [195-197] explored the effect of variable nonlocal parameters on the vibration behavior of nanostructures via the Navier technique. Kurpa and Shmatko [198] studied the vibration characteristics of the porous FG shells lying on an elastic foundation using the Ritz method.

FSDT accounts for transverse shear stresses in thin and moderately thick structures, but it falls short of meeting the actual shear stress conditions at the top and bottom surfaces. This led to the development of high-order shear deformation theories (HSDTs), which take into consideration both transverse shear and normal deformations. Yang and Shen [199] explored the thermal impact on the free vibration behavior and dynamic instability of FG cylindrical panels under both static and periodic axial forces using a semi-analytical approach. Carrera et al. [200] utilized various HSDT shell theories, derived from CUF, for the bending analysis of FG shells. Alijani et al. [201] examined the vibrations of FG DCSs under thermal variations and harmonic excitation using a multi-modal energy approach. Oktem et al. [202] utilized a boundary-discontinuous generalized double Fourier series approach to analyze the bending response of FG shells. Thai and Vo [203] conducted bending and dynamic analyses of FG plates using the Navier method. Zidi et al. [204] examined the bending behavior of an FG plate subjected to hygrothermal and mechanical loading via the Navier approach. Shen and Wang [205] employed both Vogit and Mori-Tanaka models to analyze the frequency of FG cylindrical panels resting on elastic foundations. Tornabene et al. [206] utilized ESL theories derived from the CUF, including the zig-zag effect, to study the natural frequency of FG shells. Akavci and Tanrikulu [207] studied the bending and vibration characteristics of FG plates via power-law, exponential, and Mori–Tanaka model distributions. Fantuzzi et al. [208] explored the free vibration of FG cylindrical and spherical panels based on 2D GQD models. Tornabene et al. [209] conducted an analysis of free vibrations in FG sandwich shells with varying thicknesses based on the GDQ. Dong et al. [210] utilized the Galerkin method and the fourth-order Runge–Kutta method to study the natural frequencies and dynamic nonlinear responses of sandwich shells. Wang and Zu [211] studied the large amplitude vibration of sigmoid FG porous plates via the Galerkin method. Punera and Kant [212] conducted a vibration analysis of FG open cylindrical panels using a Navier solution based on several refined HSDTs. Chen et al. [213] introduced a novel shear deformation theory that accounts for stretching effects, extending Reddy’s TSDT, to analyze the free vibration of FG shells. Mehar and Panda [214] investigated the bending behavior of FG-CNTRC panels with various gradings subjected to a uniform thermal environment using the variational method. Sayyad and Ghugal [215] developed a unified shear deformation theory for the bending analysis of softcore and hardcore FG sandwich beams and plates. Ghumare and Sayyad [216] proposed Navier's solution based on a new fifth-order SDT for the bending analysis of FG plates. This theory was later extended by Shinde and Sayyad [217] to analyze FG sandwich plates. Lie and Tong [218] explored the free and forced vibration behaviors of FG-GRC cylindrical shells under thermal conditions. Huu Quoc et al. [219] investigated the vibrational response of FG-CNT plates using Navier approach. Subsequently, Van Tham et al. [220] extended the work by applying the analysis to FG-CNT shells.

Hong [221] investigated the free vibration behavior of cylindrical shells exposed to a thermal environment using TSDT. Guellil et al. [222] analyzed FG plates resting on elastic foundations, considering the effects of different boundary conditions, using the Navier solution. Sayyad and Ghugal [223] employed a generalized higher-order shell theory via a unified formulation to analyze the bending and free vibration of FG DCSs. Kouider et al. [224] explored the bending and free vibration of FG sandwich plates using the Navier method. Shinde and Sayyad [225] examined the bending and vibration of FG sandwich plates and shells via a novel fifth-order shear and normal deformation theory. Rachid et al. [226] proposed refined 2D and quasi-3D theories to the mechanical response of FG shells resting on elastic foundations. Later on, Rachid et al. [227] studied the natural frequency of FG shells accounting for temperature-dependent and temperature-independent heat conduction. Djilali et al. [228] conducted a bending analysis of FG-CNT plates, considering the effects of a thermal environment using a simple integral HSDT. Talebi et al. [229] studied the dynamic thermal snap-through behavior of porous FG spherical with temperature-dependent properties via the multi-term Ritz–Chebyshev method. Shmakto et al. [230] analyzed the natural frequencies of FG sandwich shells resting on elastic foundations based on the R-functions theory combined with the variational Ritz method. Alnujaie et al. [231] examined the multi-directional FG sandwich plates' vibration characteristics and buckling using Navier's solution. Aris and Ahmadi [232] studied the natural frequency of rotating stiffened truncated FG conical shells within a thermal environment using Galerkin's technique. Draiche et al. [233] developed an enhanced mathematical model based on a newly refined HSDT with only four variables for FG DCSs' bending and dynamic analysis. Tamnar and Sayyad [234] applied the Navier approach to study the bending and free vibration of FG porous shallow shells. Belhachemi et al. [235] used 2D and quasi-3D HSDTs to analyze FG shells statistically. Daikh et al. [236]

investigated the impact of boundary conditions on vibration eigenvalues using a novel analytical approach involving a hyperbolic sine function.

The studies mentioned above emphasize the significant use of analytical methods to investigate the mechanical behavior of FG structures. However, these approaches encounter challenges when accounting for intricate factors like irregular geometry and boundary conditions, non-linear material behaviors, and varied loading scenarios. To overcome these difficulties, researchers have increasingly adopted numerical techniques, particularly the finite element method (FEM) [237-239]. FEM allows for local refinement of the mesh, enabling more accurate results in regions of interest without the need for simplifying assumptions that can compromise accuracy. Della Croce and Venini [240] developed a hierarchical family of finite elements for the bending analysis of FG plates under mechanical and thermal loads, applying a variational formulation. Patel et al. [241] investigated the free vibration characteristics of FG elliptical cylindrical shells using a Q8-C^0 serendipity quadrilateral shell element with 11 DOF. Das et al. [242] introduced a novel triangular FE model based on the 2nd and 3rd-order single-layer theory, designed for the thermo-elastic analysis of sandwich panels with an FG core. Arciniega and Reddy [243] conducted a geometrically nonlinear analysis of FG shells utilizing a tensor-based FE formulation with curvilinear coordinates. Reddy and Chin [244] examined the dynamic behavior of FG plates and cylinders under two types of thermal loading. Kim et al. [245] proposed a Q4 quasi-conforming shell element to analyze the linear and nonlinear deflection behavior of FG plates and shells. Prakash et al. [246] employed a Q8-C^0 isoparametric continuous element along with a neutral surface to examine the nonlinear stability of FG skew plates under in-plane loadings. Singha et al. [247] also applied the neutral surface effect to investigate the nonlinear bending of FG plates under transverse loading using a Q4-C^1 isoparametric element with 10 DOF. Pradyumna and Bandyopadhyay [248, 249] proposed a Q9-C^0 isoparametric model based on HSDT to determine the natural frequencies of FG panels in both the presence and absence of a thermal condition. Santos et al. [250] developed a semi-analytical axisymmetric 3D FE model to investigate the thermoelastic behavior of FG cylindrical shells under transient thermal shock loading. Asgari et al. [251] conducted a comparison of the stress distribution and dynamic response of FG cylindrical shells using the FEM and Newmark integration technique. Talha and Singh [252] utilized a Q9-C^0 isoparametric element with 13 DOF to examine the bending and vibration behavior of FG plates. Yas et al. [253] studied the time history of the displacement and stress components of FG cylindrical shells subjected to dynamic loading using a layer-wise FE model. Nguyen-Xuan et al. [254, 255] expanded the ES-FEM and the NS-FEM to perform bending, vibration, and buckling analyses of FG plates. Cinefra et al. [256] presented a shell finite element model based on the CUF to analyze the bending behavior of FG plates and shells. Taghvaeipour et al. [257] conducted bending and modal analyses of FG hollow cylinders using a novel cylindrical element formulation. Natarajan and Manickam [258] used a QUAD-8 shear flexible element to study the bending and free flexural vibration behavior of sandwich FG plates. Kar and Panda [259] developed a Q9 quadrilateral shell element to analyze the natural frequencies of FG panels. Similar to Ferreira's [260], Pandey and Pradyumna [261, 262] developed a Q9-C^0 isoparametric HSDT layerwise model, However, they employed the Taylor series with higher-order terms in the core to describe the in-plane displacement field, analyzing the static and dynamic characteristics of laminated and sandwich plates. Later, they applied this theory [263, 264] to investigate the bending and vibration behavior of FG sandwich plates and shells subjected to thermal shock.

Kar and Panda [265] studied the natural frequency of FG spherical panels under the influence of thermal loading using a Q9-C^1 isoparametric element with 9 DOF. Nasirmanesh and Mohammadi [266] used Q8 shell elements to perform an eigenvalue buckling analysis of cracked FG cylindrical shells. Mehar and Panda [267] employed the FEM to assess the temperature-dependent vibrational response of FG-CNTs sandwich panels. Thom et al. [268] presented an FE model based on TSDT to study the buckling and bending of 2D-FG plates. Dash et al. [269] analyzed the natural frequency of FG sandwich panels via HSDT-FE formulation. Dash et al. [270] examined the bending behavior and flexural strength of FG sandwich panels. Pham et al. [271-277] developed an edge-based smoothed finite element model, "ES-MITC3," for serval mechanical analyses of FG structures. Pandey et al. [264, 278] carried out the bending and dynamic analyses of FG sandwich plates and skew panels. Belarbi et al. [237-239] developed a Q8-C^0 isoparametric model based on layerwise theory to explore FG plates. Karakoti et al. [279] investigated the impact of blast loading on the nonlinear transient response of porous FG sandwich panels, considering the temperature-dependent effect using a Q8 element based on FSDT. Sahoo et al. [280] carried out a vibration analysis of FG sandwich shells subjected to thermal loadings using Q9 shell element with 9 DOF, grounded in HSDT. Vinh et al. [281] explored the bending and buckling behavior of porous 2D-FG plates via A new mixed Q4 quadrilateral element. Nguyen et al. [282] conducted a bending analysis of 2D-FG sandwich plates resting on an elastic foundation in thermal environments, using an FE model based on Shi's HSDT. Later, Nguyen [283] expanded this model to examine the natural frequencies of porous 3D-FG sandwich plates. Benounas et al. [284, 285] investigated the static and free vibration behavior of FG plates with power-law, exponential, and sigmoid material property distributions. Jiammeepreecha et al. [286] examined the free vibration characteristics of FG spherical and elliptical shells subjected to nonlinear temperature effects. Lakhdar et al. [287, 288] analyzed the bending, free vibration, and thermal buckling of bi-directional FG single and sandwich shells via the TSDT-FE model. Belarbi et al. [289, 290] developed a Q8-C^0 isoparametric FE model based on the improved first-order shear deformation theory (IFSDT) to analyze the bending and free vibration of FG porous plates and nanoplates. Later, they [291] extended the model to analyze the fundamental frequencies of FG doubly curved shallow shells.

1.10 Conclusion

This chapter presents an overview of FGMs, tracing their historical development from their inception by Japanese researchers aimed to solve delamination issues in composite materials for space projects. Unlike traditional composites, FGMs have unique characteristics that are explored in detail. The chapter highlights the evolution of FGMs from their initial applications as thermal barriers to their diverse uses across various fields, including aerospace, automotive, biomedical implants, civil engineering, and energy systems. FGMs can be utilized as either thin coatings or bulk materials, depending on the application. Additionally, the chapter discusses the fabrication methods for both thin coatings and bulk FGMs, as well as the micromechanical models and material gradation laws used to describe their effective properties.

Subsequently, this chapter introduces the most commonly used theories for modeling and analyzing FG plates and shells. The CPT is the simplest, but it overlooks transverse shear deformation, making it applicable only to thin structures. The FSDT improves on this by considering constant transverse shear deformation across the thickness but requires a shear correction factor to accurately model the parabolic nature of transverse shear stresses. HSDTs further refine the modeling process by expanding the in-plane displacement field, allowing for a more precise capture of thickness variations. These theories often introduce additional terms in the displacement field to account for the non-linear distribution of shear strains across the thickness.

This chapter presents a comprehensive review of existing literature on the static and free vibration analysis of FG plates and shells. It highlights the dominance of analytical methods in the field, noting that studies employing the FEM are comparatively limited. Moreover, the research on FG shells remains relatively scarce, with most available investigations predominantly relying on analytical formulations rather than numerical or computational techniques.

This thesis seeks to fill this gap by exploring the static and vibrational behavior of single-layer FG plates and shells. To achieve this, it will employ a straightforward yet effective FE model based on the IFSDT. By leveraging this model, the research aims to provide deeper insights into the mechanical performance of FG structures, thereby contributing to the advancement of numerical techniques in this field.

In the next chapter, theoretical and FE formulations are proposed for a novel model, named SQ8-IFSDT, aimed at analyzing the bending and free vibration behavior of functionally graded doubly curved shallow shells (FG DCSSs).

Chapter 02

Theoretical and finite element formulation

Chapter 02

Theoretical and finite element formulation

2.1 Introduction

The majority of the literature studies have relied on analytical models to investigate the behavior of FG plates and shells. However, these analytical methods were typically restricted to simple geometries, specific types of material gradation, particular loading conditions, and predefined boundary types. As a result, numerical methods have become the preferred approach for analyzing the complex behavior of FG structures. Among these, the FEM is widely favored due to its flexibility in handling complex loading conditions, arbitrary material property gradations, variable boundary conditions, and its overall computational efficiency.

In this chapter, a novel 2D FE model based on an improved FSDT is developed. The present element, named SQ8-IFSDT, is a C^0 eight-node isoparametric quadrilateral element, with five degrees of freedom per node. This element is specifically designed to analyze the bending and free vibration in functionally graded doubly curved shallow shells (FG DCSSs). The material properties are assumed to vary continuously through the thickness, following a power-law distribution. To overcome the limitations of traditional FSDT in accurately representing shear stresses, a function $g(z)$ has been introduced, replacing the conventional shear correction factor k_s. This modification allows for a parabolic distribution of shear stresses, and satisfies the traction-free conditions at the top and bottom surfaces of the shell. The Hamiltonian principle is employed to derive the equations of motion and to formulate the stiffness, force vector, and mass matrices for the SQ8-IFSDT element, ensuring precise and efficient analysis of these complex structures.

2.2 Geometrical configuration

A doubly curved shallow shell made of FGM, defined by the coordinates (x, y, z), is considered, as depicted in **Figure 2.1**. The shell is a composite of ceramic and metal components and has curved dimensions, a and b, in the x and y directions, respectively. The radii of curvature of the middle surface in the x and y directions are denoted as R_x and R_y.

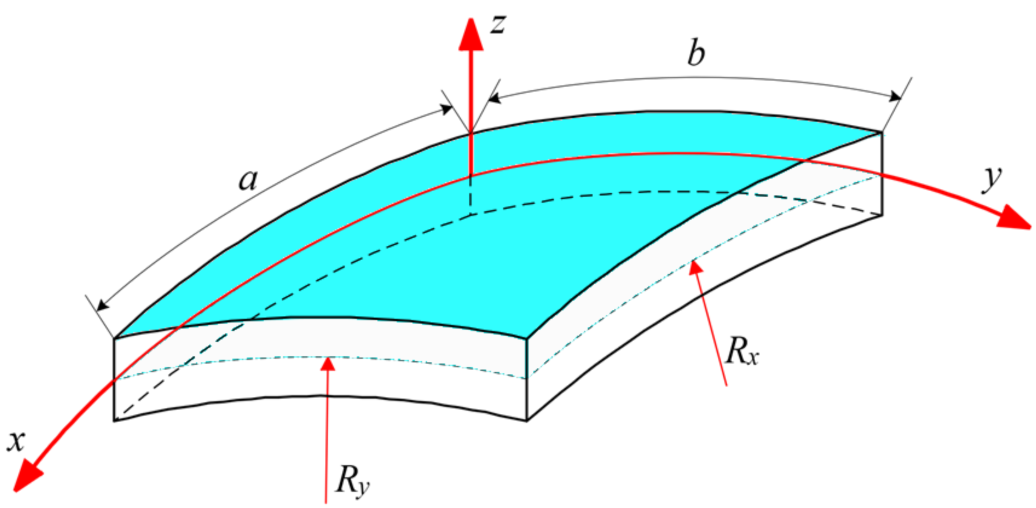

Figure 2.1 The geometry of FG DCSS.

Figure 2.2 illustrates various types of shell structures that can be achieved by modifying the curvatures as follows:

- Flat plate (FL plate): $R_x = \infty$ and $R_y = \infty$.
- Cylindrical shell (CY shell): $R_x = \infty$ and $R_y = R$.
- Spherical shell (SP shell): $R_x = R$ and $R_y = R$.
- Hyperbolic parabolic shell (HYP shell): $R_x = -R$ and $R_y = R$.
- Elliptical paraboloid shell (ELP shell): $R_x = 1.5R$ and $R_y = R$.

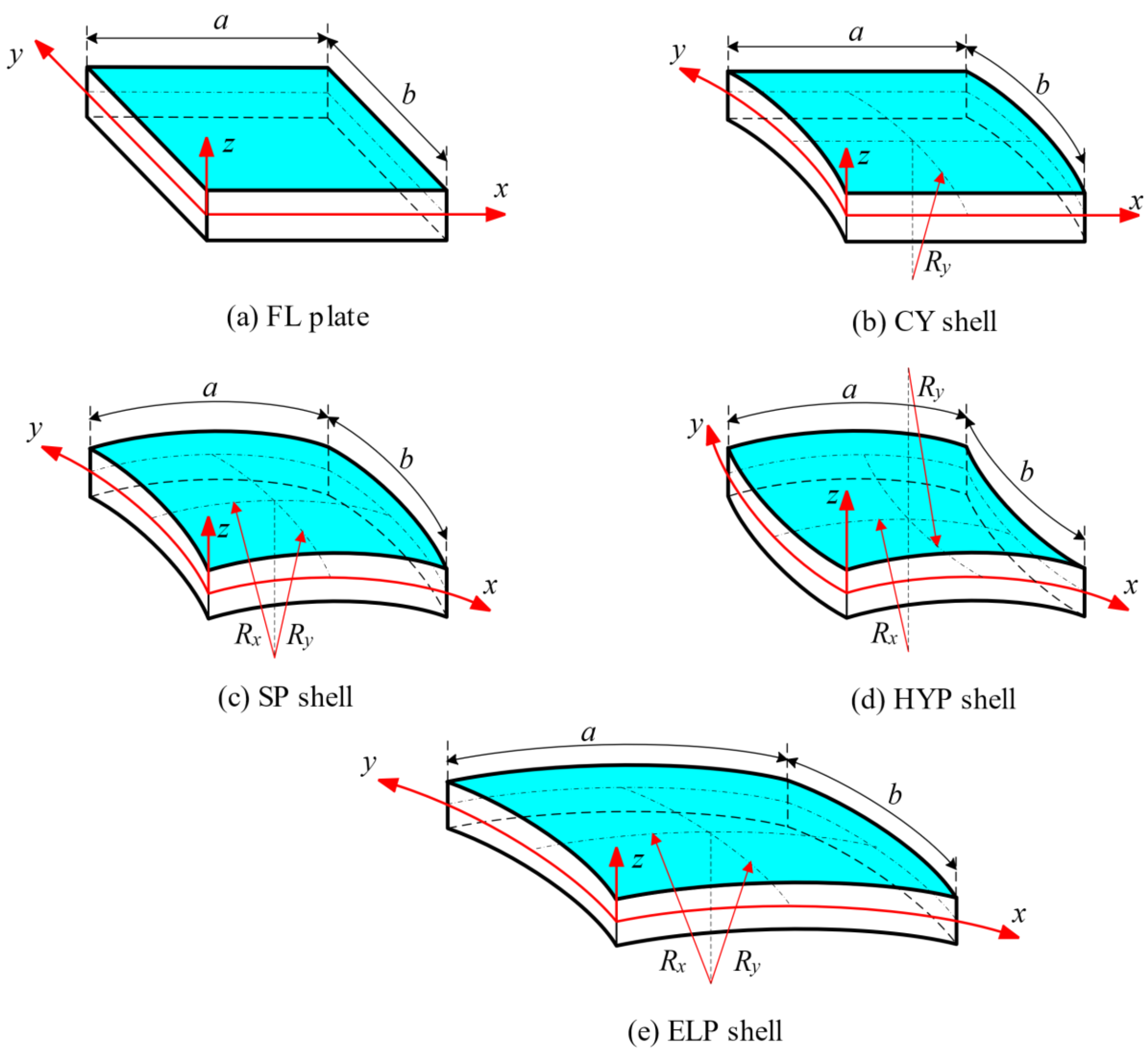

Figure 2.2 Types of FG DCSS.

2.3 Material properties

The volume fraction of the FG DCS changes along the thickness direction according to a power law distribution, expressed as [292]:

$$V_c(z) = \left(\frac{1}{2} + \frac{z}{h}\right)^k \tag{2.1}$$

Here, $V_c(z)$ represents the volume fraction of the ceramic phase, while the metal phase volume fraction V_m is given by $V_m = 1 - V_c$. The power-law index (k) controls the gradation of material properties across the thickness. When $k = 0$, the shell is purely ceramic, whereas as k approaches ∞ the shell becomes entirely metallic. The FGM shell exhibits a continuous variation of material composition through its thickness from z = -h/2 to z = +h/2, blending ceramic and metal components. To compute the effective material properties, the rule of mixtures is employed as follows [293]:

$$P(z) = P_m + (P_c - P_m)V_c(z) \tag{2.2}$$

where $P(z)$ is the effective property, P_m and P_c represent the mechanical properties of the metal and ceramic, respectively.

2.4 Kinematics of the present theory

2.4.1 Displacement field

The displacement field for the FG DCS is formulated based on the FSDT as follows [196]:

$$\begin{aligned} u(x,y,z,t) &= \left(1+\frac{z}{R_x}\right)u_0(x,y,t) + z\phi_x(x,y,t) \\ v(x,y,z,t) &= \left(1+\frac{z}{R_y}\right)v_0(x,y,t) + z\phi_y(x,y,t) \\ w(x,y,z,t) &= w_0(x,y,t) \end{aligned} \tag{2.3}$$

- u_0, v_0, and w_0 are the displacements of the mid-surface in the x-, y-, and z-directions, respectively.
- ϕ_x and ϕ_y represent the rotations of the normal to the mid-surface about the x- and y-axes, respectively.

2.4.2 Strain-displacement relationships

The strain components of FG DCSSs are deduced from the displacement field to:

$$\begin{aligned} \varepsilon_x &= \frac{\partial u_0}{\partial x} + \frac{w_0}{R_x} + z\frac{\partial \phi_x}{\partial x}, \\ \varepsilon_y &= \frac{\partial v_0}{\partial y} + \frac{w_0}{R_y} + z\frac{\partial \phi_y}{\partial y}, \\ \gamma_{xy} &= \frac{\partial u_0}{\partial y} + \frac{\partial v_0}{\partial x} + z\left(\frac{\partial \phi_x}{\partial y} + \frac{\partial \phi_y}{\partial x}\right), \\ \gamma_{xz} &= \frac{\partial w_0}{\partial x} - \frac{u_0}{R_x} + \phi_x, \\ \gamma_{yz} &= \frac{\partial w_0}{\partial y} - \frac{v_0}{R_y} + \phi_y \end{aligned} \tag{2.4}$$

In the short form:

$$\begin{Bmatrix}\varepsilon_x\\ \varepsilon_y\\ \gamma_{xy}\end{Bmatrix}=\begin{Bmatrix}\varepsilon_x^0\\ \varepsilon_y^0\\ \gamma_{xy}^0\end{Bmatrix}+z\begin{Bmatrix}\varepsilon_x^1\\ \varepsilon_y^1\\ \gamma_{xy}^1\end{Bmatrix};\qquad \begin{Bmatrix}\gamma_{xz}\\ \gamma_{yz}\end{Bmatrix}=\begin{Bmatrix}\gamma_{xz}^0\\ \gamma_{yz}^0\end{Bmatrix} \tag{2.5}$$

In which:

$$\begin{Bmatrix}\varepsilon_x^0\\ \varepsilon_y^0\\ \gamma_{xy}^0\end{Bmatrix}=\begin{Bmatrix}\dfrac{\partial u_0}{\partial x}+\dfrac{w_0}{R_x}\\ \dfrac{\partial v_0}{\partial y}+\dfrac{w_0}{R_y}\\ \dfrac{\partial u_0}{\partial y}+\dfrac{\partial v_0}{\partial x}\end{Bmatrix};\qquad \begin{Bmatrix}\varepsilon_x^1\\ \varepsilon_y^1\\ \gamma_{xy}^1\end{Bmatrix}=\begin{Bmatrix}\dfrac{\partial \phi_x}{\partial x}\\ \dfrac{\partial \phi_y}{\partial y}\\ \dfrac{\partial \phi_x}{\partial y}+\dfrac{\partial \phi_y}{\partial x}\end{Bmatrix}; \tag{2.6}$$

$$\begin{Bmatrix}\gamma_{xz}^0\\ \gamma_{yz}^0\end{Bmatrix}=\begin{Bmatrix}\dfrac{\partial w_0}{\partial x}-\dfrac{u_0}{R_x}+\phi_x\\ \dfrac{\partial w_0}{\partial y}-\dfrac{v_0}{R_y}+\phi_y\end{Bmatrix}$$

2.4.3 Constitutive relations

Neglecting the influence of transverse normal stress σ_z, the relation between stresses and strains can be written as:

$$\begin{Bmatrix}\sigma_{xx}\\ \sigma_{yy}\\ \tau_{xy}\end{Bmatrix}=\begin{bmatrix}\Lambda_{11} & \Lambda_{12} & 0\\ \Lambda_{21} & \Lambda_{22} & 0\\ 0 & 0 & \Lambda_{66}\end{bmatrix}\begin{Bmatrix}\varepsilon_{xx}\\ \varepsilon_{yy}\\ \gamma_{xy}\end{Bmatrix} \tag{2.7}$$

$$\begin{Bmatrix}\tau_{yz}\\ \tau_{xz}\end{Bmatrix}=\begin{bmatrix}\Lambda_{44} & 0\\ 0 & \Lambda_{55}\end{bmatrix}\begin{Bmatrix}\gamma_{yz}\\ \gamma_{xz}\end{Bmatrix} \tag{2.8}$$

where

$$\Lambda_{11}=\Lambda_{22}=\frac{E(z)}{1-\nu^2(z)},\quad \Lambda_{12}=\Lambda_{21}=\frac{\nu(z)E(z)}{1-\nu^2(z)},\quad \Lambda_{44}=\Lambda_{55}=\Lambda_{66}=\frac{E(z)}{2[1+\nu(z)]} \tag{2.9}$$

In many structural engineering analyses, the FSDT is widely applied, often incorporating a shear correction factor, typically $k_s = 5/6$. However, this traditional approach may fail to represent accurately the true distribution of transverse shear stresses through the shell's thickness [281]. To overcome this limitation, a novel enhanced approach is proposed [294, 295], which replaces the constant shear correction factor k_s with a function $g(z)$, defined as follows:

$$g(z) = \frac{5}{4} - \frac{5z^2}{h^2} \tag{2.10}$$

The proposed shear correction function $g(z)$ follows these conditions:

$$\int_{-\frac{h}{2}}^{\frac{h}{2}} g(z)dz = \frac{5h}{6}$$
$$g\left(-\frac{h}{2}\right) = g\left(\frac{h}{2}\right) = 0 \tag{2.11}$$

As a result, the equation (2.18) is modified to:

$$\begin{Bmatrix} \tau_{yz} \\ \tau_{xz} \end{Bmatrix} = g(z) \begin{bmatrix} \Lambda_{44} & 0 \\ 0 & \Lambda_{55} \end{bmatrix} \begin{Bmatrix} \gamma_{yz} \\ \gamma_{xz} \end{Bmatrix} \tag{2.12}$$

Eq. (2.13) incorporates a parabolic distribution of transverse shear stresses to more accurately capture the stress behavior at the shell's surfaces. This modification ensures that the free boundary conditions are satisfied on both the upper and lower surfaces without relying on the traditional shear correction factor used in FSDT. Additionally, the proposed approach provides a more realistic distribution and precise calculation of transverse shear stresses across the entire shell thickness.

2.5 The equation of motion

In the presented work, Hamilton's principle is employed to derive the governing equation for the bending and free vibration analysis of FG DCSSs, which can be expressed as:

$$\delta\Pi = \int_{t_1}^{t_2} \delta(U + W - T)dt = 0 \tag{2.13}$$

Here t_1 and t_2 represent the initial and final times, respectively, while δU, δW, and δT denote the variations in the strain energy, the work performed by the external forces, and the kinetic energy, respectively.

The first variation of the strain energy is given by the following expression:

$$\delta U = \frac{1}{2}\int_V \left(\sigma_x \delta\varepsilon_x + \sigma_y \delta\varepsilon_y + \tau_{xy}\delta\gamma_{xy} + \tau_{xz}\delta\gamma_{xz} + \tau_{yz}\delta\gamma_{yz}\right)dV \tag{2.14}$$

$$\delta U = \frac{1}{2}\int_V \left(\sigma_x[\delta\varepsilon_x^0 + z\delta\varepsilon_x^1] + \sigma_y\left[\delta\varepsilon_y^0 + z\delta\varepsilon_y^1\right] + \tau_{xy}\left[\delta\gamma_{xy}^0 + z\delta\gamma_{xy}^1\right] + \tau_{xz}\left[\delta\gamma_{xz}^0 + \tau_{yz}\delta\gamma_{yz}^0\right]\right)dV \quad (2.15)$$

$$\delta U = \frac{1}{2}\int_A \left(N_x\delta\varepsilon_x^0 + N_y\delta\varepsilon_y^0 + N_{xy}\delta\gamma_{xy}^0 + M_x\delta\varepsilon_x^1 + M_y\delta\varepsilon_y^1 + M_{xy}\delta\gamma_{xy}^1 + Q_{xz}\delta\gamma_{xz}^0 + Q_{yz}\delta\gamma_{yz}^0\right)dA \quad (2.16)$$

N_i, M_i, and Q_i represent the axial force, bending moment, and shear force, respectively.

with

$$N = \begin{Bmatrix} N_x \\ N_y \\ N_{xy} \end{Bmatrix} = \int_{-h/2}^{h/2} \begin{Bmatrix} \sigma_x \\ \sigma_x \\ \tau_{xy} \end{Bmatrix} dz, \qquad M = \begin{Bmatrix} M_x \\ M_y \\ M_{xy} \end{Bmatrix} = \int_{-h/2}^{h/2} \begin{Bmatrix} \sigma_x \\ \sigma_x \\ \tau_{xy} \end{Bmatrix} zdz,$$
$$Q = \begin{Bmatrix} Q_{xz} \\ Q_{yz} \end{Bmatrix} = \int_{-\frac{h}{2}}^{\frac{h}{2}} \begin{Bmatrix} \tau_{xz} \\ \tau_{yz} \end{Bmatrix} dz \quad (2.17)$$

By substituting Eqs. (2.7) and (2.8) into Eq. (2.17) and integrating through the thickness of the shell, the constitutive relations for forces and moments in terms of strains can be expressed as:

$$\begin{Bmatrix} N_x \\ N_y \\ N_{xy} \\ M_x \\ M_y \\ M_{xy} \end{Bmatrix} = \begin{bmatrix} A_{11} & A_{12} & 0 & B_{11} & B_{12} & 0 \\ A_{12} & A_{22} & 0 & B_{12} & B_{22} & 0 \\ 0 & 0 & A_{66} & 0 & 0 & B_{66} \\ B_{11} & B_{12} & 0 & D_{11} & D_{12} & 0 \\ B_{12} & B_{22} & 0 & D_{12} & D_{22} & 0 \\ 0 & 0 & B_{66} & 0 & 0 & D_{66} \end{bmatrix} \begin{Bmatrix} \varepsilon_x^0 \\ \varepsilon_y^0 \\ \gamma_{xy}^0 \\ \varepsilon_x^1 \\ \varepsilon_y^1 \\ \gamma_{xy}^1 \end{Bmatrix} \quad (2.18)$$

$$\begin{bmatrix} Q_{xz} \\ Q_{yz} \end{bmatrix} = \begin{bmatrix} S_{55} & 0 \\ 0 & S_{44} \end{bmatrix} \begin{bmatrix} \gamma_{xz}^0 \\ \gamma_{yz}^0 \end{bmatrix} \quad (2.19)$$

where

$$\left(A_{ij},\ B_{ij},\ D_{ij}\right) = \int_{-\frac{h}{2}}^{\frac{h}{2}} \Lambda_{ij}(z)(1, z,\ z^2)\, dz \quad (i,j = 1,2,6) \quad (2.20)$$

$$\left(S_{ij}\right) = \int_{-\frac{h}{2}}^{\frac{h}{2}} g(z)\Lambda_{ij}(z)dz \qquad (i,j = 4,5) \quad (2.21)$$

The stiffness coefficient, as described by Reddy [296], can be expressed as:

$$A_{11} = A_{22} = \int_{-h/2}^{h/2} \Lambda_{11} dz = \int_{-h/2}^{h/2} \frac{E(z)}{1-\nu^2(z)} dz = \frac{E_c h^2}{1-\nu^2(z)} \left(\frac{m+k}{k+1}\right), \tag{2.22a}$$

$$A_{12} = A_{21} = \int_{-h/2}^{h/2} \Lambda_{12} dz = \int_{-h/2}^{h/2} \frac{\nu(z)E(z)}{1-\nu^2(z)} dz = \nu(z) A_{11}, \tag{2.22b}$$

$$A_{66} = \int_{-h/2}^{h/2} \Lambda_{66} dz = \int_{-h/2}^{h/2} \frac{E(z)}{2(1+\nu(z))} dz = \frac{1-\nu(z)}{2} A_{11}, \tag{2.22c}$$

$$B_{11} = B_{22} = \int_{-h/2}^{h/2} z\Lambda_{11} dz = \int_{-h/2}^{h/2} \frac{zE(z)}{1-\nu^2(z)} dz = \frac{E_c h^2}{1-\nu^2(z)} \; \frac{(m-1)+k}{2(k+1)(k+2)}, \tag{2.22d}$$

$$B_{12} = B_{21} = \nu(z) B_{11}, \tag{2.22e}$$

$$B_{66} = \frac{1-\nu(z)}{2} B_{11}, \tag{2.22f}$$

$$D_{11} = D_{22} = \int_{-h/2}^{h/2} z^2 \Lambda_{11} dz = \int_{-h/2}^{h/2} \frac{z^2 E(z)}{1-\nu^2(z)} dz = \frac{E_c h^3}{1-\nu^2(z)} \left(\frac{(m-k)(2+k+k^2)}{4(k+1)(k+2)(k+3)} + \frac{1}{12}\right), \tag{2.22g}$$

$$D_{12} = D_{21} = \nu(z) D_{11}, \tag{2.22h}$$

$$D_{66} = \frac{1-\nu(z)}{2} D_{11}, \tag{2.22i}$$

$$S_{44} = S_{55} = \int_{-h/2}^{h/2} g(z)\Lambda_{44} dz = \int_{-h/2}^{h/2} \frac{g(z)E(z)}{2(1+\nu(z))} dz = \frac{5h}{6} \frac{E_c bh}{2(1+\nu(z))} \frac{m+k}{1+k} \tag{2.22j}$$

Here, $m = E_m/E_c$ represents the ratio of Young's modulus for the two components of the FG DCSS.

By substituting Eq. (2.18) and Eq. (2.19) into Eq. (2.16), the variation of the strain energy can be written as:

$$
\begin{aligned}
\delta U = \frac{1}{2}\int_A \, [&\varepsilon_x^0 A_{11}\delta\varepsilon_x^0 + \varepsilon_y^0 A_{12}\delta\varepsilon_x^0 + \varepsilon_x^1 B_{11}\delta\varepsilon_x^0 + \varepsilon_y^1 B_{12}\delta\varepsilon_x^0 + \varepsilon_x^0 A_{12}\delta\varepsilon_y^0 \\
&+ \varepsilon_y^0 A_{22}\delta\varepsilon_y^0 + \varepsilon_x^1 B_{12}\delta\varepsilon_y^0 + \varepsilon_y^1 B_{22}\delta\varepsilon_y^0 + \gamma_{xy}^0 A_{66}\delta\gamma_{xy}^0 + \gamma_{xy}^1 B_{66}\delta\gamma_{xy}^0 \\
&+ \varepsilon_x^0 B_{11}\delta\varepsilon_x^1 + \varepsilon_y^0 B_{12}\delta\varepsilon_x^1 + \varepsilon_x^1 D_{11}\delta\varepsilon_x^1 + \varepsilon_y^1 D_{12}\delta\varepsilon_x^1 + \varepsilon_x^0 B_{12}\delta\varepsilon_y^1 \\
&+ \varepsilon_y^0 B_{22}\delta\varepsilon_y^1 + \varepsilon_x^1 D_{12}\delta\varepsilon_y^1 + \varepsilon_y^1 D_{22}\delta\varepsilon_y^1 + \gamma_{xy}^0 B_{66}\delta\gamma_{xy}^1 + \gamma_{xy}^1 D_{66}\delta\gamma_{xy}^1 \\
&+ \gamma_{xz}^0 S_{55}\delta\gamma_{xz}^0 + \gamma_{yz}^0 S_{44}\delta\gamma_{yz}^0 \big) dA
\end{aligned}
\tag{2.23}
$$

In short

$$
\begin{aligned}
\delta U = \frac{1}{2}\int_A \, [&(\varepsilon^0)^T[A]\delta\varepsilon^0 + (\varepsilon^0)^T[B]\delta\varepsilon^1 + (\varepsilon^1)^T[B]\delta\varepsilon^0 + (\varepsilon^1)^T[D]\delta\varepsilon^1 \\
&+ (\gamma^0)^T[S]\delta\gamma^0]dA
\end{aligned}
\tag{2.24}
$$

The variation of the external work due to the distributed loading force *q* acting on an FG DCSS is given by:

$$
\delta W = -\frac{1}{2}\int_A q\delta w dA \tag{2.25}
$$

A transverse distributed load $q = [0 \quad 0 \quad q \quad 0 \quad 0]^T$ is assumed, with no additional loads applied.

The computation of the variation of kinetic energy for an FG DCSS follows this formula:

$$
\delta T = \frac{1}{2}\int_V \rho(z)\,(\dot{u}\delta\dot{u} + \dot{v}\delta\dot{v} + \dot{w}\delta\dot{w})dV \tag{2.26}
$$

where $\dot{u}$, $\dot{v}$, and $\dot{w}$ denote the velocities in the *x*, *y*, and *z* directions, respectively, while *ρ(z)* represents the effective density of the FG DCSS at position *z*.

The governing equations of motion for the FG DCSS are derived from Eq. (2.13) and can be expressed as the following:

$$
\begin{aligned}
\delta u&: \frac{\partial N_x}{\partial x} + \frac{\partial N_{xy}}{\partial y} + \frac{Q_x}{R_x} = I_0\ddot{u} + I_1\ddot{\varphi}_x \\
\delta v&: \frac{\partial N_y}{\partial y} + \frac{\partial N_{xy}}{\partial x} + \frac{Q_y}{R_y} = I_0\ddot{v} + I_1\ddot{\varphi}_y
\end{aligned}
\tag{2.27}
$$

$$\delta w: \frac{\partial Q_x}{\partial x} + \frac{\partial Q_y}{\partial y} - \frac{N_x}{R_x} - \frac{N_y}{R_y} = I_0 \ddot{w}$$

$$\delta \varphi_x: \frac{\partial M_x}{\partial x} + \frac{\partial M_{xy}}{\partial y} - Q_x = I_1 \ddot{u} + I_2 \ddot{\phi}_x$$

$$\delta \varphi_y: \frac{\partial M_y}{\partial y} + \frac{\partial M_{xy}}{\partial x} - Q_y = I_1 \ddot{v} + I_2 \ddot{\phi}_y$$

The inertia terms are presented as:

$$I_i = \int_{-h/2}^{h/2} P(z)\, z^i dz = \int_{-h/2}^{h/2} (\rho_m + (\rho_c - \rho_m) V(z))\, z^i dz, \qquad i = 0,1,2 \tag{2.28}$$

Or

$$\begin{gathered} I_0 = \frac{(\rho_c - \rho_m)h}{(k+1)} + \rho_m h; \qquad I_1 = \frac{(\rho_c - \rho_m)h^2}{2(k+1)(k+2)}; \\ I_2 = \frac{(\rho_c - \rho_m)h^3(2 + k + k^2)}{4(k+1)(k+2)(k+3)} + \rho_m \frac{h^3}{12} \end{gathered} \tag{2.29}$$

2.6 Finite element formulation

A 2D C^0 eight-node isoparametric quadrilateral element, featuring five degrees of freedom per node (DOF), has been developed for the static and free vibration analysis of FG DCSSs (as illustrated in **Figure 2.3**). The formulation of the presented element is based on the improved first-order shear deformation theory (IFSDT).

Figure 2.3 represents the natural coordinate system (ξ, η), while the physical coordinates of a point in the element are defined by $x = a$, $x = b$, $y = c$, $y = d$.

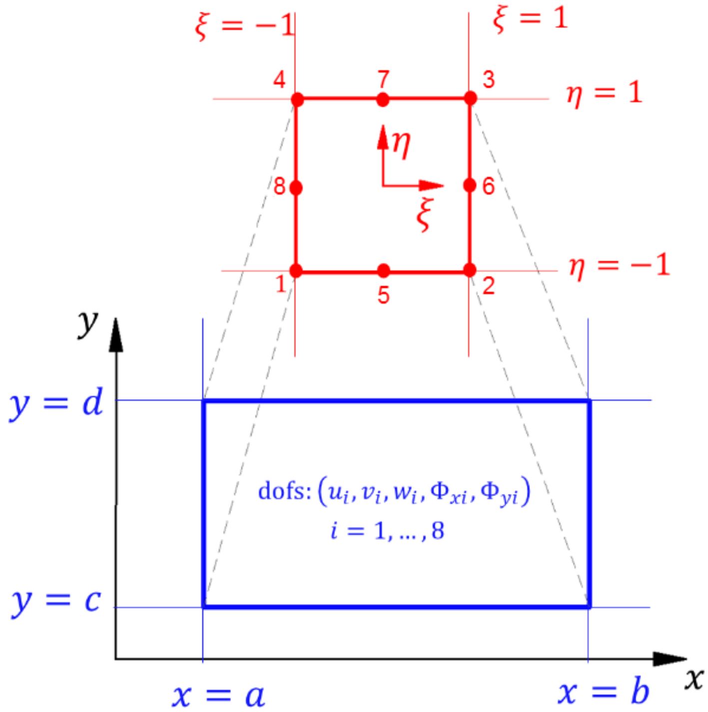

Figure 2.3 The geometry and corresponding DOFs of the developed element.

After transformation, the elements become isoparametric by ensuring that the number of nodes used in the geometric interpolation functions matches the number of nodes used in the displacement interpolation functions. The shape functions N_i for 8-node serendipity elements are given by:

$$N_i = \frac{1}{4}(1 + \xi\xi_i)(1 + \eta\eta_i)(\xi\xi_i + \eta\eta_i - 1), \qquad i = 1, 2, 3, 4 \tag{2.30a}$$

$$N_i = \frac{1}{2}(1 - \xi^2)(1 + \eta\eta_i), \qquad i = 5, 7 \tag{2.30b}$$

$$N_i = \frac{1}{2}(1 - \eta^2)(1 + \xi\xi_i), \qquad i = 6, 8 \tag{2.30c}$$

Or

$$
\begin{aligned}
&N_1(\xi,\eta) = -\frac{1}{4}(1-\xi)(1-\eta)(1+\xi+\eta), \quad N_2(\xi,\eta) = -\frac{1}{4}(1+\xi)(1-\eta)(1-\xi+\eta) \\
&N_3(\xi,\eta) = -\frac{1}{4}(1+\xi)(1+\eta)(1-\xi-\eta), \quad N_4(\xi,\eta) = -\frac{1}{4}(1-\xi)(1+\eta)(1+\xi-\eta) \\
&N_5(\xi,\eta) = \frac{1}{2}(1-\xi^2)(1-\eta), \qquad N_6(\xi,\eta) = \frac{1}{2}(1+\xi)(1-\eta^2) \\
&N_7(\xi,\eta) = \frac{1}{2}(1-\xi^2)(1+\eta), \qquad N_8(\xi,\eta) = \frac{1}{2}(1-\xi)(1-\eta^2)
\end{aligned}
\tag{2.31}
$$

The displacement parameters are given as:

$$
\begin{aligned}
&u = \sum_{i=1}^{n} N_i(\xi,\eta)\,\tilde{u}_i, \qquad v = \sum_{i=1}^{n} N_i(\xi,\eta)\,\tilde{v}_i, \qquad w = \sum_{i=1}^{n} N_i(\xi,\eta)\,\widetilde{w}_i, \\
&\phi_x = \sum_{i=1}^{n} N_i(\xi,\eta)\,\tilde{\phi}_{x,i}, \qquad \phi_y = \sum_{i=1}^{n} N_i(\xi,\eta)\,\tilde{\phi}_{y,i}
\end{aligned}
\tag{2.32}
$$

Where

$$
\begin{aligned}
&\begin{Bmatrix} N_{i,\xi} \\ N_{i,\eta} \end{Bmatrix} = \begin{bmatrix} J_{11} & J_{12} \\ J_{21} & J_{22} \end{bmatrix} \begin{Bmatrix} N_{i,x} \\ N_{i,y} \end{Bmatrix} = J \begin{Bmatrix} N_{i,x} \\ N_{i,y} \end{Bmatrix} \\
&\begin{Bmatrix} N_{i,x} \\ N_{i,y} \end{Bmatrix} = J^{-1} \begin{Bmatrix} N_{i,\xi} \\ N_{i,\eta} \end{Bmatrix} = \begin{bmatrix} J_{11}^* & J_{12}^* \\ J_{21}^* & J_{22}^* \end{bmatrix} \begin{Bmatrix} N_{i,\xi} \\ N_{i,\eta} \end{Bmatrix}
\end{aligned}
\tag{2.33}
$$

J is the Jacobian matrix used for the transformation from natural to Cartesian coordinates, and it contains the following elements:

$$
\begin{aligned}
&J_{11} = \sum_{i=1}^{n} N_{i,\xi}\,\tilde{u}_i, \qquad J_{12} = \sum_{i=1}^{n} N_{i,\xi}\,\tilde{v}_i, \\
&J_{21} = \sum_{i=1}^{n} N_{i,\eta}\,\tilde{u}_i, \qquad J_{22} = \sum_{i=1}^{n} N_{i,\eta}\,\tilde{v}_i
\end{aligned}
\tag{2.34}
$$

Where n is the order of the finite element node, and J_{11}^*, J_{12}^*, J_{21}^*, J_{22}^* are the elements of the inverse Jacobian matrix. Based on the IFSDT assumptions, each node is assigned five degrees of freedom to account for the five unknown variables, as outlined below:

$$
\tilde{u} = \{u_1 \dots u_n\}^T, \qquad \tilde{v} = \{v_1 \dots v_n\}^T, \qquad \widetilde{w} = \{w_1 \dots w_n\}^T, \tag{2.35}
$$

$$\tilde{\phi}_x = \{\phi_{x,1} \dots \phi_{x,n}\}^T, \qquad \tilde{\phi}_y = \{\phi_{y,1} \dots \phi_{y,n}\}^T$$

Thus, Eq. (2.35) can be reformulated as:

$$\begin{Bmatrix} u \\ v \\ w \\ \phi_x \\ \phi_y \end{Bmatrix} = \begin{bmatrix} N & 0 & 0 & 0 & 0 \\ 0 & N & 0 & 0 & 0 \\ 0 & 0 & N & 0 & 0 \\ 0 & 0 & 0 & N & 0 \\ 0 & 0 & 0 & 0 & N \end{bmatrix} \begin{Bmatrix} \tilde{u} \\ \tilde{v} \\ \tilde{w} \\ \phi_x \\ \phi_y \end{Bmatrix} = [N]d^e \tag{2.36}$$

The strain-displacement matrices, including the membrane component $[B_m]$, bending component $[B_b]$, and shear component $[B_s]$, are derived using Eq. (2.4) with the FE approximation as follows:

$$\begin{aligned} \varepsilon^0 &= \left[B_m^{(e)}\right]\{d\}^e \\ \varepsilon^1 &= \left[B_b^{(e)}\right]\{d\}^e \\ \gamma^0 &= \left[B_s^{(e)}\right]\{d\}^e \end{aligned} \tag{2.37}$$

Where

$$\left[B_m^{(e)}\right] = \begin{bmatrix} \frac{\partial N}{\partial x} & 0 & \frac{1}{R_x}N & 0 & 0 \\ 0 & \frac{\partial N}{\partial y} & \frac{1}{R_y}N & 0 & 0 \\ \frac{\partial N}{\partial y} & \frac{\partial N}{\partial x} & 0 & 0 & 0 \end{bmatrix}, \qquad \left[B_b^{(e)}\right] = \begin{bmatrix} 0 & 0 & 0 & \frac{\partial N}{\partial x} & 0 \\ 0 & 0 & 0 & 0 & \frac{\partial N}{\partial y} \\ 0 & 0 & 0 & \frac{\partial N}{\partial y} & \frac{\partial N}{\partial x} \end{bmatrix},$$

$$\left[B_s^{(e)}\right] = \begin{bmatrix} -\frac{1}{R_x}N & 0 & \frac{\partial N}{\partial x} & N & 0 \\ 0 & -\frac{1}{R_y}N & \frac{\partial N}{\partial y} & 0 & N \end{bmatrix} \tag{2.38}$$

In this context, $\left[B_m^{(e)}\right]$ and $\left[B_b^{(e)}\right]$ are matrices of size 3×40, respectively, while $\left[B_s^{(e)}\right]$ is a matrix of size 2×40.

Now, the strain energy in Eq. (2.24) will become:

$$U = \frac{1}{2} d^{eT} \int_{A^e} (B_m^T[A]B_m + B_m^T[B]B_b + B_b^T[B]B_m + B_b^T[D]B_b + B_s^T[S]B_s) dA^e d^e \tag{2.39}$$

This results in the following stiffness components:

$$\begin{aligned} K_m^{(e)} &= \int_{A^e} B_m^T[A]B_m dA^e \\ K_{mb}^{(e)} &= \int_{A^e} B_m^T[B]B_b dA^e \\ K_{bm}^{(e)} &= \int_{A^e} B_b^T[B]B_m dA^e \\ K_b^{(e)} &= \int_{A^e} B_b^T[D]B_b dA^e \\ K_s^{(e)} &= \int_{A^e} B_s^T[S]B_s dA^e \end{aligned} \tag{2.40}$$

The element stiffness matrix is defined as the sum of all these components, given by:

$$[K]^e = K_m^{(e)} + K_{mb}^{(e)} + K_{bm}^{(e)} + K_b^{(e)} + K_s^{(e)} \tag{2.41}$$

To ensure an accurate numerical evaluation of the integrals, Gauss quadrature is applied. A 3×3 Gauss quadrature scheme is used for the membrane, bending, and bending–membrane coupling contributions. In contrast, a reduced 2×2 quadrature scheme is adopted for the shear terms as reduced integration to mitigate shear locking. After applying Gauss integration for computational purposes, the element stiffness matrix is defined as:

$$\begin{aligned} [K]^e = \int_{-1}^{1}\int_{-1}^{1} \Bigg(& \underbrace{[B_m][A][B_m]^T}_{\text{membrane}} + \underbrace{[B_b][B][B_m]^T}_{\text{coupling membrane-bending}} + \underbrace{[B_m][B][B_b]^T}_{\text{coupling bending-membrane}} \\ & + \underbrace{[B_b][D][B_b]^T}_{\text{bending}} + \underbrace{[B_s][S][B_s]^T}_{shear} \Bigg) |J| d\xi d\eta \end{aligned} \tag{2.42}$$

Here $|J|$ is the determinant of the Jacobian matrix, and $|J| d\xi d\eta = dxdy$ represents the transformation to the Cartesian coordinate system.

Following the integration and assembly processes, the static equilibrium equation for the analysis can be written as:

$$[K]^e \times \{d\}^e = \{f\}^e \tag{2.43}$$

Where $\{f\}^e$ is the element force vector, which represents the equivalent nodal forces induced by the applied distributed load q, which can be formulated as:

$$\{f\}^e = -\int_{-1}^{1}\int_{-1}^{1}[N_w]^T\, q\, |J| d\xi d\eta \tag{2.44}$$

with

$$[N_w] = [N_w^1 \quad N_w^2 \quad N_w^3 \quad N_w^4 \quad N_w^5 \quad N_w^6 \quad N_w^7 \quad N_w^8] \tag{2.45}$$

where

$$[N_w^i] = [0 \quad 0 \quad N_i \quad 0 \quad 0] \tag{2.46}$$

N_w^i: represents the shape function that defines how the external distributed load q is distributed and transferred to the i^{th} node of the element.

Following the assembly process, the global static equations of motion for the FG DCSS are derived as follows:

$$[K] \times \{d\} = \{f\} \tag{2.47}$$

The static equations of motion at equilibrium (2.47) are solved directly using a MATLAB script (MATLAB 2023b, The MathWorks, Inc.) developed by the authors. The detailed FEM procedure is shown in **Figure 2.4**.

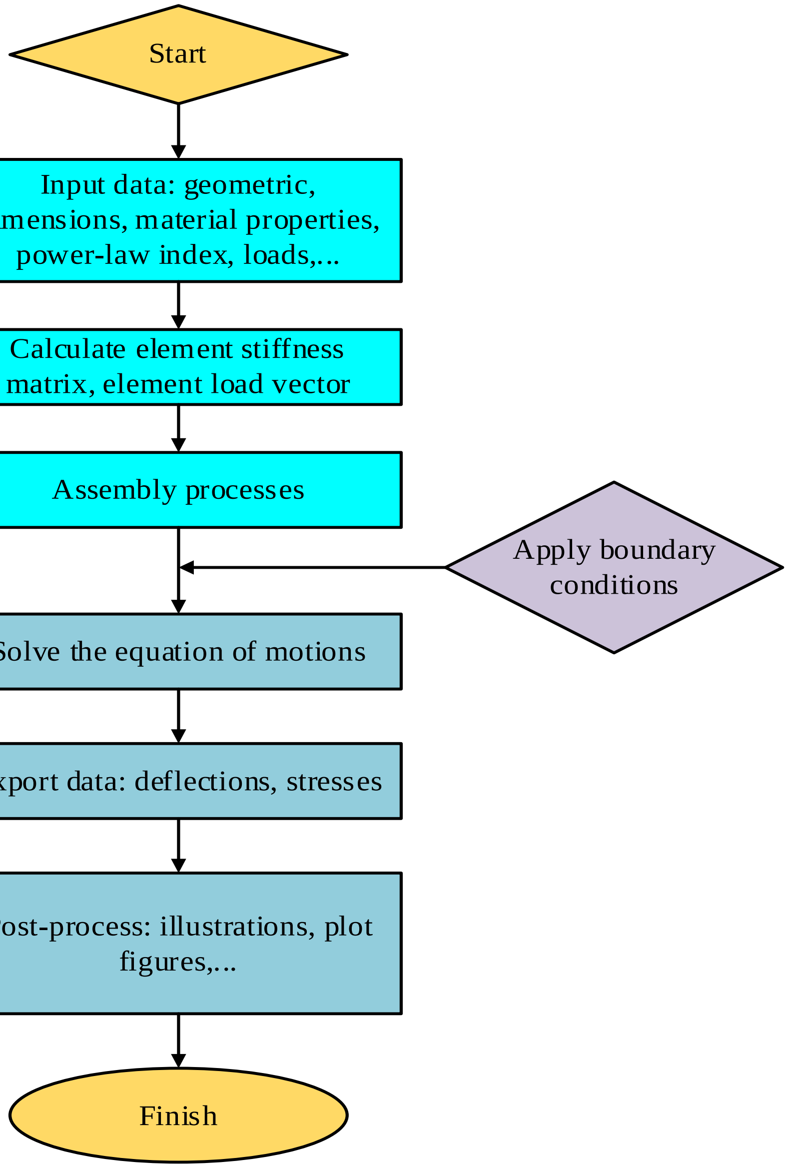

Figure 2.4 The flowchart illustrating the systematic FEM solution procedure.

Next, the motion equation for the free vibration of the FG DCSS is derived from Eq. (2.13) and expressed as the following dynamic equilibrium equation of the system:

$$[M]\{\ddot{d}\} + [K]\{d\} = 0 \tag{2.48}$$

The element mass matrix is calculated using the following expression:

$$[M]^e = \int_{-1}^{1}\int_{-1}^{1} ([N]^T[I_k][N])|J|d\xi d\eta \tag{2.49}$$

where

$$I_k = \begin{bmatrix} I_0 & 0 & 0 & I_1 & 0 \\ & I_0 & 0 & 0 & I_1 \\ & & I_0 & 0 & 0 \\ & sym & & I_2 & 0 \\ & & & & I_2 \end{bmatrix} \tag{2.50}$$

Once the stiffness and mass matrices for all elements are evaluated, the governing equations for the free vibration analysis of the FG DCSSs can be formulated as a generalized eigenvalue problem, expressed as:

$$[K]_{N\times N}\{\chi\}_{N\times 1} - \omega^2[M]_{N\times N}\{\chi\}_{N\times 1} = 0 \tag{2.51}$$

Here, ω represents the natural frequency, $[K]$ stands for the global stiffness matrix with dimensions $N\times N$, $[M]$ is the global mass matrix, also with dimensions $N\times N$, and $\{\chi\}$ is the $N\times 1$ vector that represents the mode shapes. In this context, N indicates the total number of degrees of freedom of the FG DCSS. The mode shape vector is expressed as:

$$\{\chi\}_{N\times 1} = \{d_1 \quad d_2 \quad d_3 \quad \dots \quad d_{n-1} \quad d_n\}^T \tag{2.52}$$

The eigenvector $\{\chi\}$ characterizes the complete set of mode shapes of the shell, capturing both out-of-plane and in-plane vibration behaviors. For in-plane modes, the transverse displacement component is negligible, allowing these modes to be easily distinguished from out-of-plane vibrations. To determine the natural frequencies and corresponding mode shapes, the system of equations must yield non-trivial solutions, which is achieved by setting the determinant of the governing matrix equation to zero, as expressed below:

$$det([K] - \omega^2[M]) = 0 \tag{2.53}$$

2.7 Conclusion

In this chapter, a new 2D C^0 eight-node isoparametric quadrilateral finite element model with five degrees of freedom has been developed, named SQ8-IFSDT. The Fe model is based on an improved first-order shear deformation theory. The model is specifically designed for the static and free vibration analysis of FG DCSSs.

The following chapter will focus on assessing the convergence and accuracy of the SQ8-IFSDT model in predicting the transverse displacement, normal stress, and shear stress distribution of FG DCSSs. It will include a convergence study and a comparison against established data from the literature. Furthermore, it will present new results that have never been published before, contributing novel insights into the bending and vibrational behavior of FG DCSSs.

Chapter 03

Bending analysis of FG DCSs:

Results and discussion

Chapter 03

Bending analysis of FG DCSs: Results and discussion

3.1 Introduction

This chapter presents comprehensive numerical results to validate the accuracy and efficiency of the proposed FE model, SQ8-IFSDT, in analyzing the static behavior of functionally graded doubly curved shallow shells (FG DCSSs). Five different shell geometries are investigated: flat plates (FL), cylindrical shells (CY), spherical shells (SP), hyperbolic paraboloid shells (HYP), and elliptical shells (ELP). A convergence study is performed, and the results are benchmarked against existing literature to ensure reliability. Additionally, a detailed parametric study is conducted to assess the influence of key parameters including the power-law index (k), side-to-thickness ratio (a/h), radius-to-thickness ratio (R/h), radius-to-length ratio (R/a), boundary conditions, and loading types on the transverse displacement as well as normal and shear stresses of FG DCSSs. **Table 3.1** summarizes the material properties used. **Table 3.2** and **Figure 3.1** outline the boundary conditions applied across all case studies.

For this study, the following relations for the dimensionless transverse displacement (DTD), normal and shear stresses are:

$$w^* = \frac{w}{h} \quad ; \quad \bar{w} = \left(\frac{w}{q_0}\right)\left(\frac{100E_c h^3}{a^4}\right) \quad ; \quad \bar{\sigma}_x = \frac{h}{q_0 a}\,\sigma_x\left(\frac{a}{2},\frac{b}{2},\frac{h}{2}\right) \quad ; \quad \bar{\sigma}_y = \frac{h}{q_0 a}\,\sigma_y\left(\frac{a}{2},\frac{b}{2},\frac{h}{3}\right) \tag{3.1}$$

$$\bar{\tau}_{xy} = \frac{h}{q_0 a}\, \tau_{xy}\left(0,0,-\frac{h}{3}\right) \quad ; \quad \bar{\tau}_{xz} = \frac{h}{q_0 a}\, \tau_{xz}\left(0,\frac{b}{2},0\right) \quad ; \quad \bar{\tau}_{yz} = \frac{h}{q_0 a}\, \tau_{xy}\left(\frac{a}{2},0,\frac{h}{6}\right)$$

The uniformly distributed load (UL) is given by:

$$q(x,y) = q \qquad (3.2)$$

The sinusoidally distributed load (SL) is given by:

$$q(x,y) = q\sin\left(\frac{\pi x}{a}\right)\sin\left(\frac{\pi y}{b}\right) \qquad (3.2)$$

Table 3.1 Material properties of FG DCSSs analyzed in this study.

Materials	**Properties**		
	$\boldsymbol{E\ (GPa)}$	$\boldsymbol{\nu}$	$\boldsymbol{\rho\ (kg/m^3)}$
Al	70	0.30	2707
Al_2O_3	380	0.3	3800
ZrO_2	151	0.3	3000

Table 3.2 The boundary conditions used in the present study.

Boundary conditions	**Abbreviations**	**Restrained edges**
Simply supported	SSSS	$v_0 = w_0 = \phi_y = 0$ at $x = 0$ and $x = a$ $u_0 = w_0 = \phi_x = 0$ at $y = 0$ and y = b
Clamped	CCCC	$u_0 = v_0 = w_0 = \phi_x = \phi_y = 0$ at $x = 0$ and $x = a$ and $y = 0$ and $y = b$
Clamped-Simply supported	CSCS	$u_0 = w_0 = \phi_x = 0$ at $y = 0$ and $y = b$ $u_0 = v_0 = w_0 = \phi_x = \phi_y = 0$ at $x = 0$ and $x = a$
Three edges Clamped and one Simply supported	CSCC	$u_0 = v_0 = w_0 = \phi_x = \phi_y = 0$ at $x = 0$ and x = a and $y = b$ $u_0 = w_0 = \phi_x = 0$ at $y = 0$
Two edges Clamped and two opposite edges Free	CFCF	$u_0 = v_0 = w_0 = \phi_x = \phi_y = 0$ at $x = 0$ and $x = a$

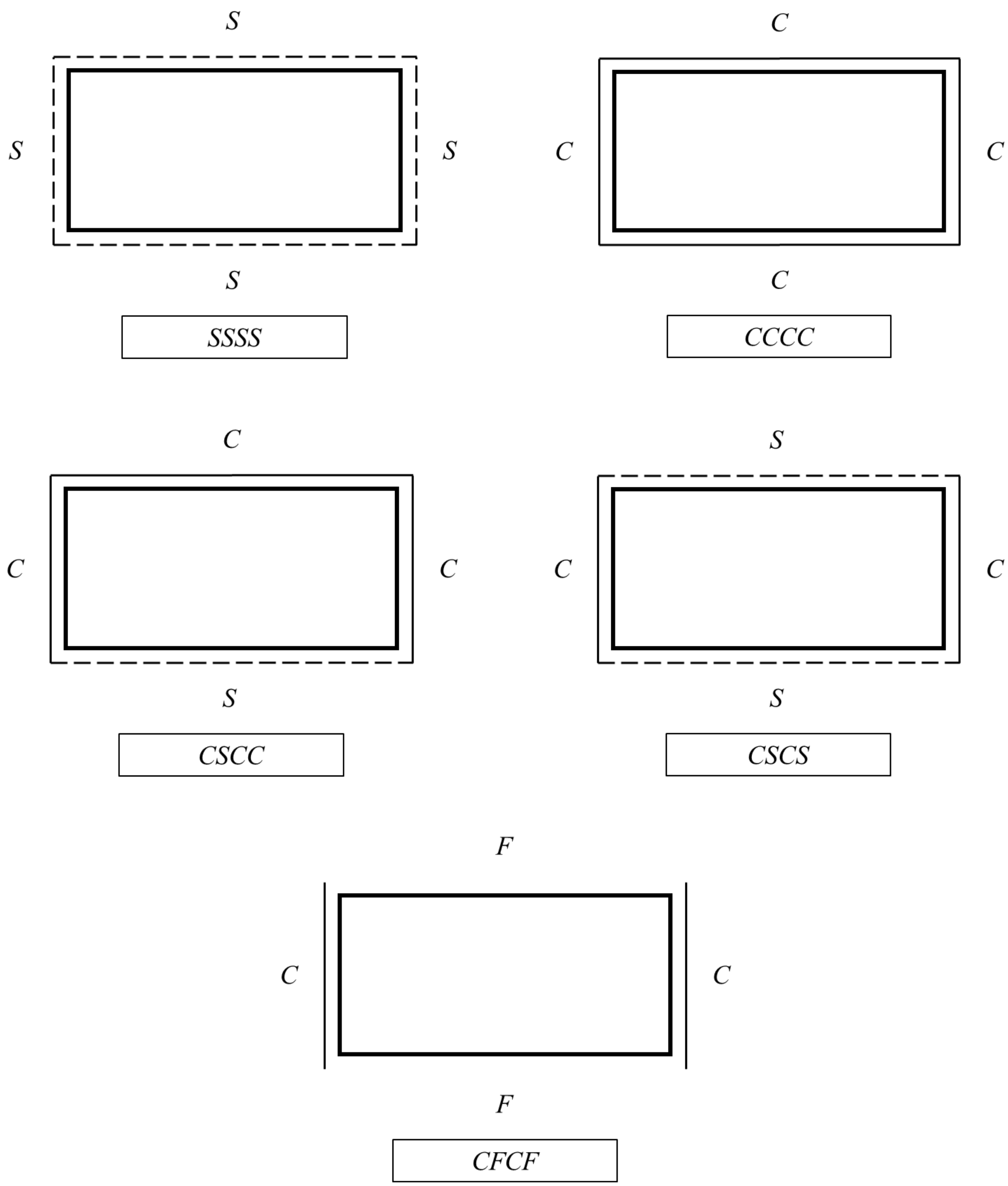

Figure 3.1 The boundary conditions employed in the numerical examples.

3.2 Convergence and accuracy study

Table 3.3 assesses the accuracy and convergence rate of the proposed numerical model. The study explores the effects of power-law index (k) and radius-to-thickness ratios (R/h) on the DTD of a simply supported FG (Al/ZrO_2) CY shells, with dimensions $a = b = 0.2$ m and $R = 1$ m, under a uniform load. The numerical results obtained are compared with those reported by:

- Sayyad and Ghugal [223] employed the Navier method based on HSDT.
- Huan et al. [297] applied FSDT combined with the Navier approach.
- Zhao et al. [167] used FSDT in conjunction with the element-free kp-Ritz method.
- Viola et al. [298] utilized UTSDT via the GDQ method.

The results obtained for various mesh sizes (e.g., 2×2, 4×4, up to 14×14) under the SQ8-IFSDT model demonstrate that the DTD stabilizes as the mesh size increases. Beyond a mesh size of approximately 8×8, the displacement values show minimal variation, indicating that the numerical solution converges rapidly with finer mesh refinement. Additionally, the displacement increases with the increase of the index (k) for all (R/h) ratios. The results predicted by the SQ8-IFSDT model exhibit close agreement with those from other models (HSDT and UTSDT), confirming the high consistency and reliability of the proposed model.

Table 3.3 The DTD (w^*) of FG (Al/ZrO_2) CY shells subjected to a uniform load for various power-law index (k) and (R/h) ratio.

Reference	**Model**	**Power-law index (*k*)**								
		***k* = 1**			***k* = 2**			***k* = 10**		
		R/h			***R/h***			***R/h***		
		50	**100**	**200**	**50**	**100**	**200**	**50**	**100**	**200**
Present (2×2)	SQ8-IFSDT	0.00406	0.05304	0.55877	0.00446	0.05856	0.62271	0.00517	0.06852	0.74199
Present (4×4)	SQ8-IFSDT	0.00429	0.06081	0.72662	0.00470	0.06671	0.80407	0.00544	0.07727	0.94810
Present (6×6)	SQ8-IFSDT	0.00429	0.06088	0.72770	0.00471	0.06678	0.80525	0.00544	0.07735	0.94948
Present (8×8)	SQ8-IFSDT	0.00429	0.06089	0.72786	0.00471	0.06679	0.80542	0.00544	0.07736	0.94966
Present (10×10)	SQ8-IFSDT	0.00429	0.06089	0.72789	0.00471	0.06679	0.80545	0.00544	0.07736	0.94970
Present (12×12)	SQ8-IFSDT	0.00429	0.06089	0.72790	0.00471	0.06679	0.80546	0.00544	0.07736	0.94971
Present (14×14)	SQ8-IFSDT	0.00429	0.06089	0.72790	0.00471	0.06679	0.80547	0.00544	0.07736	0.94972
Sayyad and Ghugal [223]	HSDT	0.00428	0.06067	0.72607	0.00469	0.06654	0.80339	0.00542	0.07709	0.94728
Huan et al. [297]	FSDT	0.00430	0.06091	0.72710	0.0047	0.06679	0.80560	-	-	-
Zhao et al. [167]	FSDT	0.00428	0.06072	0.72830	0.00469	0.06678	0.80570	-	-	-
Viola et al. [298]	UTSDT	0.00431	-	0.72940	0.00473	-	0.80706	-	-	-

3.3 Parameter study

Example 1:

Table 3.4 applies the current FE model to examine the DTD of FG (Al/Al_2O_3) DCSSs under a sinusoidal load distribution with power-law index (*k*). Numerical results obtained from the proposed FE model are compared to findings from:

- Tati [299] developed a Q4-FE model based on HSDT.
- Zenkour [58] utilized HSDT with the Navier approach.
- Benyoucef et al. [300] employed Navier technique based on HSDT.
- Mechab et al. [301] applied the Navier method using the two-variable refined plate theory.
- Rachid et al. [226] employed Navier's solution based on HSDT.

Notably, for the four shallow shell types—CY, SP, HYP, and ELP, this study presents new numerical results that, to the best of the authors' knowledge, are reported for the first time in the literature. As such, no direct comparisons with existing data are available. As observed in **Table 3.4**, increasing the index (*k*) leads to greater deflection in the shell. This trend results from the increased metal volume fraction with higher *k*, which decreases the shells' rigidity. Furthermore, for shells with similar dimensions and power-law index, SP shells demonstrate the lowest deflection, while HYP shells show the highest.

Table 3.4 The DTDs ($\bar{w}$) of FG (Al/Al_2O_3) DCSSs subjected to sinusoidal load with various power-law index (*k*).

Types of shell	Reference	Model	Power-law index (*k*)						
			***k* = 0**	***k* = 1**	***k* = 2**	***k* = 4**	***k* = 5**	***k* = 10**	***k* = ∞**
CY shell ($R_x/a = 5$, $R_y/b = \infty$)	Present	SQ8-IFSDT	0.2885	0.5721	0.7365	0.8597	0.8898	0.9885	1.5565
SP shell ($R_x/a = 5$, $R_y/b = 5$)	Present	SQ8-IFSDT	0.2660	0.5212	0.6719	0.7925	0.8232	0.9216	1.4354
HYP shell ($R_x/a = 5$, $R_y/b = -5$)	Present	SQ8-IFSDT	0.2985	0.5938	0.7636	0.8879	0.9177	1.0170	1.6103
ELP shell ($R_x/a = 5$, $R_y/b = 7.5$)	Present	SQ8-IFSDT	0.2745	0.5406	0.6965	0.8183	0.8488	0.9473	1.4816
FL plate ($R_x/a = \infty$, $R_y/b = \infty$)	Present	SQ8-IFSDT	0.2960	0.5889	0.7574	0.8806	0.9102	1.0087	1.5971
	Tati [57]	Q4-HSDT	0.2957	0.5882	0.7575	0.8832	0.9136	1.0125	-
	Zenkour [58]	HSDT	0.2960	0.5889	0.7573	0.8819	0.9118	1.0089	1.6070
	Benyoucef et al. [59]	HSDT	0.2960	0.5889	0.7572	0.8810	0.9108	1.0083	1.6071
	Mechab et al. [60]	RPT	0.2961	0.5890	0.7573	0.8816	0.9112	1.0089	-
	Rachid et al. [52]	HSDT	0.2960	0.5889	0.7573	0.8818	0.9117	-	1.6070

Example 2:

Table 3.5 presents the DTD of FG (Al/ZrO_2) DCSSs subjected to a uniformly distributed load. The analysis is conducted for shells with dimensions $a = b = 0.2$ m and $h = R_x/100$. The influence of the power-law index (k) and various boundary conditions (SSSS, CCCC, CSCS, and CFCF) is thoroughly examined. To validate the accuracy of the proposed numerical model, results for CY shells are compared with those reported by Zhao et al. [167] and Viola et al. [298] under different boundary conditions. The comparison confirms good agreement, reinforcing the credibility of the model.

Overall, the results indicate that increasing the index (k) leads to higher DTD values. This behavior is attributed to the decrease in ceramic content and the corresponding increase in metallic volume fraction with higher k, which reduces the shell's stiffness and results in greater displacement.

Table 3.5 The DTDs ($\bar{w}$) of FG (Al/ZrO_2) DCSSs subjected to uniform load for different boundary conditions.

Types of shell	BCs	Reference	Model	Power-law index (*k*)					
				k **= 0**	***k*** **= 0.2**	***k*** **= 0.5**	***k*** **= 1**	***k*** **= 2**	***k*** **= 5**
CY shell (R_x/a = 1, R_y/b = ∞)	SSSS	Present	SQ8-IFSDT	0.0427	0.0481	0.0543	0.0608	0.0667	0.0726
		Zhao et al. [167]	FSDT	0.0427	0.0481	0.0543	0.0608	0.0667	0.0725
		Viola et al. [298]	UTSDT	0.0429	0.0483	0.0546	0.0611	0.0670	0.0728
	CCCC	Present	SQ8-IFSDT	0.0137	0.0154	0.0174	0.0195	0.0215	0.0234
		Zhao et al. [167]	FSDT	0.0134	0.0151	0.0170	0.0190	0.0209	0.0227
		Viola et al. [298]	UTSDT	0.0138	0.0155	0.0175	0.0196	0.0215	0.0234
	CSCS	Present	SQ8-IFSDT	0.0216	0.0243	0.0275	0.0308	0.0338	0.0367
		Zhao et al. [167]	FSDT	0.0212	0.0239	0.0270	0.0302	0.0331	0.0359
		Viola et al. [298]	UTSDT	0.0217	0.0244	0.0276	0.0309	0.0339	0.0368
	CFCF	Present	SQ8-IFSDT	0.0277	0.0311	0.0350	0.0392	0.0433	0.0475
		Zhao et al. [167]	FSDT	0.0277	0.0313	0.0353	0.0395	0.0433	0.0470
		Viola et al. [298]	UTSDT	0.0288	0.0324	0.0366	0.0410	0.0449	0.0488
SP shell (R_x/a = 1, R_y/b = 1)	SSSS	Present	SQ8-IFSDT	0.0324	0.0363	0.0408	0.0458	0.0507	0.0560
	CCCC	Present	SQ8-IFSDT	0.0118	0.0133	0.0150	0.0168	0.0185	0.0204
	CSCS	Present	SQ8-IFSDT	0.0178	0.0199	0.0225	0.0252	0.0278	0.0306
	CFCF	Present	SQ8-IFSDT	0.0271	0.0304	0.0342	0.0383	0.0423	0.0465
HYP shell (R_x/a = 1, R_y/b = -1)	SSSS	Present	SQ8-IFSDT	0.0480	0.0542	0.0613	0.0686	0.0749	0.0809
	CCCC	Present	SQ8-IFSDT	0.0130	0.0146	0.0165	0.0185	0.0204	0.0223
	CSCS	Present	SQ8-IFSDT	0.0194	0.0219	0.0246	0.0276	0.0304	0.0332
	CFCF	Present	SQ8-IFSDT	0.0266	0.0298	0.0336	0.0376	0.0415	0.0457
ELP shell (R_x/a = 1, R_y/b = 1.5)	SSSS	Present	SQ8-IFSDT	0.0360	0.0404	0.0454	0.0509	0.0562	0.0617
	CCCC	Present	SQ8-IFSDT	0.0127	0.0142	0.0161	0.0180	0.0198	0.0217
	CSCS	Present	SQ8-IFSDT	0.0195	0.0219	0.0247	0.0277	0.0305	0.0334
	CFCF	Present	SQ8-IFSDT	0.0275	0.0308	0.0347	0.0389	0.0429	0.0471

Figure 3.2 depicts the influence of the power-law index (k) on DTDs of FG (Al/ZrO_2) DCSSs under various boundary conditions. The results show that, for all shell types and boundary conditions, DTDs increase sharply as (k) rises from 0 to 2, after which the rate of increase becomes more gradual. The figure also highlights the significant role of boundary conditions in the bending behavior of the shells. Among the studied cases, shells with simply supported (SSSS) boundaries exhibit the largest displacements, whereas those with fully clamped (CCCC) boundaries show the smallest, for the same value of (k).

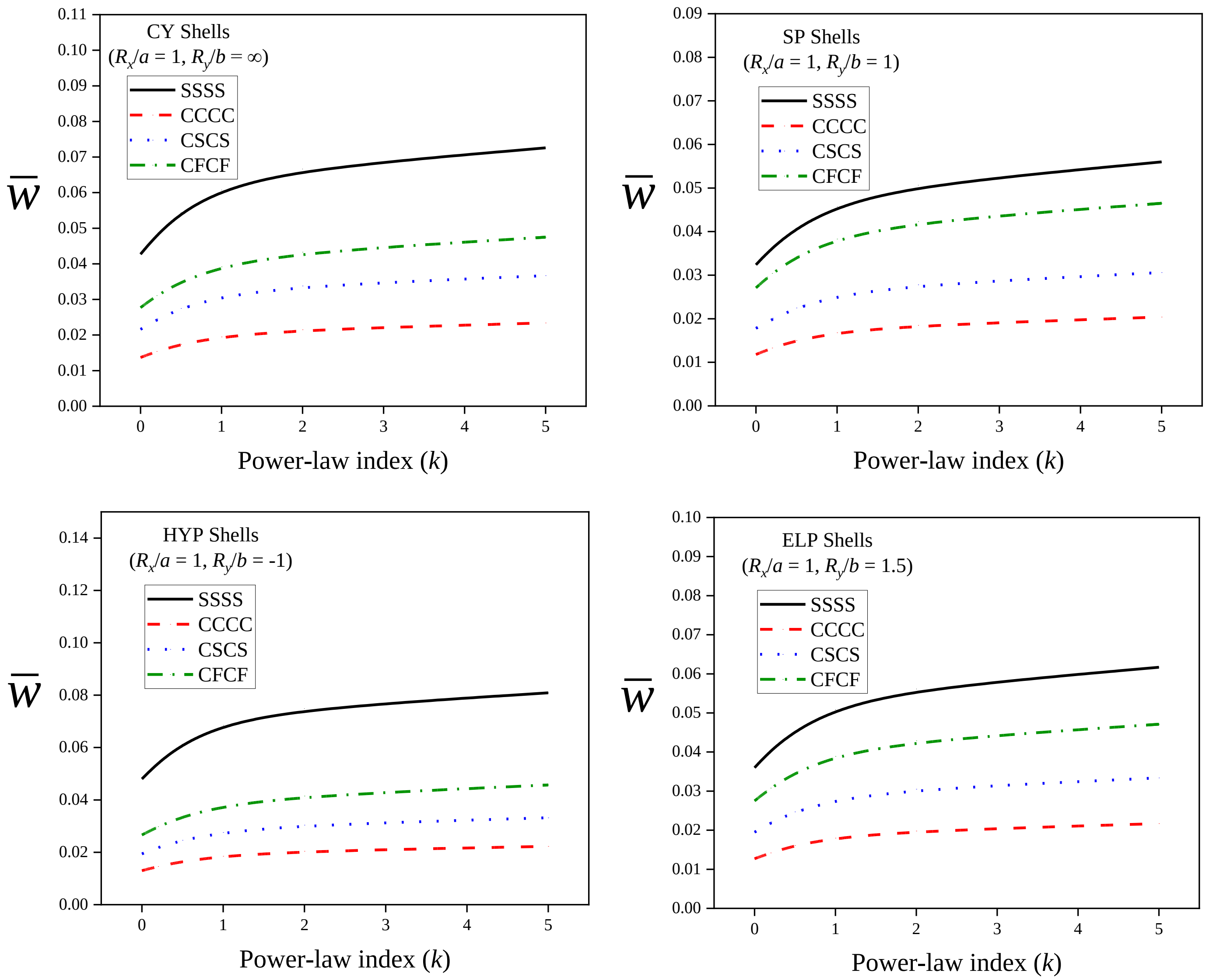

Figure 3.2 The effects of boundary conditions on the DTD of FG (Al/ZrO_2) DCSSs subjected to uniform load with different power-law index (k).

Example 3:

Table 3.6 investigates the effects of the shell curvature on the DTD of FG (Al/Al_2O_3) DCSSs with a/h = 10 and k = 2. The present results compared with FSDT and HSDT analytical solutions from Sayyad and Ghugal [223]. The comparison reveals strong agreement, particularly with the HSDT-based solutions, indicating that the proposed FE model is accurate and reliable for analyzing the bending behavior of FG DCSSs with varying curvatures.

For CY, SP, and ELP shells, an increase in the radii of curvature leads to greater transverse deflections. In contrast, HYP shells exhibit reduced deflections as the curvature increases. However, as the radii of curvature become sufficiently large, the deflections of all shell types tend to converge, reflecting the behavior of flat plates in the shallow shell limit.

Example 4:

This section investigates the dimensionless normal and shear stresses of FG (Al/Al_2O_3) DCSSs for various power-law index (k) as presented in **Table 3.7**. The results are compared with those from Sayyad and Ghugal [223], showing excellent agreement in both normal and shear stress values. The results from the SQ8-IFSDT model are close with those obtained with Navier's solution based on HSDT. These findings confirm that the proposed FE model is both reliable and accurate for the analysis of displacement and stress in FG DCSSs.

Table 3.6 The DTDs ($\bar{w}$) of FG (Al/Al_2O_3) DCSSs under a uniform load for different power-law index (k).

Types of shell	k	Present (2×2)	Present (4×4)	Present (6×6)	Present (8×8)	Present (10×10)	Present (12×12)	Present (14×14)	Sayyad and Ghugal [223]			
		SQ8-IFSDT	SQ8-IFSDT	SQ8-IFSDT	SQ8-IFSDT	SQ8-IFSDT	SQ8-IFSDT	SQ8-IFSDT	FSDT	Difference (%)	HSDT	Difference (%)
CY shell (R_x/a = 5, R_y/b = ∞)	0	4.2986	4.5391	4.5427	4.5433	4.5434	4.5435	4.5435	4.4921	1.1442	4.5264	0.3778
	1	8.4820	9.0072	9.0146	9.0157	9.016	9.0161	9.0161	8.9072	1.2226	8.9670	0.5476
	5	13.315	13.988	13.999	14.001	14.001	14.001	14.001	13.683	2.3241	13.931	0.5025
	10	14.826	15.529	15.541	15.543	15.544	15.544	15.544	15.152	2.5871	15.458	0.5563
	∞	23.197	24.489	24.509	24.512	24.513	24.513	24.513	24.385	0.5249	24.571	-0.2361
SP shell (R_x/a = 5, R_y/b = 5)	0	3.9750	4.1753	4.1782	4.1786	4.1787	4.1788	4.1788	4.1285	1.2184	4.1570	0.5244
	1	7.7599	8.1845	8.1902	8.191	8.1912	8.1913	8.1913	8.0729	1.4666	8.1211	0.8644
	5	12.347	12.912	12.921	12.922	12.923	12.923	12.923	12.601	2.5554	12.807	0.9058
	10	13.846	14.448	14.458	14.460	14.460	14.460	14.460	14.071	2.7646	14.331	0.9001
	∞	21.456	22.534	22.550	22.552	22.553	22.553	22.553	22.412	0.6291	22.566	-0.0576
HYP shell (R_x/a = 5, R_y/b = -5)	0	4.4329	4.7005	4.7050	4.7056	4.7058	4.7059	4.7059	4.6278	1.6876	4.6644	0.8897
	1	8.7660	9.3562	9.3656	9.3669	9.3673	9.3674	9.3675	9.2246	1.5491	9.2892	0.8429
	5	13.692	14.439	14.452	14.454	14.455	14.455	14.455	14.086	2.6196	14.350	0.7317
	10	15.217	15.991	16.005	16.008	16.008	16.009	16.009	15.550	2.9518	15.874	0.8504
	∞	23.918	25.356	25.381	25.384	25.385	25.386	25.386	25.122	1.0509	25.321	0.2567
ELP shell (R_x/a =5, R_y/b =7.5)	0	4.0995	4.3139	4.3171	4.3175	4.3177	4.3177	4.3177	4.2694	1.1313	4.3001	0.4093
	1	8.0378	8.4979	8.5041	8.505	8.5052	8.5053	8.5053	8.3937	1.3296	8.4461	0.7009
	5	12.722	13.325	13.335	13.336	13.337	13.337	13.337	13.021	2.4268	13.243	0.7098
	10	14.226	14.864	14.875	14.876	14.877	14.877	14.877	14.493	2.6496	14.770	0.7244
	∞	22.126	23.279	23.296	23.299	23.300	23.300	23.300	23.177	0.5307	23.343	-0.1842
FL plate (R_x/a = ∞, R_y/b = ∞)	0	4.4110	4.6615	4.6651	4.6657	4.6658	4.6650	4.6659	4.6273	0.8342	4.6639	0.0429
	1	8.7279	9.2791	9.2866	9.2876	9.2879	9.2880	9.2881	9.2235	0.7004	9.2880	0.0011
	5	13.623	14.319	14.330	14.332	14.332	14.333	14.333	14.085	1.7607	14.348	-0.1045
	10	15.135	15.857	15.870	15.872	15.872	15.872	15.872	15.548	2.0839	15.872	0.0000
	∞	23.800	25.146	25.166	25.169	25.170	25.170	25.170	25.120	0.1990	25.318	-0.5846

Difference (%) = [(Present result − Analytical result) / Analytical result] × 100

Table 3.7 The effects of the power-law index (k) on the dimensionless normal and shear stresses of FG (Al/Al_2O_3) DCSSs under uniform load.

k	Stresses	CY shell (R_x/a = 5, R_y/b = ∞)			SP shell (R_x/a = 5, R_y/b =5)			HYP shell (R_x/a = 5, R_y/b = -5)			ELP shell (R_x/a = 5, R_y/b = 7.5)		
		Present	Sayyad and Ghugal [223]		Present	Sayyad and Ghugal [223]		Present	Sayyad and Ghugal [223]		Present	Sayyad and Ghugal [223]	
		SQ8-IFSDT	FSDT	HSDT	SQ8-IFSDT	FSDT	HSDT	SQ8-IFSDT	FSDT	HSDT	SQ8-IFSDT	FSDT	HSDT
0	$\bar{\sigma}_x\left(\frac{L}{2},\frac{l}{2},\frac{h}{2}\right)$	2.9934	3.0029	3.0216	2.9501	2.9519	2.9679	2.8630	2.8663	2.8848	2.9819	2.9876	3.0048
	$\bar{\sigma}_y\left(\frac{L}{2},\frac{l}{2},\frac{h}{3}\right)$	2.0953	-	-	2.1024	-	-	1.9527	-	-	2.1140	-	-
	$\bar{\tau}_{xy}\left(0,0,-\frac{h}{3}\right)$	1.5075	-	-	1.6251	-	-	1.2999	-	-	1.5961	-	-
	$\bar{\tau}_{xz}\left(0,\frac{l}{2},0\right)$	0.5083	0.3227	0.4781	0.4765	0.3027	0.4480	0.5210	0.3299	0.4888	0.4888	0.3105	0.4597
	$\bar{\tau}_{yz}\left(\frac{L}{2},0,\frac{h}{6}\right)$	0.4517	-	-	0.4236	-	-	0.4631	-	-	0.4344	-	-
1	$\bar{\sigma}_x\left(\frac{L}{2},\frac{l}{2},\frac{h}{2}\right)$	4.6990	4.7137	4.7460	4.6554	4.6503	4.6777	4.4127	4.4273	4.4594	4.7028	4.7061	4.7356
	$\bar{\sigma}_y\left(\frac{L}{2},\frac{l}{2},\frac{h}{3}\right)$	2.5072	-	-	2.5811	-	-	2.2333	-	-	2.5776	-	-
	$\bar{\tau}_{xy}\left(0,0,-\frac{h}{3}\right)$	1.2420	-	-	1.2817	-	-	1.1225	-	-	1.2769	-	-
	$\bar{\tau}_{xz}\left(0,\frac{l}{2},0\right)$	0.5115	0.3215	0.4782	0.4749	0.2984	0.4435	0.5257	0.3298	0.4908	0.4890	0.3073	0.4569
	$\bar{\tau}_{yz}\left(\frac{L}{2},0,\frac{h}{6}\right)$	0.5599	-	-	0.5191	-	-	0.5769	-	-	0.5346	-	-
5	$\bar{\sigma}_x\left(\frac{L}{2},\frac{l}{2},\frac{h}{2}\right)$	6.5463	6.5701	6.6370	6.6677	6.6545	6.7149	6.0268	6.0635	6.1238	6.6693	6.6706	6.7344
	$\bar{\sigma}_y\left(\frac{L}{2},\frac{l}{2},\frac{h}{3}\right)$	1.9532	-	-	2.0889	-	-	1.6798	-	-	2.0591	-	-
	$\bar{\tau}_{xy}\left(0,0,-\frac{h}{3}\right)$	1.1710	-	-	1.2190	-	-	1.0598	-	-	1.2099	-	-
	$\bar{\tau}_{xz}\left(0,\frac{l}{2},0\right)$	0.3880	0.2115	0.3874	0.3645	0.1987	0.3633	0.3970	0.2161	0.3959	0.3736	0.2037	0.3727
	$\bar{\tau}_{yz}\left(\frac{L}{2},0,\frac{h}{6}\right)$	0.4808	-	-	0.4506	-	-	0.4935	-	-	0.4622	-	-

Table 3.7 Continued

10	$\bar{\sigma}_x\left(\frac{L}{2},\frac{l}{2},\frac{h}{2}\right)$	7.8092	7.8392	7.9161	7.9688	7.9565	8.0275	7.2286	7.2713	7.3393	7.9605	7.9652	8.0396
	$\bar{\sigma}_y\left(\frac{L}{2},\frac{l}{2},\frac{h}{3}\right)$	1.5194	-	-	1.6091	-	-	1.3356	-	-	1.5897	-	-
	$\bar{\tau}_{xy}\left(0,0,-\frac{h}{3}\right)$	1.2147	-	-	1.2832	-	-	1.0860	-	-	1.2671	-	-
	$\bar{\tau}_{xz}\left(0,\frac{l}{2},0\right)$	0.4297	0.2318	0.4255	0.4061	0.2191	0.4016	0.4388	0.2362	0.4339	0.4153	0.2241	0.4110
	$\bar{\tau}_{yz}\left(\frac{L}{2},0,\frac{h}{6}\right)$	0.4103	-	-	0.3870	-	-	0.4200	-	-	0.3960	-	-

Table 3.8 presents the dimensionless normal and shear stresses of FG (Al/Al2O3) DCSSs for different the effects radius-to-length ratio (R_x/a) under uniform and sinusoidal scenarios with a = 10h, and k = 2. As Rx/a increases, both normal and shear stresses generally decrease for all shell types, with CY shells exhibiting the highest stresses and hyperbolic paraboloid shells the lowest. Shear stresses are less sensitive to changes in R_x/a compared to normal stresses. Additionally, sinusoidal loads result in slightly lower stress values than uniform loads, particularly for larger R_x/a values.

Table 3.8 The effects of the radius-to-length ratio (R_x/a) on the dimensionless normal and shear of FG (Al/Al_2O_3) DCSSs under uniform and sinusoidal loads.

R_x/a	Types of shell	CY shell ($R_y/b = \infty$)		SP shell ($R_y/b = R_x/a$)		HYP shell ($R_y/b = -R_x/a$)		ELP shell ($R_y/b = 1.5\times R_x/a$)	
	Load type	**UL**	**SL**	**UL**	**SL**	**UL**	**SL**	**UL**	**SL**
5	$\bar{\sigma}_x$	5.5386	3.8037	5.5407	3.8066	5.1444	3.5557	5.5797	3.8305
	$\bar{\sigma}_y$	2.4280	1.6464	2.5518	1.7339	2.1058	1.4360	2.5321	1.7181
	$\bar{\tau}_{xy}$	1.0984	0.6074	1.1274	0.6233	1.0005	0.5492	1.1250	0.6224
	$\bar{\tau}_{xz}$	0.4605	0.2224	0.4279	0.2027	0.4731	0.2304	0.4405	0.2102
	$\bar{\tau}_{yz}$	0.5778	0.2798	0.5358	0.2538	0.5955	0.2906	0.5519	0.2637
10	$\bar{\sigma}_x$	5.4160	3.7207	5.5719	3.8182	5.1599	3.5606	5.5313	3.7928
	$\bar{\sigma}_y$	2.2588	1.5412	2.3980	1.6328	2.0729	1.4207	2.3571	1.6056
	$\bar{\tau}_{xy}$	1.0562	0.5823	1.0974	0.6067	0.9980	0.5475	1.0856	0.5998
	$\bar{\tau}_{xz}$	0.4696	0.2282	0.4607	0.2227	0.4727	0.2301	0.4643	0.2249
	$\bar{\tau}_{yz}$	0.5888	0.2863	0.5768	0.2789	0.5934	0.2892	0.5816	0.2818
20	$\bar{\sigma}_x$	5.3151	3.6546	5.4333	3.7284	5.1726	3.5658	5.3967	3.7055
	$\bar{\sigma}_y$	2.1572	1.4780	2.2451	1.5351	2.0585	1.4142	2.2170	1.5168
	$\bar{\tau}_{xy}$	1.0287	0.5658	1.0559	0.5821	0.9974	0.5471	1.0473	0.5770
	$\bar{\tau}_{xz}$	0.4720	0.2297	0.4698	0.2283	0.4727	0.2301	0.4707	0.2289
	$\bar{\tau}_{yz}$	0.5914	0.2879	0.5883	0.2859	0.5927	0.2887	0.5896	0.2867
50	$\bar{\sigma}_x$	5.2422	3.6073	5.2988	3.6426	5.1818	3.5697	5.2804	3.6311
	$\bar{\sigma}_y$	2.0913	1.4370	2.1304	1.4623	2.0505	1.4107	2.1176	1.4539
	$\bar{\tau}_{xy}$	1.0102	0.5548	1.0226	0.5622	0.9972	0.5470	1.0186	0.5598
	$\bar{\tau}_{xz}$	0.4728	0.2301	0.4725	0.2299	0.4728	0.2302	0.4726	0.2300
	$\bar{\tau}_{yz}$	0.5921	0.2883	0.5916	0.2879	0.5924	0.2884	0.5918	0.2881
100	$\bar{\sigma}_x$	5.2159	3.5903	5.2457	3.6089	5.1851	3.5712	5.2359	3.6028
	$\bar{\sigma}_y$	2.0685	1.4228	2.0887	1.4358	2.0480	1.4095	2.0820	1.4315
	$\bar{\tau}_{xy}$	1.0038	0.5509	1.0102	0.5548	0.9972	0.5470	1.0081	0.5535
	$\bar{\tau}_{xz}$	0.4729	0.2302	0.4728	0.2302	0.4729	0.2302	0.4729	0.2302
	$\bar{\tau}_{yz}$	0.5922	0.2883	0.5921	0.2882	0.5923	0.2884	0.5921	0.2883

Figures 3.3 and **3.4** illustrate the distribution of normal stresses through the thickness of FG (Al/Al_2O_3) DCSSs with a side-to-thickness ratio of $a/h = 4$. When the power-law index (k) is equal to 0, the stress distribution is linear and symmetrical. However, for k > 0, the stress distribution becomes nonlinear and asymmetrical, with the maximum normal stress occurring at the top surface and the minimum at the bottom.

Figure 3.5 shows the distribution of in-plane shear stress across the thickness of FG (Al/Al_2O_3) DCSSs with a side-to-thickness ratio of $a/h = 4$. For homogeneous shells ($k = 0$), the in-plane shear stress follows a linear and symmetric profile. However, for $k > 0$, the distribution becomes nonlinear and asymmetric.

Figures 3.6 and **3.7** show the distribution of out-plane shear stress across the thickness of FG (Al/Al_2O_3) DCSSs with a side-to-thickness ratio of $a/h = 4$. The present FE model accurately predicts a parabolic distribution with zero transverse shear stresses at the top and bottom surfaces of the FG DCSSs.

Figures 3.8–3.12 illustrate the effects of side-to-thickness ratio (a/h) on the normal and shear stresses in FG (Al/Al_2O_3) DCSSs. The impact of (a/h) on these stresses varies depending on the shell type. For normal and in-plane shear stresses, the relationship is nonlinear for CY, SP, and ELP shells but linear for HYP FG shells and FL FG plates. In contrast, for out-of-plane shear stresses, the dependence is nonlinear across all cases, including CY, SP, HYP, and ELP shells, as well as FL plates.

Finally, **Figures 3.13–3.17** show the distribution of normal and shear stresses through the thickness of shells with different radius- to-side ratio, with a side-to-thickness ratio of $a/h = 20$ and a power-law index $k = 5$. The stress distributions in CY, SP, and ELP shells are significantly influenced by curvature, while HYP shells show minimal sensitivity to changes in curvature.

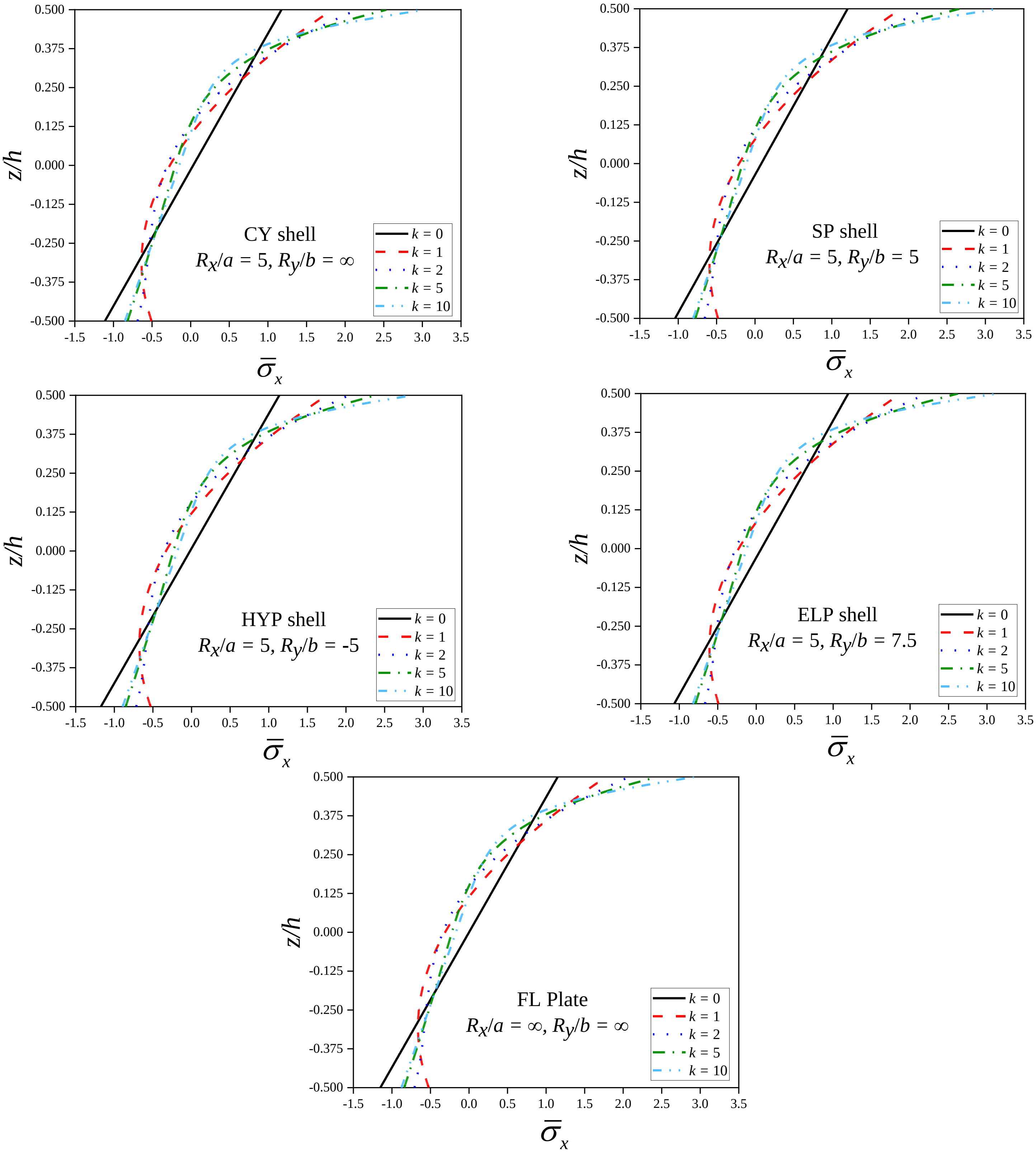

Figure 3.3 Through-thickness distributions of the normalized axial stress ($\bar{\sigma}_x$) for FG (Al/Al_2O_3) DCSSs with different index (k) subjected to a uniform load.

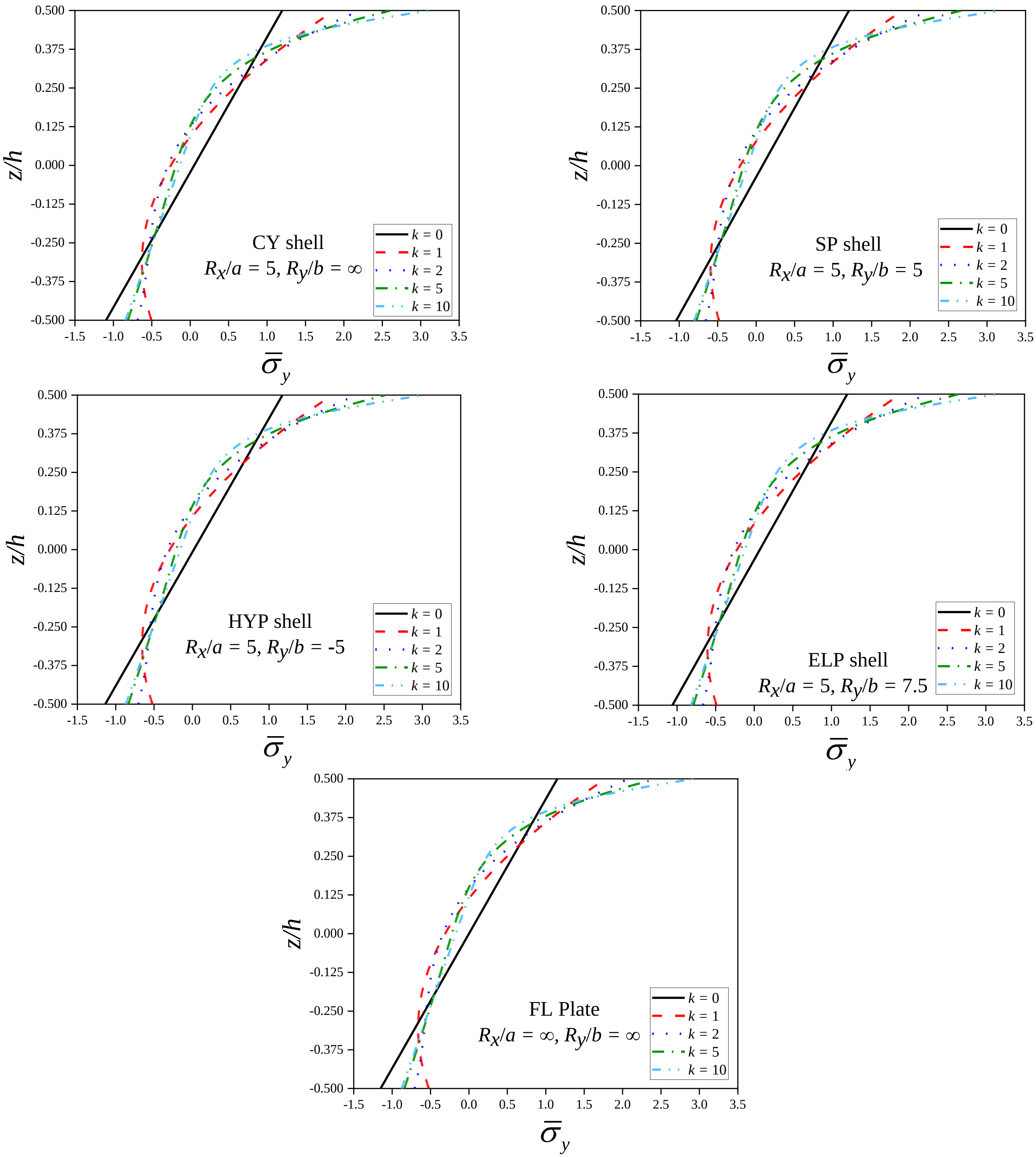

Figure 3.4 Through-thickness distributions of the normalized axial stress ($\bar{\sigma}_y$) for FG (Al/Al_2O_3) DCSSs with different index (k) subjected to a uniform load.

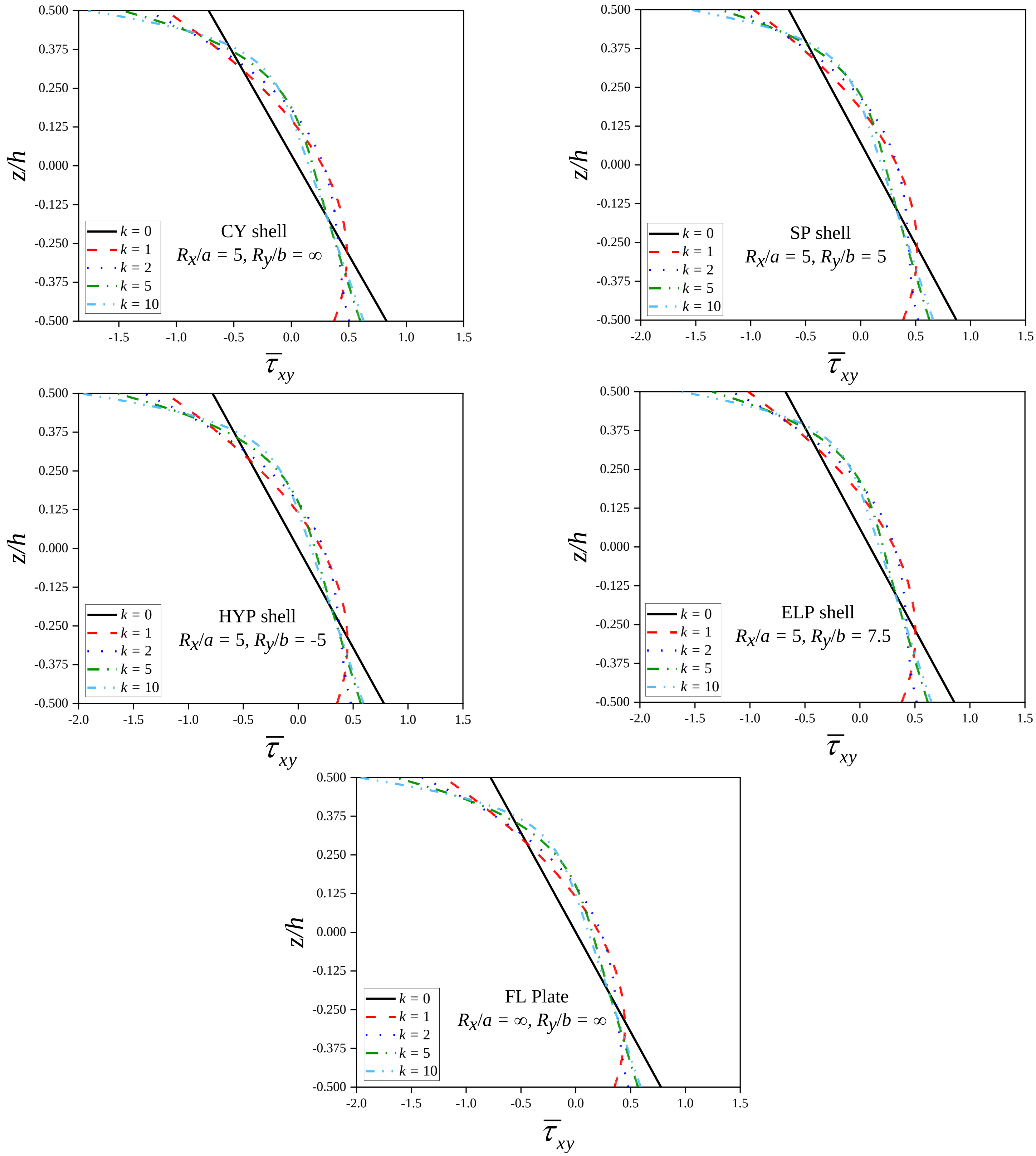

Figure 3.5 Through-thickness distributions of the in-plane shear stress ($\bar{\tau}_{xy}$) for FG (Al/Al_2O_3) DCSSs with different index (k) subjected to a uniform load.

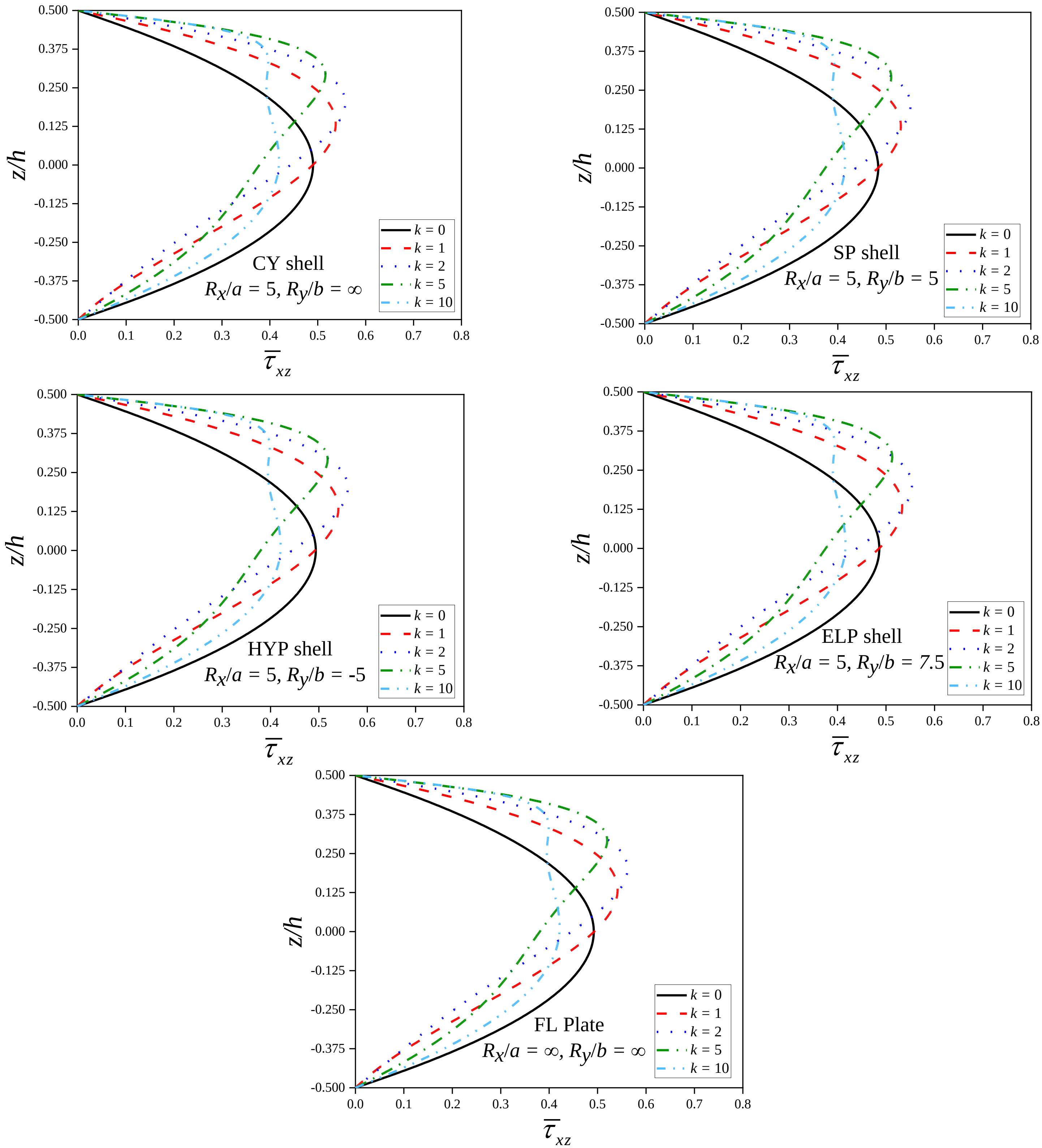

Figure 3.6 Through-thickness distributions of the out-of-plane shear stress ($\bar{\tau}_{xz}$) for FG (Al/Al_2O_3) DCSSs with different index (k) subjected to a uniform load.

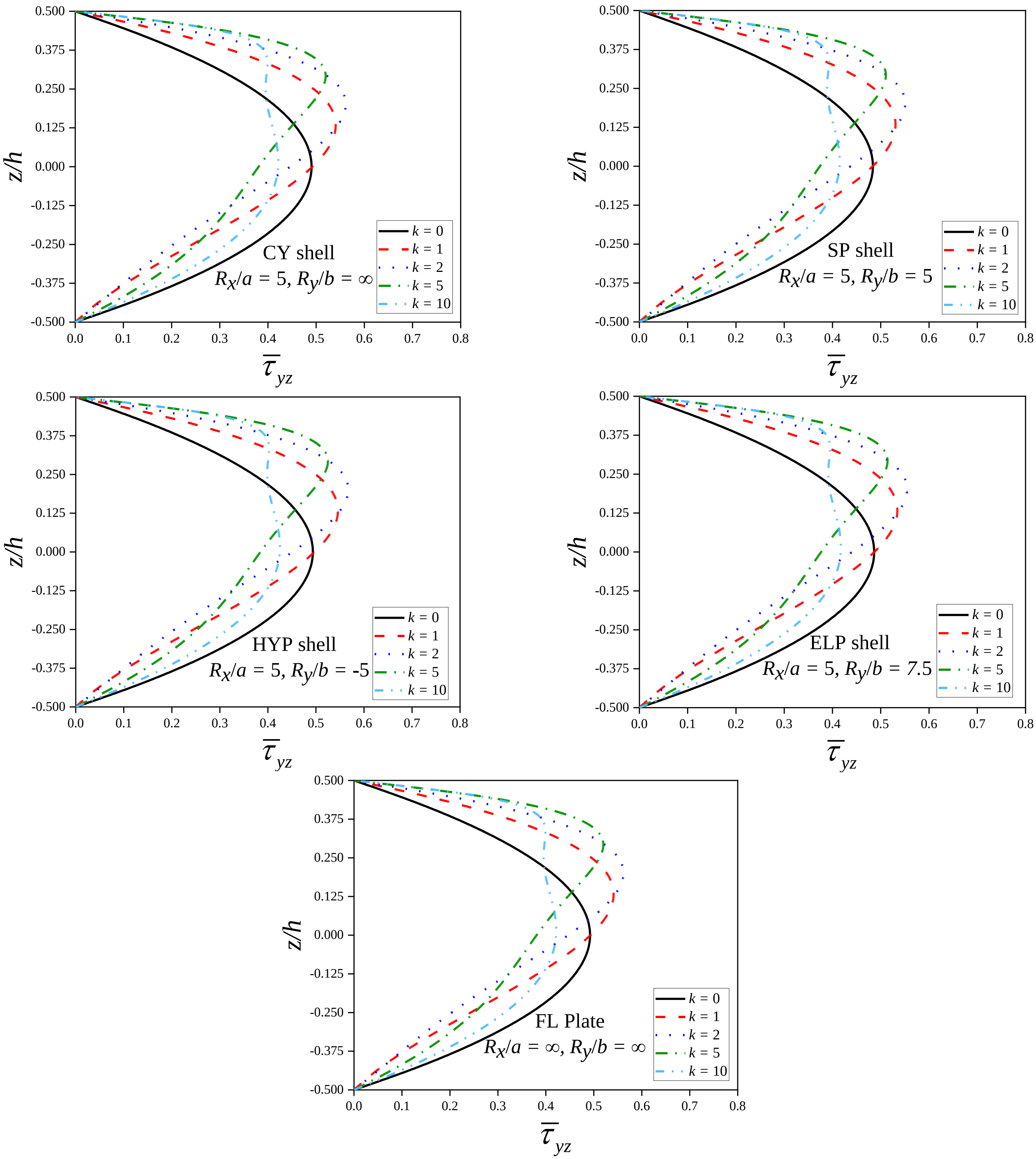

Figure 3.7 Through-thickness distributions of the out-of-plane shear stress ($\bar{\tau}_{yz}$) for FG (Al/Al_2O_3) DCSSs with different index (k) subjected to a uniform load.

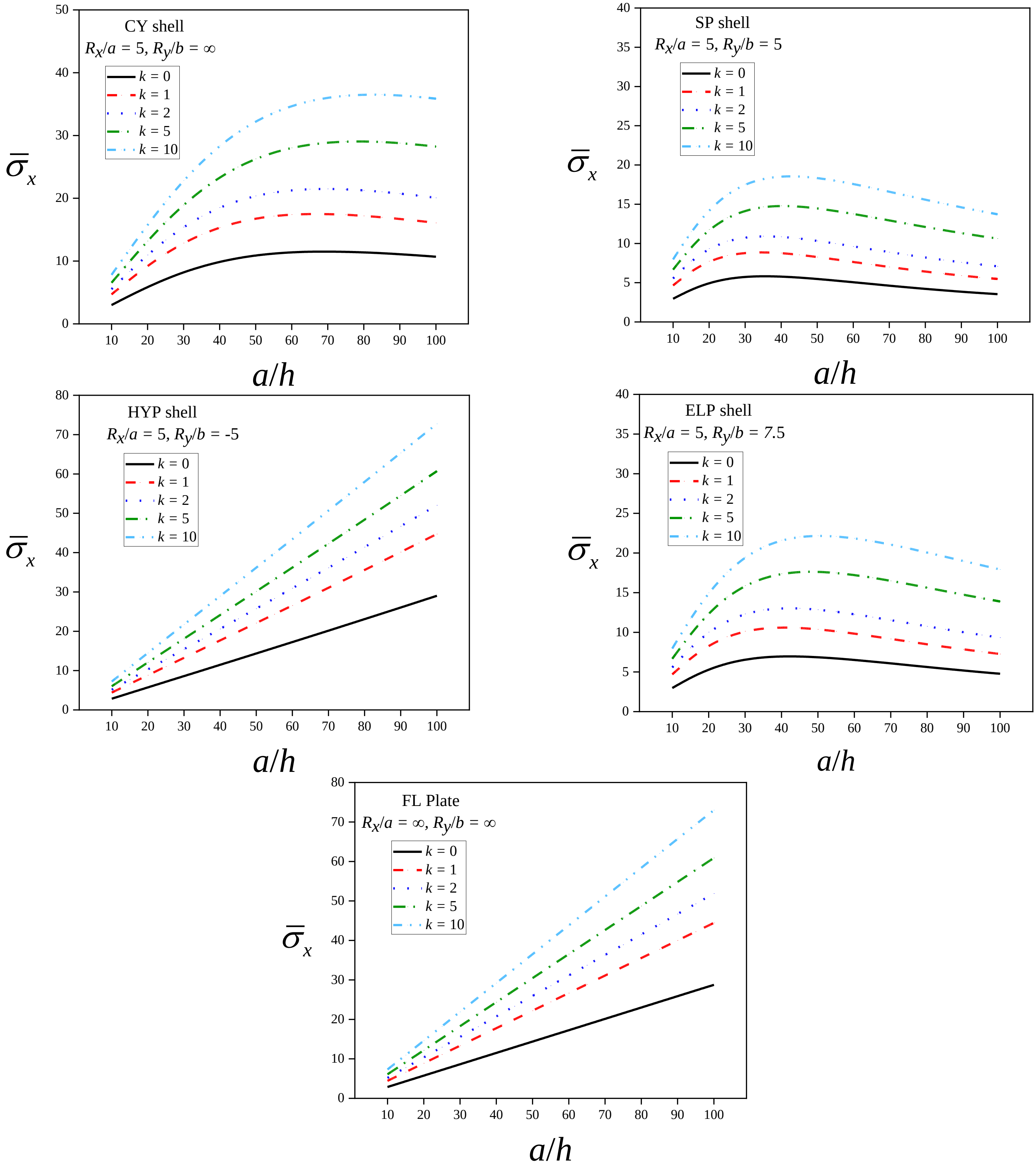

Figure 3.8 Normalized axial stress ($\bar{\sigma}_x$) versus side-to-thickness ratio (a/h) for FG (Al/Al_2O_3) DCSSs with various index (k) subjected to a uniform load. ($z = h/2$)

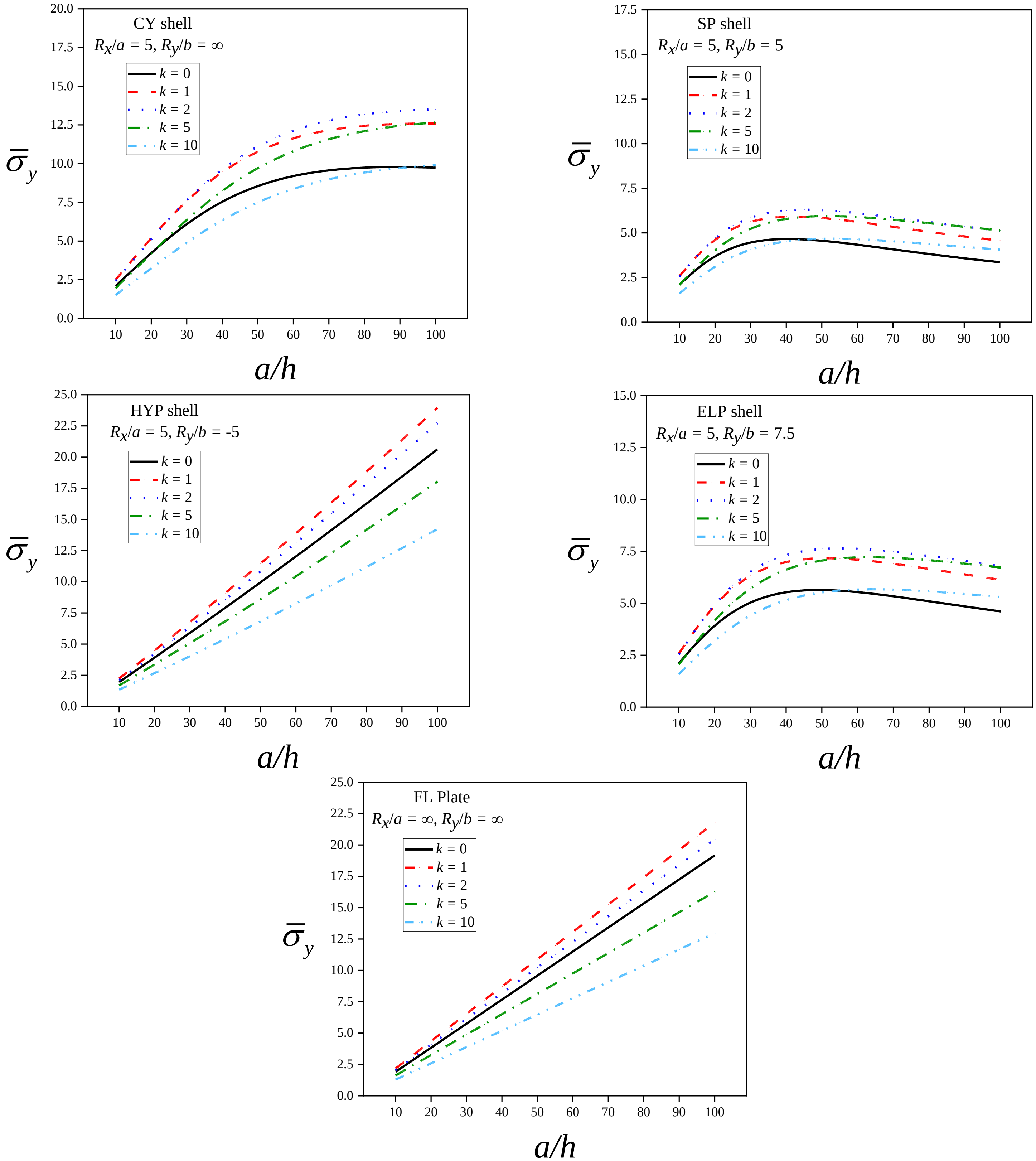

Figure 3.9 Normalized axial stress ($\bar{\sigma}_y$) versus side-to-thickness ratio (a/h) for FG (Al/Al_2O_3) DCSSs with various index (k) subjected to a uniform load. ($z = h/2$)

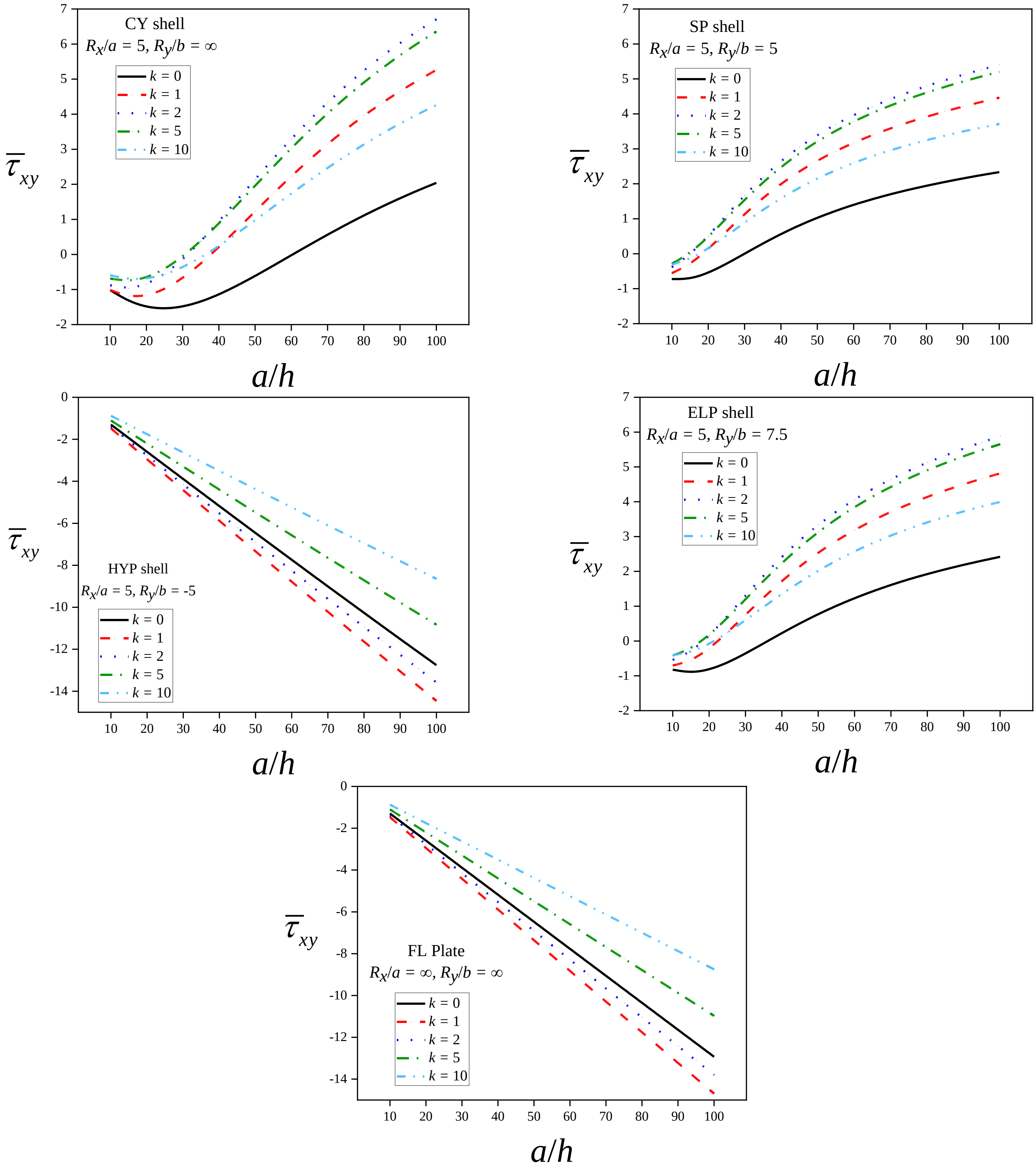

Figure 3.10 In-plane shear stress ($\bar{\tau}_{xy}$) versus side-to-thickness ratio (a/h) for FG (Al/Al_2O_3) DCSSs with various index (k) subjected to a uniform load. (z = - h/3)

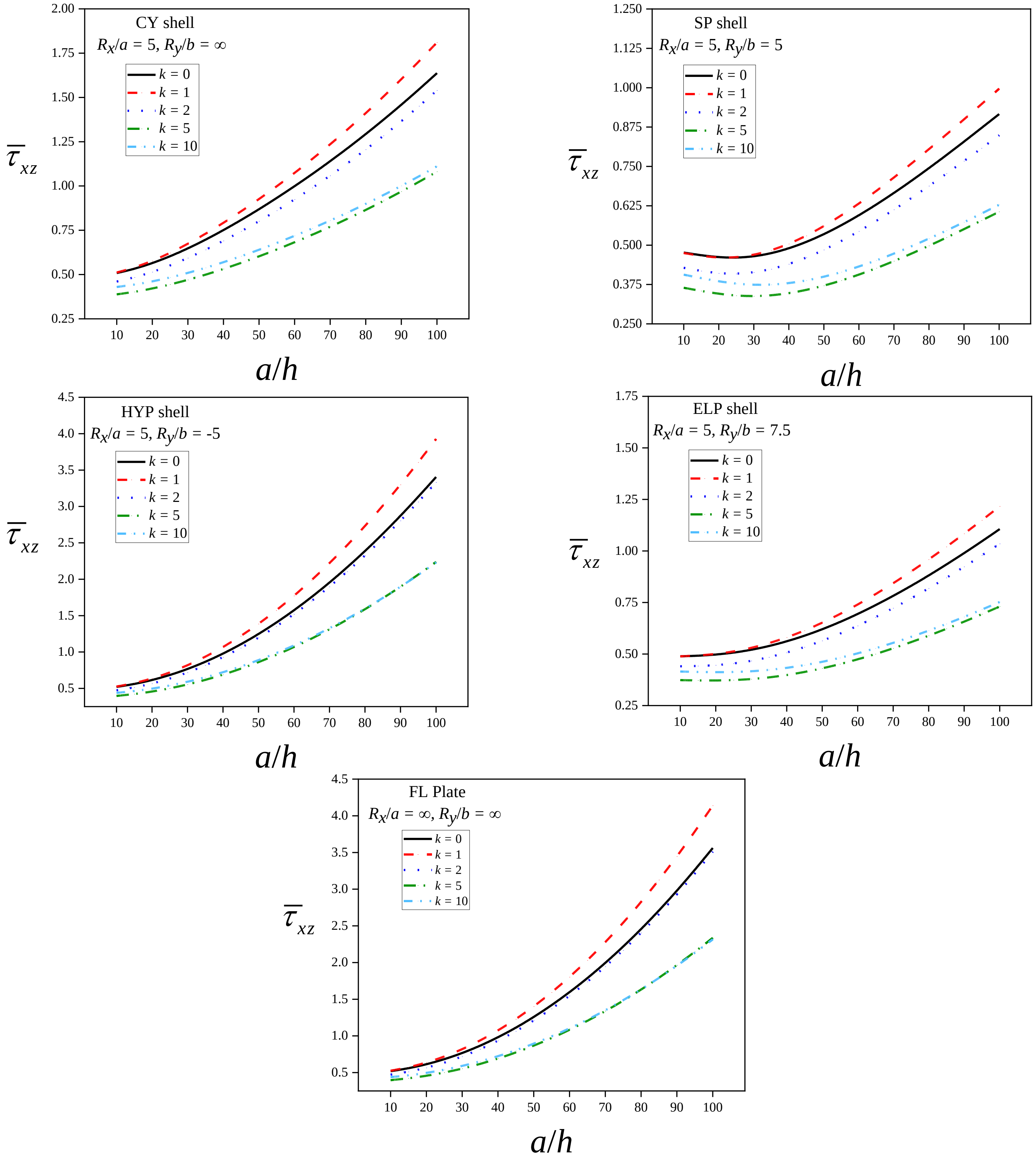

Figure 3.11 Out-plane shear stress ($\bar{\tau}_{xz}$) versus side-to-thickness ratio (a/h) for FG (Al/Al_2O_3) DCSSs with various index (k) subjected to a uniform load. (z = 0)

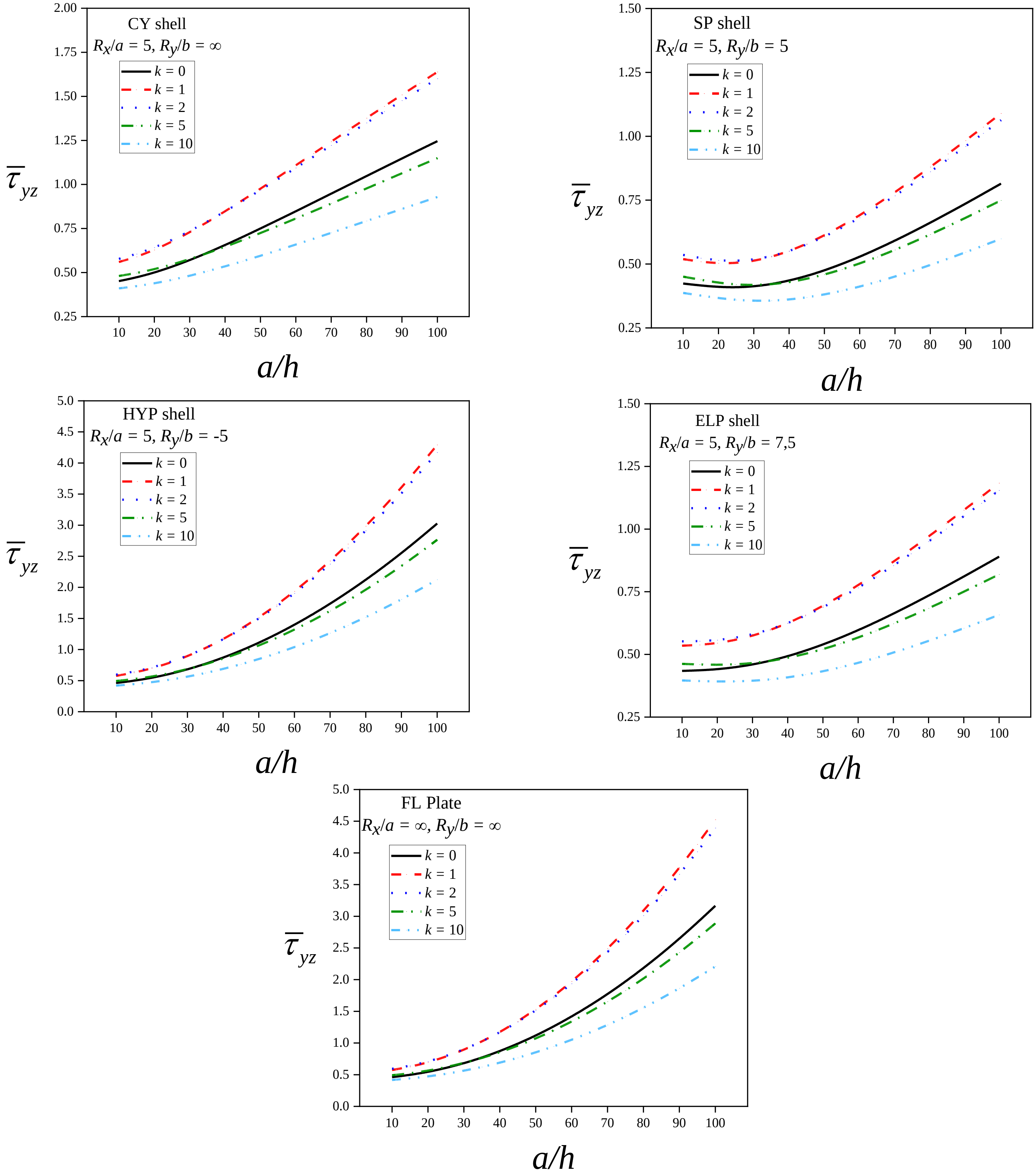

Figure 3.12 Out-plane shear stress ($\bar{\tau}_{yz}$) versus side-to-thickness ratio (a/h) for FG (Al/Al_2O_3) DCSSs with various index (k) subjected to a uniform load. ($z = h/6$)

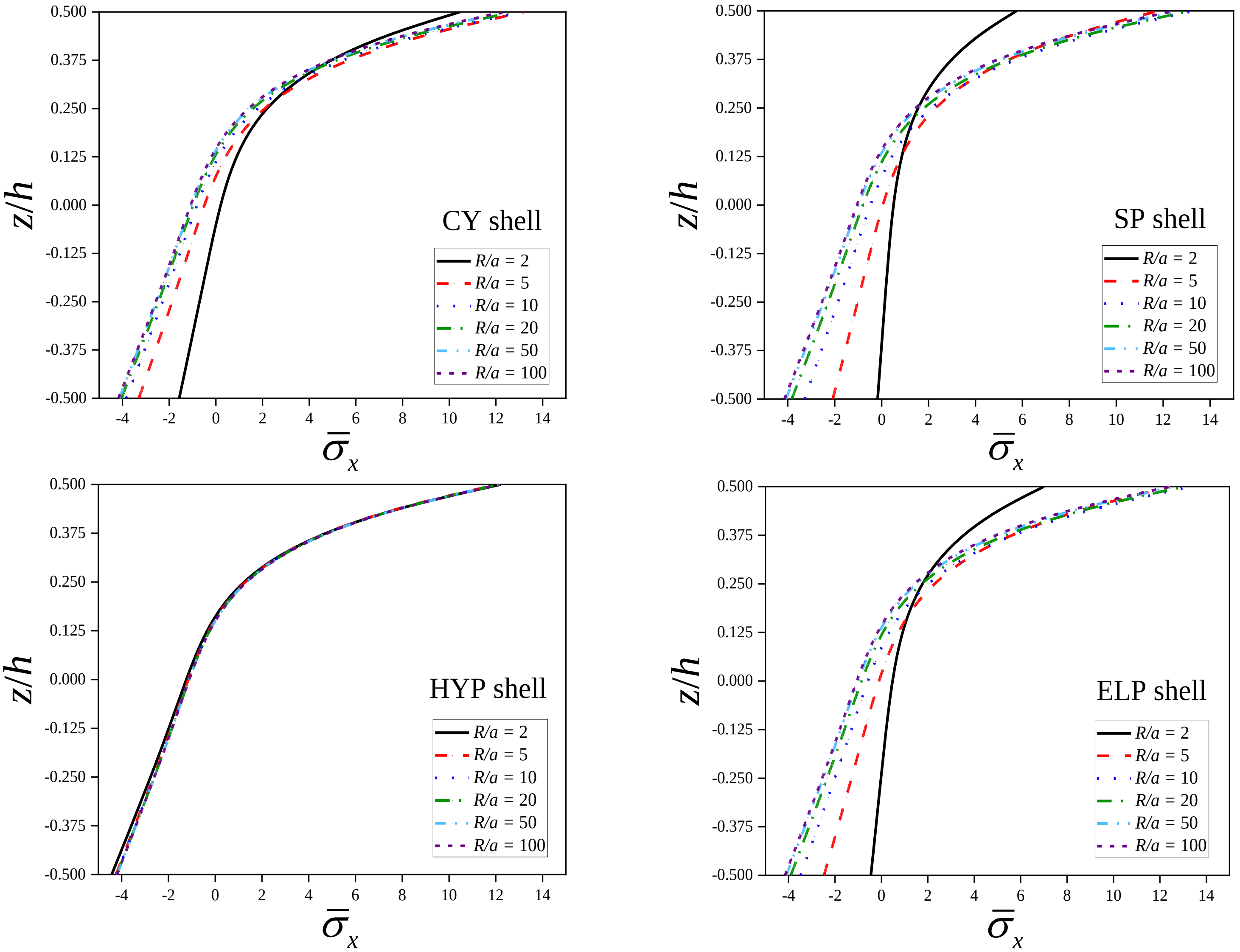

Figure 3.13 Through-thickness distributions of normalized axial stress ($\bar{\sigma}_x$) for FG (Al/Al_2O_3) DCSSs with different radius-to-length ratios (R/a) under a uniform load.

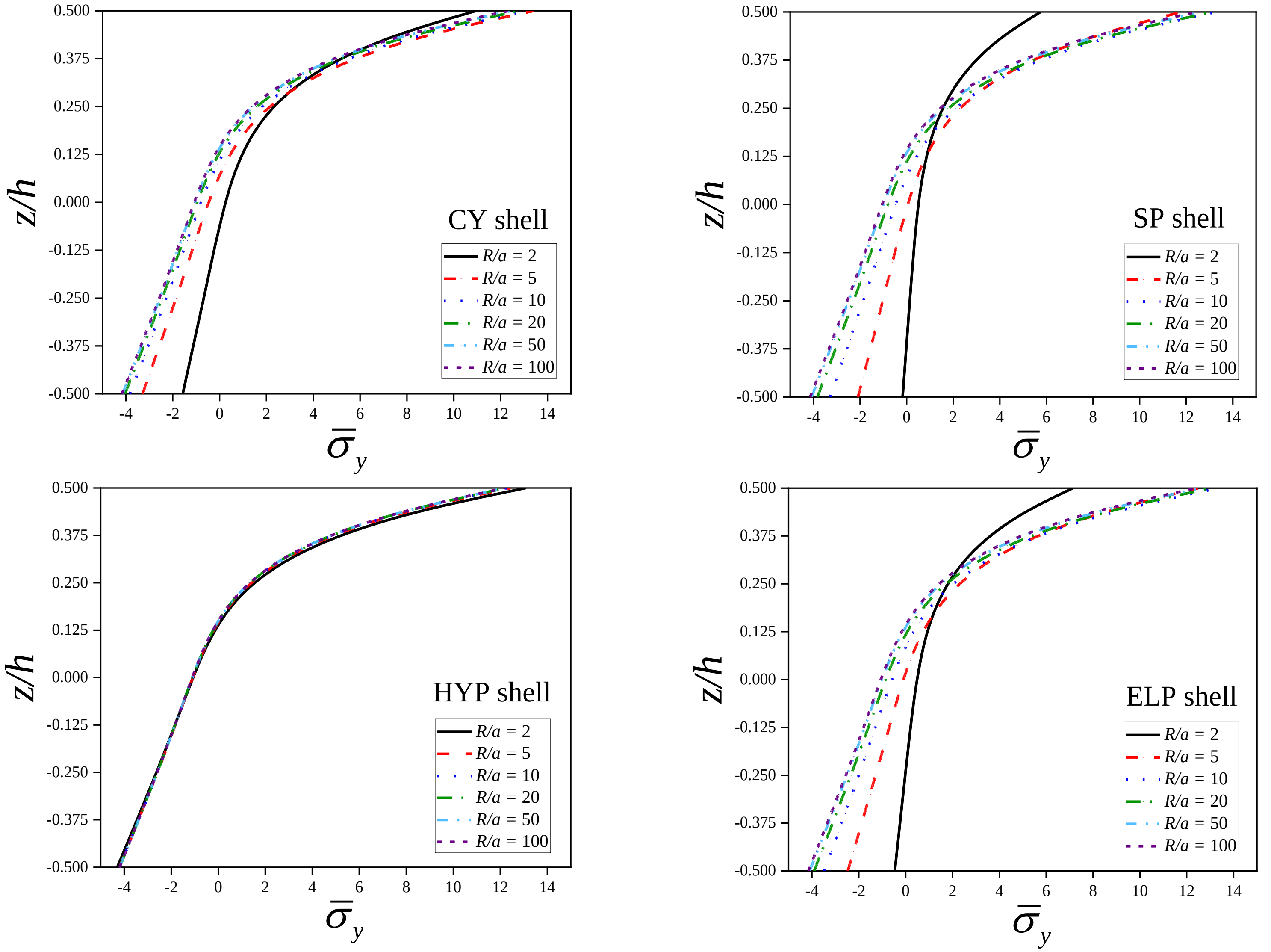

Figure 3.14 Through-thickness distributions of normalized axial stress ($\bar{\sigma}_y$) for FG (Al/Al_2O_3) DCSSs with different radius-to-length ratios (R/a) under a uniform load.

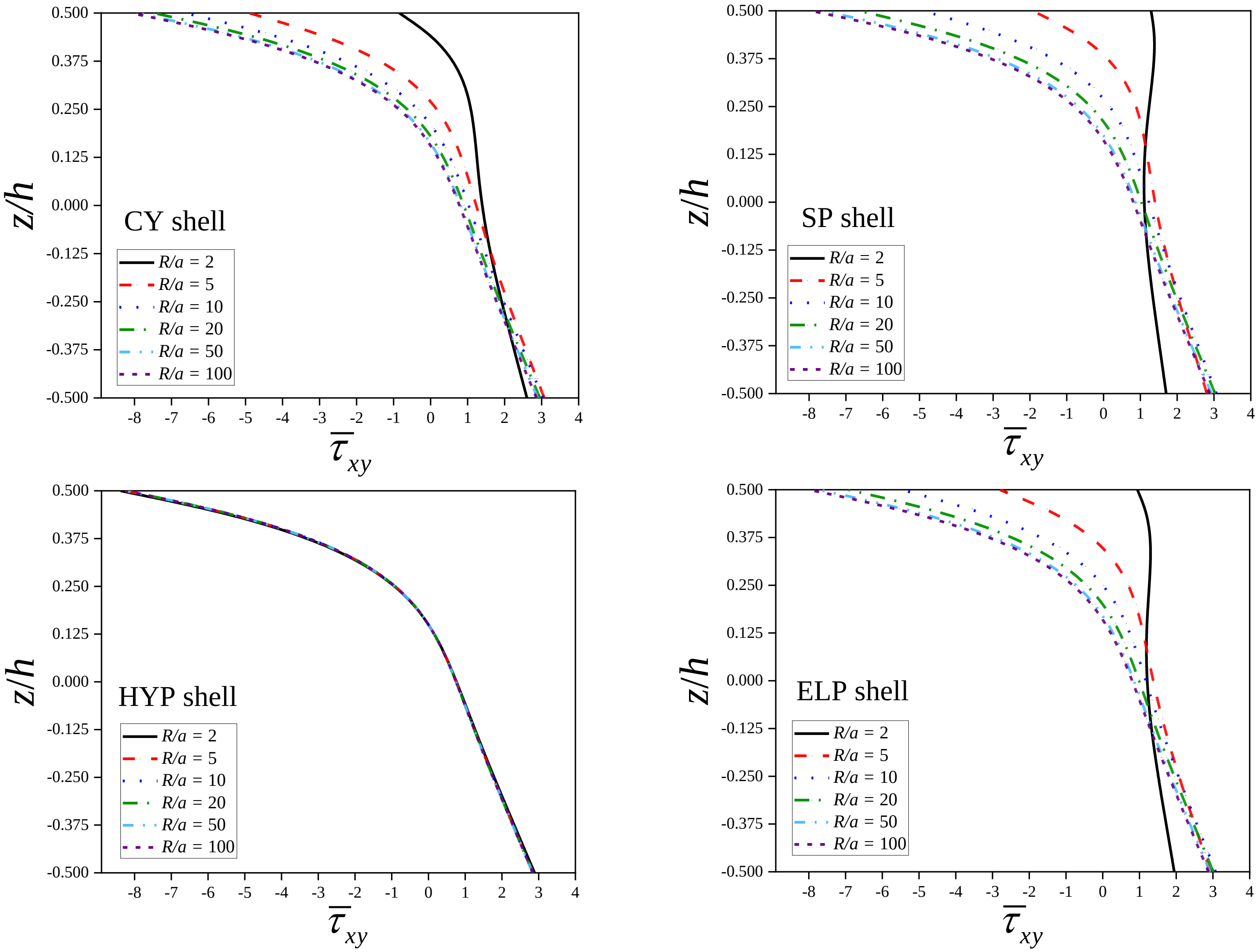

Figure 3.15 Through-thickness distributions of in-plane shear stress ($\bar{\tau}_{xy}$) for FG (Al/Al_2O_3) DCSSs with different radius-to-length ratios (R/a) under a uniform load.

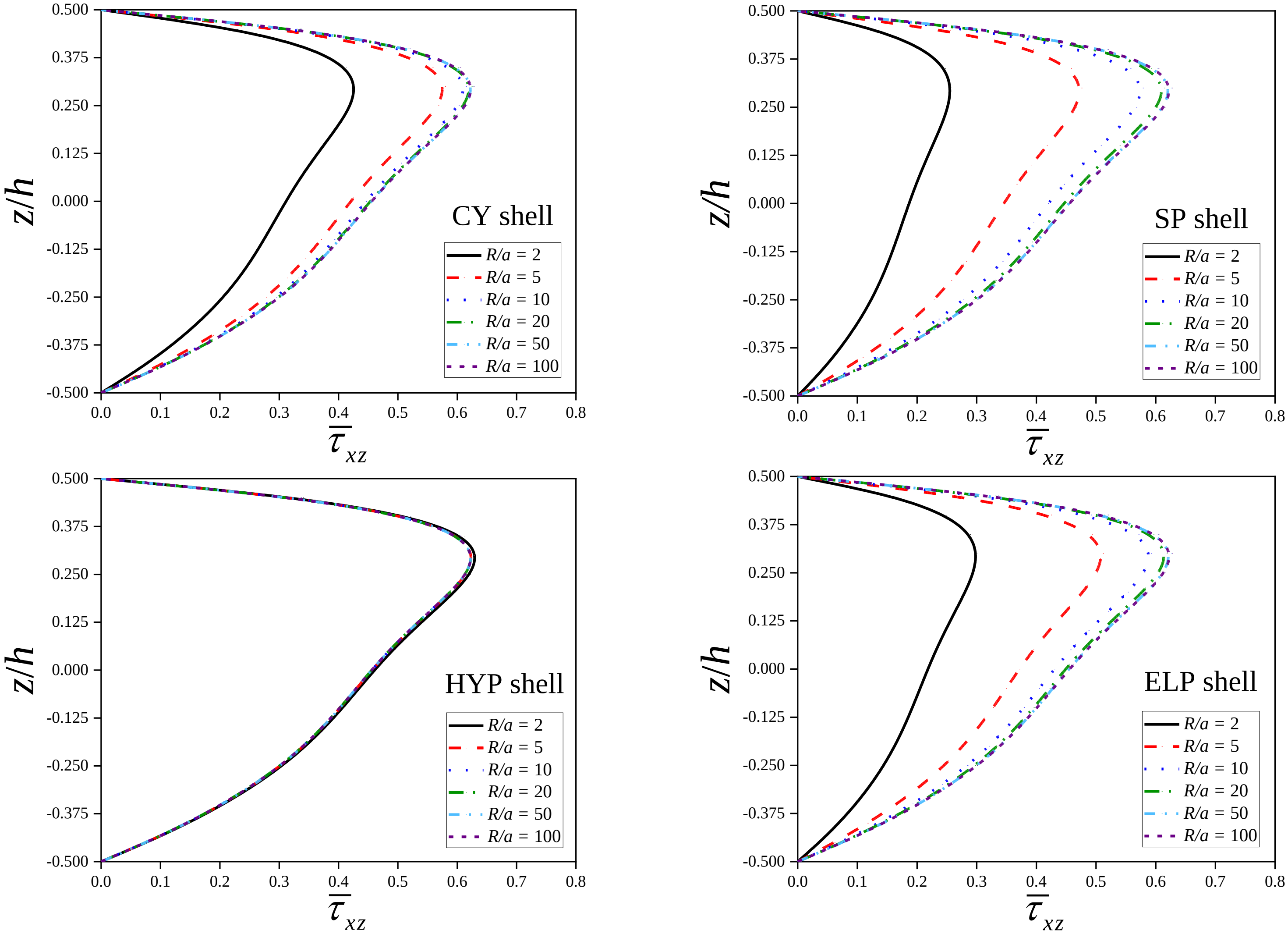

Figure 3.16 Through-thickness distributions of out-plane shear stress ($\bar{\tau}_{xz}$) for FG (Al/Al_2O_3) DCSSs with different radius-to-length ratios (R/a) under a uniform load.

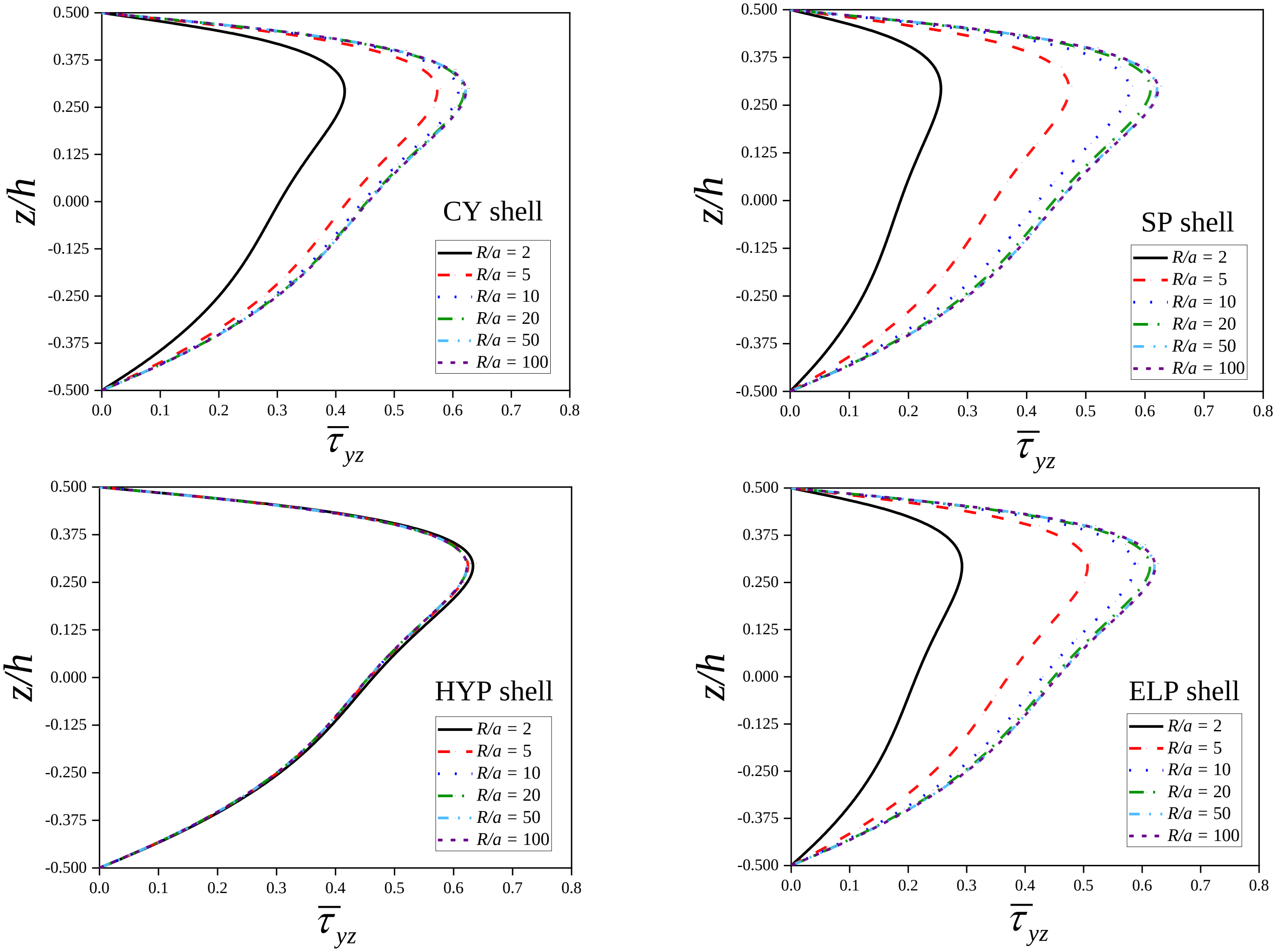

Figure 3.17 Through-thickness distributions of out-plane shear stress ($\bar{\tau}_{yz}$) for FG (Al/Al_2O_3) DCSSs with different radius-to-length ratios (R/a) under a uniform load.

3.4 Conclusion

This study presents a comprehensive investigation of the bending behavior of FG DCSSs using the IFSDT. Five types of shells are examined: CY shells, SP shells, HYP shells, ELP shells and FL plates. Key parameters such as power-law index (k), side-to-thickness ratio (a/h), radius-to-thickness ratio (R/h), radius-to-length ratio (R/a), boundary conditions, and loading types are analyzed with respect to their effects on transverse displacement, as well as normal and shear stress distributions. A convergence study demonstrates that the proposed FE model is both computationally efficient and stable, even at lower mesh densities. Comparisons with existing literature validate the accuracy of the model. Additionally, new findings—previously unreported—are introduced, contributing novel insights into the bending analysis of FG DCSSs. Key findings include:

- Shell deflections increase with a higher power-law index (k).
- For CY, SP, and ELP shells, an increase in the radius of curvature leads to higher DTD, whereas in HYP shells, displacements decrease.
- At large radii of curvature, displacements across all FG shell types tend to converge.
- Boundary conditions have a significant influence on bending behavior; shells with SSSS conditions exhibit the highest displacements, while those with CCCC show the lowest, under the same value of (k).
- Normal and shear stress distributions are highly dependent on the specific geometry of the FG shell.

This research introduces an innovative and efficient computational framework that empowers engineers and researchers to design and manufacture FG DCSSs with greater precision. By accurately predicting transverse displacements, along with normal and shear stress distributions, the proposed model lays a solid foundation for future advancements in the analysis and development of FG structures.

The following chapter will present a series of numerical examples to demonstrate the accuracy and efficiency of the proposed FE model in analyzing the vibrational response of various FG DCSSs.

Chapter 04

Free vibration analysis of FG DCSs: Results and discussion

Chapter 04

Free vibration analysis of FG DCSs: Results and discussion

4.1 Introduction

This chapter presents a comprehensive set of numerical results to validate the accuracy and efficiency of the proposed finite element model, SQ8-IFSDT, in analyzing the free vibration behavior of functionally graded doubly curved shallow shells (FG DCSSs). Five distinct shell geometries are considered: flat plates (FL), cylindrical shells (CY), spherical shells (SP), hyperbolic paraboloid shells (HYP), and elliptical shells (ELP). A convergence study is conducted to verify numerical stability, and results are benchmarked against established literature to confirm the model's reliability. Furthermore, a detailed parametric investigation is carried out to evaluate the influence of critical parameters—including the power-law index (k), side-to-thickness ratio (a/h), shell curvature, and boundary conditions—on the natural frequencies and mode shapes of FG DCSSs. **Table 4.1** presents the material properties employed in the study. **Table 4.2** and **Figure 4.1** illustrate the boundary conditions applied across all case scenarios.

For this study, the following relations for dimensionless fundamental frequency (DFF) are considered:

$$\bar{\omega} = \omega h(\rho_c/E_c) \quad ; \quad \bar{\bar{\omega}} = \omega a^2\sqrt{12\rho_m(1-\nu^2)/E_m h^2)} \tag{4.1}$$

Table 4.1 Material properties of FG DCSS considered in this work.

Properties	Ceramic					Metal	
	Si_3N_4	**SiC**	**$(Al_2O_3)1$**	**$(Al_2O_3)2$**	**ZrO_2**	**SUS304**	**Al**
$\boldsymbol{E}$ $(\boldsymbol{GPa})$	322.27	427	380	380	151	207.78	70
$\boldsymbol{\nu}$	0.24	0.17	0.3	0.3	0.3	0.318	0.3
$\boldsymbol{\rho}$ $(\boldsymbol{kg/m^3})$	2370	3100	3000	3800	3000	8166	2707

Table 4.2 The boundary conditions applied in the present work.

Boundary conditions	Abbreviations	Restrained edges
Simply supported	SSSS	$v_0 = w_0 = \phi_y = 0$ at x = 0 and x = a $u_0 = w_0 = \phi_x = 0$ at y = 0 and y = b
Clamped	CCCC	$u_0 = v_0 = w_0 = \phi_x = \phi_y = 0$ at x = 0 and x = a and y = 0 and y = b
Clamped-Simply supported	CSCS	$u_0 = w_0 = \phi_x = 0$ at y = 0 and y = b $u_0 = v_0 = w_0 = \phi_x = \phi_y = 0$ at x = 0 and x = a
Three edges Clamped and one Simply supported	CSCC	$u_0 = v_0 = w_0 = \phi_x = \phi_y = 0$ at x = 0 and x = a and y = b $u_0 = w_0 = \phi_x = 0$ at y = 0
Two edges Clamped and two opposite edges Free	CFCF	$u_0 = v_0 = w_0 = \phi_x = \phi_y = 0$ at x = 0 and x = a

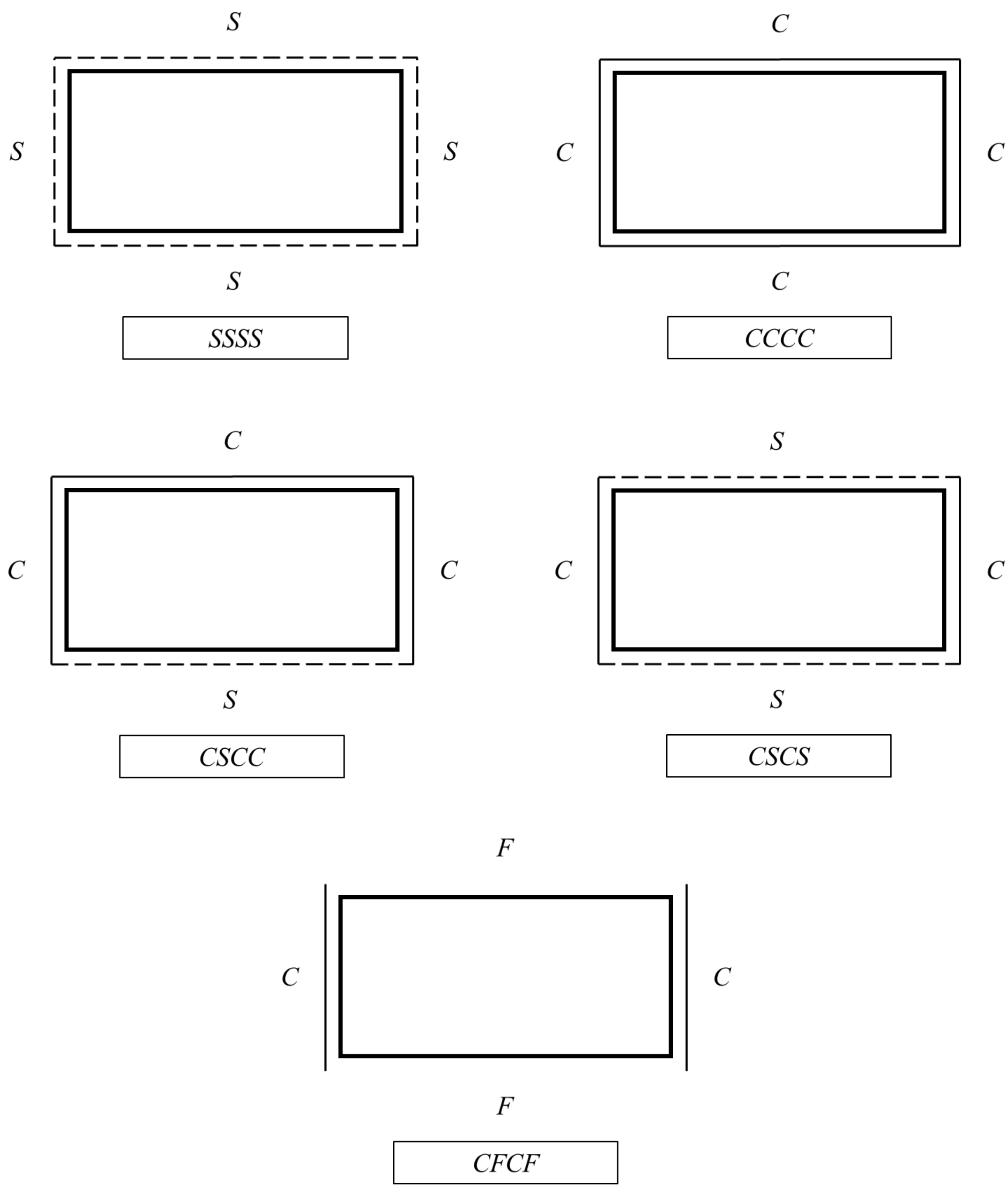

Figure 4.1 Applied boundary conditions for the numerical examples.

4.2 Convergence study

In this section, the convergence of the proposed FE model is investigated through the analysis of simply supported FG DCSSs made of (Al/Al_2O_3), with $a = b = 10h$. Various value of the power-law index (k = 0, 0.5, 1, 4, and 10) is considered. To validate the model, the numerical results are compared with those reported by:

- Matsunaga [302] utilized HSDT in conjunction with Navier's technique.
- Trinh and Kim [303] employed a three-variable refined shear deformation theory (TRSDT) using the Bubnov–Galerkin method.
- Alijani et al. [145] applied FSDT via the Galerkin method.
- Chorfi and Houmat [304] used FSDT, integrating the p-version of the FEM with the blending function approach.
- Van Vinh and Tounsi [196] implemented FSDT using Navier's method.

The numerical results for the DFFs demonstrate convergence with a 6×6 mesh and closely align with published results for all types of shells, as shown in **Table 4.3**. Therefore, it can be concluded that the current FE model is well suited for the free vibration analysis of FG DCSSs.

Table 4.3 Convergence of the DFFs (ϖ) of FG (Al/Al_2O_3) DCSSs.

Types of shell	Reference	Model	Power-law (*k*)				
			k **= 0**	***k*** **= 0.5**	***k*** **=1**	***k*** **= 4**	***k*** **= 10**
FL plate ($R_x/a = \infty$, $Ry/b = \infty$)	Present (2×2)	SQ8-IFSDT	0.0597	0.0509	0.0459	0.0393	0.0374
	Present (4×4)	SQ8-IFSDT	0.0577	0.0491	0.0442	0.0381	0.0364
	Present (6×6)	SQ8-IFSDT	0.0577	0.0490	0.0442	0.0381	0.0364
	Present (8×8)	SQ8-IFSDT	0.0577	0.0490	0.0442	0.0381	0.0364
	Present (10×10)	SQ8-IFSDT	0.0577	0.0490	0.0442	0.0381	0.0364
	Matsunaga [302]	HSDT	0.0588	0.0492	0.0430	0.0381	0.0364
	Trinh and Kim [303]	TRSDT	0.0577	0.0490	0.0442	0.0381	0.0364
	Alijani et al. [145]	FSDT	0.0597	0.0506	0.0456	0.0396	0.0380
	Chorfi and Houmat [304]	P-FEM	0.0577	0.0490	0.0442	0.0383	0.0366
	Van Vinh and Tounsi [196]	FSDT	0.0577	0.0490	0.0442	0.0382	0.0366
CY shell ($R_x/a = 2$, $R_y/b = \infty$)	Present (2×2)	SQ8-IFSDT	0.0637	0.0546	0.0494	0.0418	0.0394
	Present (4×4)	SQ8-IFSDT	0.0617	0.0528	0.0477	0.0406	0.0383
	Present (6×6)	SQ8-IFSDT	0.0617	0.0527	0.0477	0.0406	0.0383
	Present (8×8)	SQ8-IFSDT	0.0617	0.0527	0.0477	0.0405	0.0383
	Present (10×10)	SQ8-IFSDT	0.0617	0.0527	0.0477	0.0405	0.0383
	Matsunaga [302]	HSDT	0.0622	0.0535	0.0485	0.0413	0.0390
	Trinh and Kim [303]	TRSDT	0.0628	0.0538	0.0488	0.0416	0.0392
	Alijani et al. [145]	FSDT	0.0648	0.0553	0.0501	0.0430	0.0408
	Chorfi and Houmat [304]	P-FEM	0.0629	0.0540	0.0490	0.0419	0.0395
	Van Vinh and Tounsi [196]	FSDT	0.0617	0.0527	0.0477	0.0407	0.0385
SP shell ($R_x/a = 2$, $R_y/b = 2$)	Present (2×2)	SQ8-IFSDT	0.0764	0.0662	0.0603	0.0501	0.0463
	Present (4×4)	SQ8-IFSDT	0.0746	0.0646	0.0589	0.0490	0.0454
	Present (6×6)	SQ8-IFSDT	0.0746	0.0646	0.0588	0.0490	0.0454
	Present (8×8)	SQ8-IFSDT	0.0746	0.0646	0.0588	0.0490	0.0453
	Present (10×10)	SQ8-IFSDT	0.0746	0.0646	0.0588	0.0490	0.0453
	Matsunaga [302]	HSDT	0.0751	0.0657	0.0601	0.0503	0.0464
	Trinh and Kim [303]	TRSDT	0.0761	0.0662	0.0605	0.0506	0.0467
	Alijani et al. [145]	FSDT	0.0779	0.0676	0.0617	0.0519	0.0482
	Chorfi and Houmat [304]	P-FEM	0.0762	0.0664	0.0607	0.0509	0.0471
	Van Vinh and Tounsi [196]	FSDT	0.0746	0.0646	0.0588	0.0490	0.0455
HYP shell ($R_x/a = 2$, $R_y/b = -2$)	Present (2×2)	SQ8-IFSDT	0.0574	0.0490	0.0443	0.0378	0.0359
	Present (4×4)	SQ8-IFSDT	0.0548	0.0466	0.0420	0.0362	0.0346
	Present (6×6)	SQ8-IFSDT	0.0548	0.0466	0.0420	0.0362	0.0345
	Present (8×8)	SQ8-IFSDT	0.0548	0.0466	0.0420	0.0362	0.0345
	Present (10×10)	SQ8-IFSDT	0.0548	0.0466	0.0420	0.0362	0.0345
	Matsunaga [302]	HSDT	0.0563	0.0479	0.0432	0.0372	0.0355
	Trinh and Kim [303]	TRSDT	0.0577	0.0490	0.0442	0.0381	0.0364
	Alijani et al. [145]	FSDT	0.0597	0.0506	0.0456	0.0396	0.0380
	Chorfi and Houmat [304]	P-FEM	0.0580	0.0493	0.0445	0.0385	0.0368
	Van Vinh and Tounsi [196]	FSDT	0.0548	0.0465	0.0420	0.0363	0.0347
ELP Shell ($R_x/a = 2$, $R_y/b = 4/3$)	Present (2×2)	SQ8-IFSDT	0.0839	0.0731	0.0668	0.0550	0.0504
	Present (4×4)	SQ8-IFSDT	0.0822	0.0716	0.0653	0.0540	0.0495
	Present (6×6)	SQ8-IFSDT	0.0821	0.0715	0.0653	0.0540	0.0495
	Present (8×8)	SQ8-IFSDT	0.0821	0.0715	0.0653	0.0540	0.0495
	Present (10×10)	SQ8-IFSDT	0.0821	0.0715	0.0653	0.0540	0.0495

4.3 Parameter study

Example 1:

Table 4.4 presents the analyses of natural frequencies of clamped FG (Si_3N_4/SUS304) CY panels with different power-law index (*k*) for *a*/*h* =10 and *R*/*a* =10. The results obtained are compared with the findings of Neves et al. [305], who used radial basis functions collocation based on HSDT, and Pradyumna and Bandyopadhyay [249], who applied the Q8-FE model also based on HSDT. The comparisons indicate strong agreement between the present results and the reference data across all evaluated modes, validating the accuracy of the FE model. Therefore, this model is suitable for studying the vibration characteristics of FG shells across different power-law index (*k*).

Table 4.4 The first four DFFs ($\bar{\bar{\omega}}$) of clamped FG (Si_3N_4/SUS304) CY panels for various power-law index (*k*).

Mode	Reference	Model	Power-law (*k*)				
			***k* = 0**	***k* = 0.2**	***k* = 2**	***k* = 10**	***k* = ∞**
1	Present	SQ8-IFSDT	74.2064	60.3690	40.4269	34.9922	32.5926
	Neves et al. [305]	HSDT	74.2634	60.0061	40.5259	35.1663	32.6108
	Pradyumna and Bandyopadhyay [249]	Q8-HSDT	72.9613	60.0269	39.1457	33.3666	32.0274
2	Present	SQ8-IFSDT	141.5267	115.0536	76.7531	66.2729	61.8705
	Neves et al. [305]	HSDT	141.6779	114.3788	76.9725	66.6482	61.9329
	Pradyumna and Bandyopadhyay [249]	Q8-HSDT	138.5552	113.8806	74.2915	63.2869	60.5546
3	Present	SQ8-IFSDT	141.6957	115.2227	76.8629	66.3558	61.9450
	Neves et al. [305]	HSDT	141.8485	114.5495	77.0818	66.7332	62.0082
	Pradyumna and Bandyopadhyay [249]	Q8-HSDT	138.5552	114.0266	74.3868	63.3668	60.6302
4	Present	SQ8-IFSDT	198.8302	161.6120	107.5698	92.7290	86.6707
	Neves et al. [305]	HSDT	199.1566	160.7355	107.9484	93.3350	86.8160
	Pradyumna and Bandyopadhyay [249]	Q8-HSDT	195.5366	160.6235	104.7687	89.1970	85.1788

Example 2:

Table 4.5 presents the natural frequencies of FG DCSSs is analyzed under various boundary conditions, with *a*/*h* =10 and *k* = 2. Five types of curved shells, including FL plates, CY, SP, HYP, and ELP shells are considered. A comparison is provided of the first five DFFs of FG (SUS304/Si_3N_4) CY shells with Zhao et al. [167]. The outcomes demonstrate a strong agreement with Zhao et al. [167] across all boundary conditions. Moreover, the natural frequencies are observed to increase significantly with higher vibration modes for all shell types.

From **Table 4.5** and **Figure 4.2**, the CCCC FG shells have the highest frequencies among all curved shells, while the CFCF shells exhibit the lowest frequencies. The first six displacement modes of FG (SUS304/Si_3N_4) CY shells are illustrated in **Figure 4.3**. The mode shapes for SSSS, CCCC, CSCS, and CFCF are symmetric, while those for CSCC are asymmetric. This highlights the critical impact of boundary conditions on the mode shapes.

Table 4.5 First five DFFs ($\bar{\bar{\omega}}$) of FG (SUS304/Si_3N_4) DCSSs for different boundary conditions.

Types of shell	Mode	Reference	Model	BCs				
				SSSS	**CSCC**	**CSCS**	**CCCC**	**CFCF**
FL plate ($R_x/a = \infty$, $Ry/b = \infty$)	1	Present	SQ8-IFSDT	23.6528	36.1157	33.0657	40.3181	25.6117
	2	Present	SQ8-IFSDT	56.3989	68.5756	60.8808	76.8625	29.8642
	3	Present	SQ8-IFSDT	56.3989	74.9086	73.3684	76.8625	47.8664
	4	Present	SQ8-IFSDT	79.9682	102.377	79.9682	107.662	65.3604
	5	Present	SQ8-IFSDT	79.9682	102.699	97.6193	126.939	70.8242
CY shell ($R_x/a = 10$, $R_y/b = \infty$)	1	Present	SQ8-IFSDT	23.6530	36.1374	33.1990	40.4269	25.8319
		Zhao et al. [167]	FSDT	-	36.0330	32.8530	40.1870	-
	2	Present	SQ8-IFSDT	56.3037	68.4821	60.8931	76.7531	30.0553
		Zhao et al. [167]	FSDT	-	68.4820	60.6470	76.8230	-
	3	Present	SQ8-IFSDT	56.3797	74.8902	73.2617	76.8629	47.9460
		Zhao et al. [167]	FSDT	-	74.8440	73.4110	76.885	-
	4	Present	SQ8-IFSDT	79.9682	102.277	79.9682	107.569	65.2262
		Zhao et al. [167]	FSDT	-	101.793	79.3530	107.423	-
	5	Present	SQ8-IFSDT	80.0652	102.864	97.5338	126.830	70.7460
		Zhao et al. [167]	FSDT	-	102.163	97.3290	127.835	-
SP shell ($R_x/a = 10$, $R_y/b = 10$)	1	Present	SQ8-IFSDT	23.8382	36.3165	33.2451	40.6112	25.8767
	2	Present	SQ8-IFSDT	56.3361	68.5064	60.8194	76.7678	30.0608
	3	Present	SQ8-IFSDT	56.3361	74.8125	73.2722	76.7678	47.9017
	4	Present	SQ8-IFSDT	80.0652	102.225	80.0652	107.511	65.2350
	5	Present	SQ8-IFSDT	80.0652	102.864	97.4671	126.723	70.7563
HYP shell ($R_x/a = 10$, $R_y/b = -10$)	1	Present	SQ8-IFSDT	23.6033	36.3027	33.2647	40.5551	25.8690
	2	Present	SQ8-IFSDT	56.3947	68.6470	60.9521	76.9071	30.0583
	3	Present	SQ8-IFSDT	56.435	74.9483	73.3729	76.9432	47.9936
	4	Present	SQ8-IFSDT	79.8713	102.366	79.8713	107.661	65.2964
	5	Present	SQ8-IFSDT	80.0652	102.861	97.6098	126.981	70.7503
ELP Shell ($R_x/a = 10$, $R_y/b = 15$)	1	Present	SQ8-IFSDT	23.9803	36.5336	33.2173	40.8192	25.9296
	2	Present	SQ8-IFSDT	56.3037	68.5892	60.8456	76.7148	30.0668
	3	Present	SQ8-IFSDT	56.4136	74.7666	73.2552	76.8382	47.8808
	4	Present	SQ8-IFSDT	80.0652	102.212	80.0329	107.494	65.2690
	5	Present	SQ8-IFSDT	80.1139	102.863	97.4883	126.682	70.7669

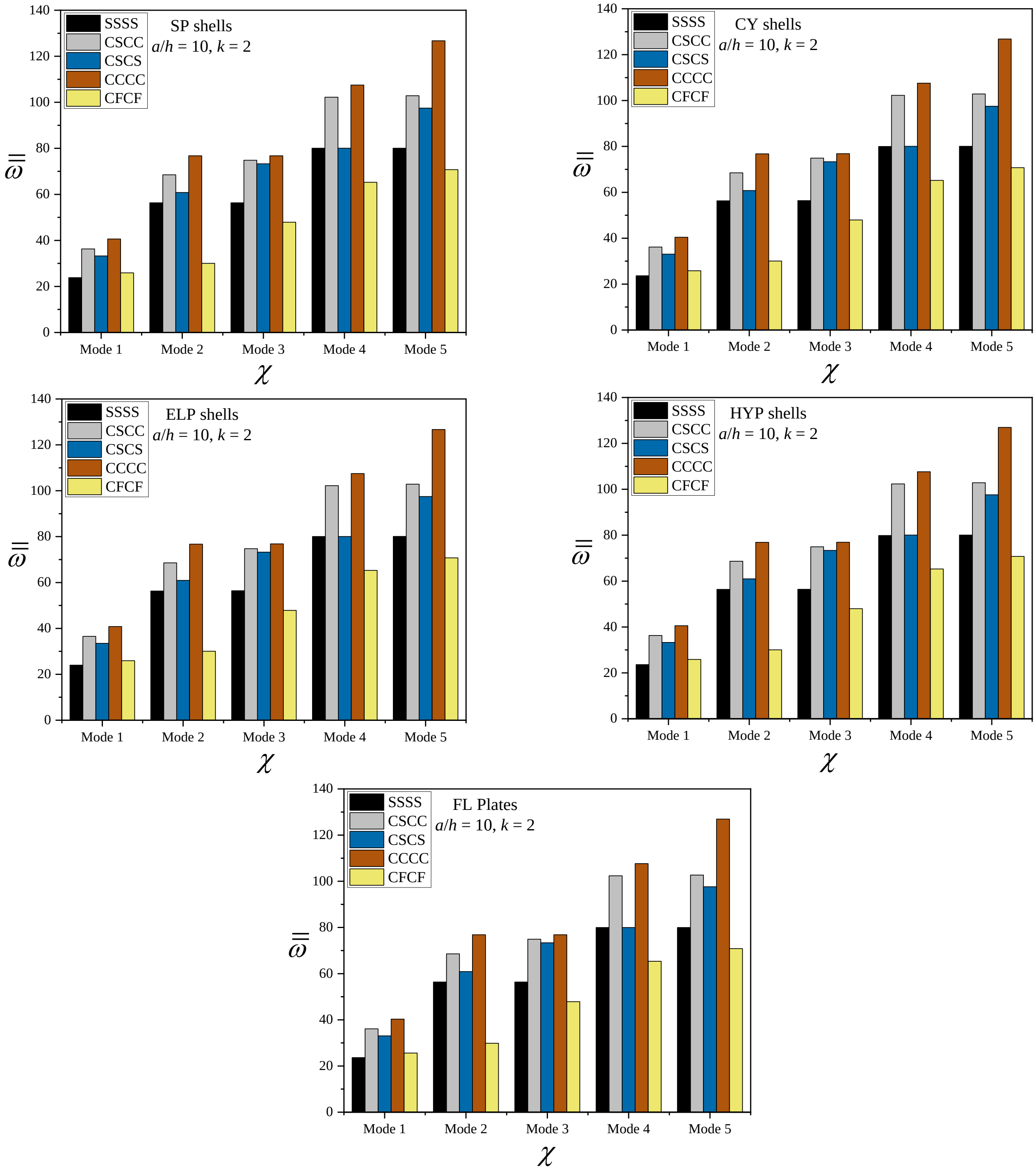

Figure 4.2 The first five DFFs of FG (SUS304/Si_3N_4) DCSSs with different boundary conditions.

SSSS

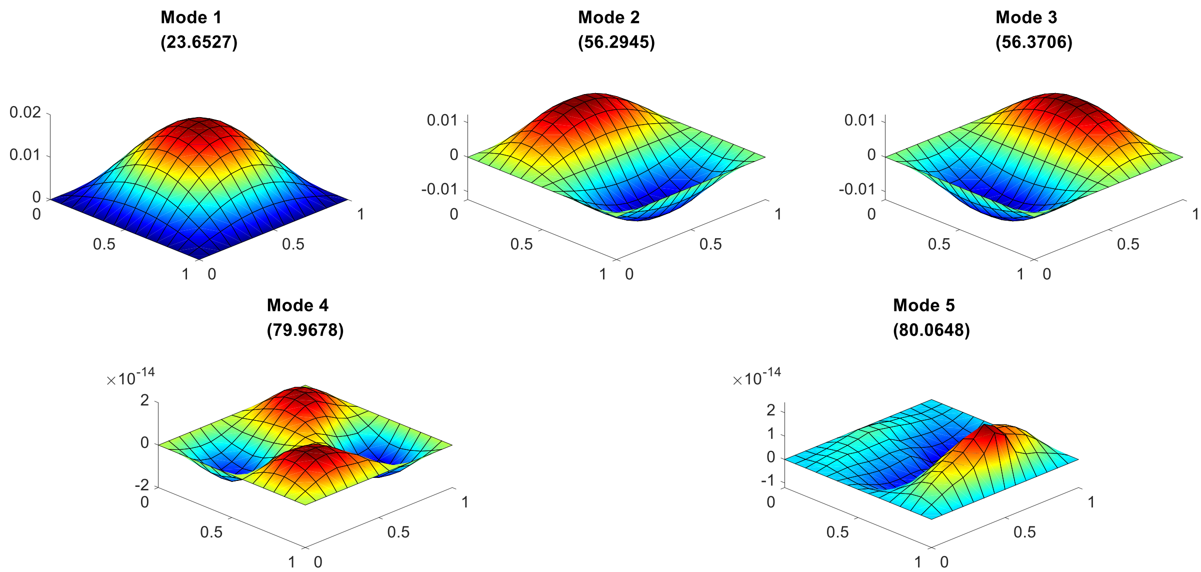
Mode 1
(23.6527)
Mode 2
(56.2945)
Mode 3
(56.3706)
Mode 4
(79.9678)
Mode 5
(80.0648)

CSCC

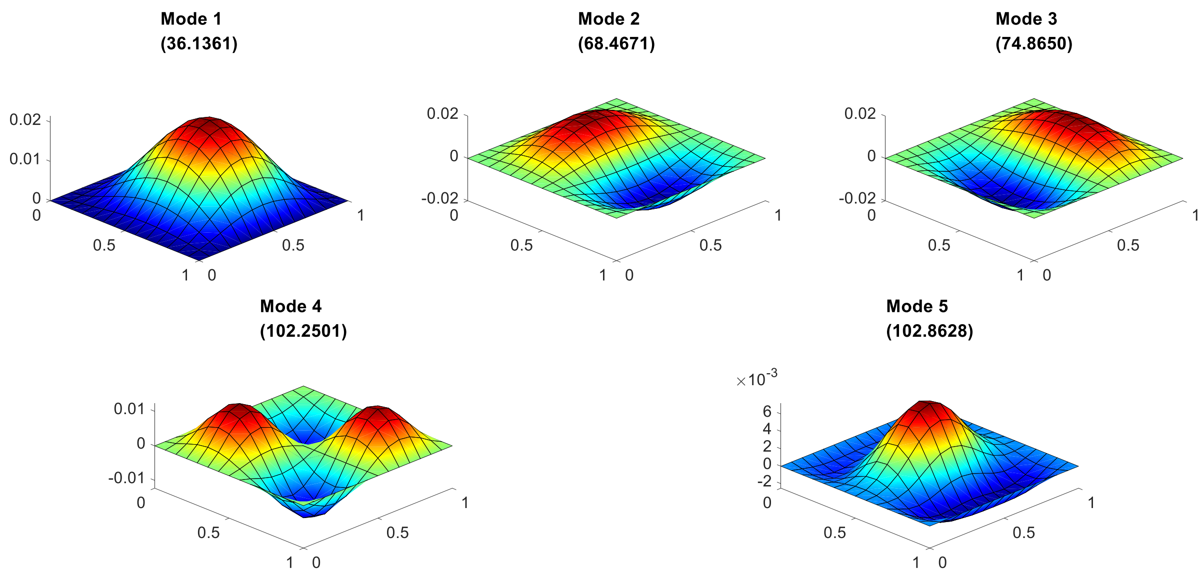
Mode 1
(36.1361)
Mode 2
(68.4671)
Mode 3
(74.8650)
Mode 4
(102.2501)
Mode 5
(102.8628)

CSCS

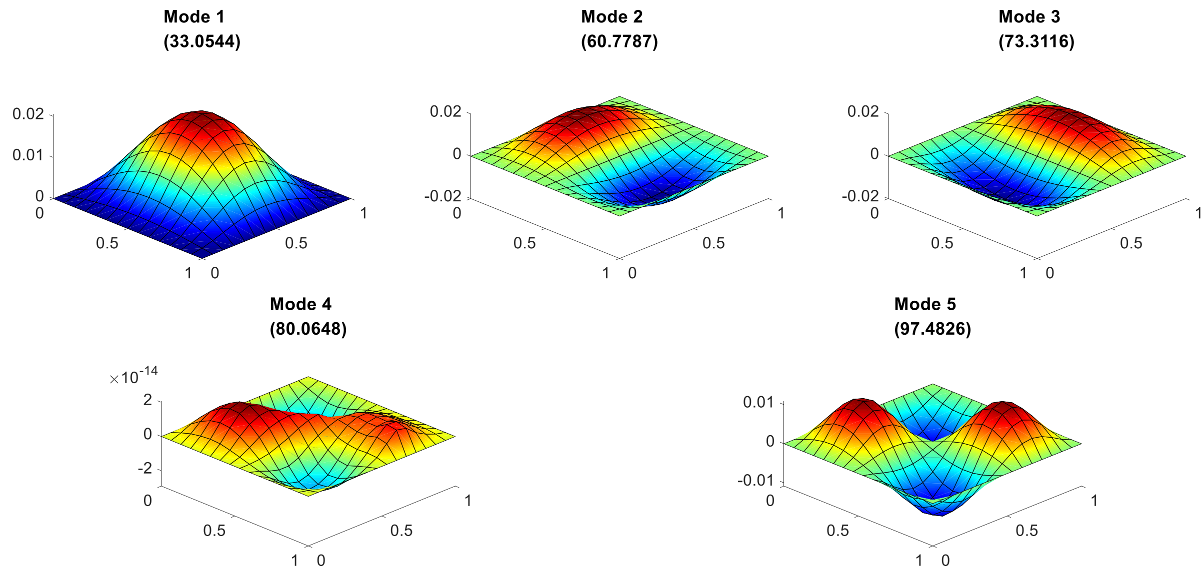
Mode 1
(33.0544)
Mode 2
(60.7787)
Mode 3
(73.3116)
Mode 4
(80.0648)
Mode 5
(97.4826)

CCCC

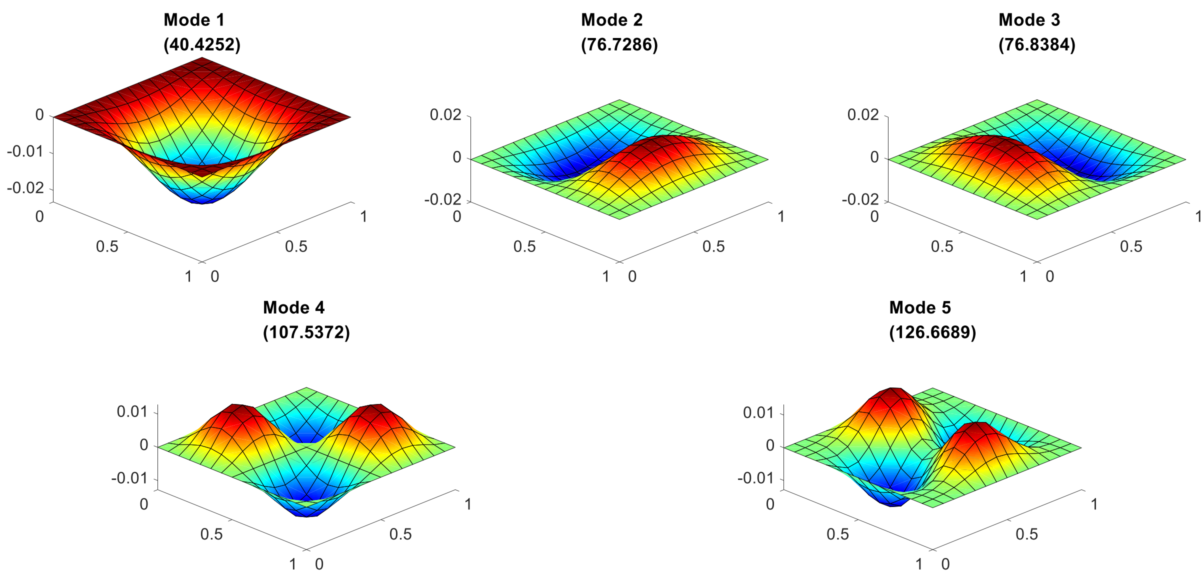
Mode 1
(40.4252)
Mode 2
(76.7286)
Mode 3
(76.8384)
Mode 4
(107.5372)
Mode 5
(126.6689)

CFCF

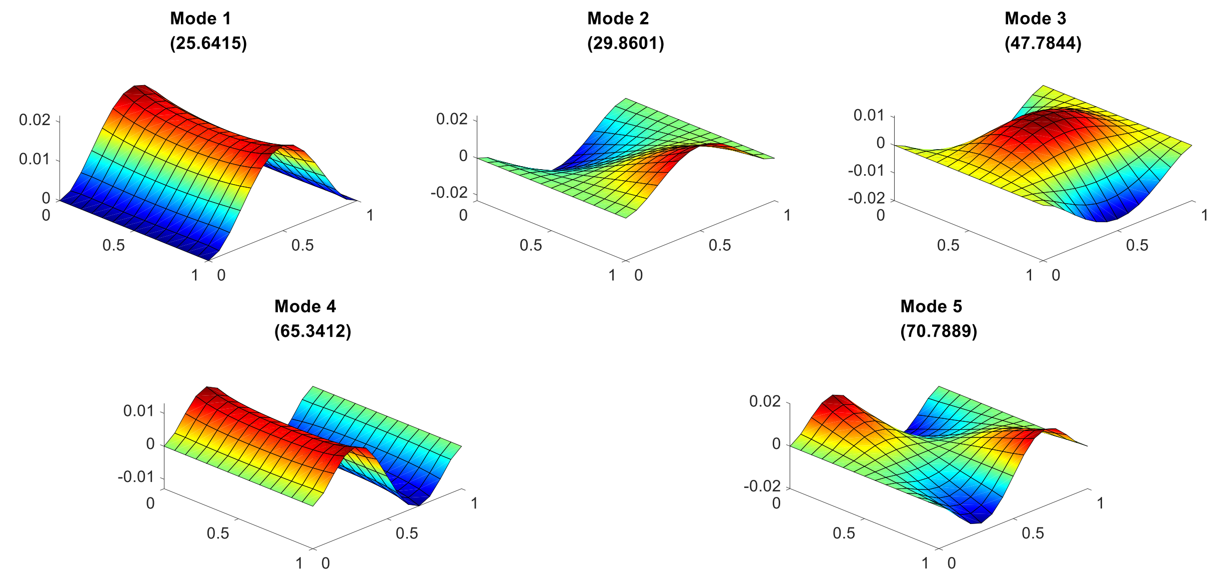

Figure 4.3 The first five mode shapes of FG (SUS304/Si_3N_4) CY shells under different boundary conditions.

Example 3:

The DFFs ($\bar{\bar{\omega}}$) of FG (Al/Al_2O_3) CY and SP shells with different radius-to-length ratios (R/a) are provided in **Tables 4.6** and **4.7**, respectively. The results are calculated for various values of the power-law index (k = 0, 0.2, 0.5, 1, 2, 10, and ∞), a range of radius-to-length ratios (R/a = 0.5, 1, 5, 10, 50, and ∞), and two types of boundary conditions (SSSS and CCCC). These results are compared with existing data, including the analytical solution from Neves et al. [305] and the FEM-Q8 solution from Pradyumna and Bandyopadhyay [249]. The comparison reveals a strong alignment between the findings, affirming the accuracy of the present FE model, SQ8-IFSDT, as opposed to the HSDTs used by Neves et al. [305] and Pradyumna and Bandyopadhyay [249].

The tables further illustrate that the DFFs of FG CY and SP shells decrease as the radius-to-length ratio (R/a) increases. Generally, FG (Al/Al_2O_3) SP shells exhibit higher frequencies than FG (Al/Al_2O_3) CY shells with equivalent R/a values. When R/a ratio approaches ∞, both CY and SP shells behave like flat plates with similar frequencies, establishing the flat plate frequencies as a limiting case for FG (Al/Al_2O_3) CY and SP shells. **Figures 4.4** illustrate the DFFs variations of FG (Al/Al_2O_3) CY and SP shells as a function of the R/a ratio under SSSS and CCCC boundary conditions. As the R/a ratio increases from 0.5 to 5, the frequencies drop sharply at first and then gradually stabilize at lower values.

Additionally, an increase in the index (k) results in lower frequencies for FG (Al/Al_2O_3) shells. This is due to the corresponding increase in the metal volume fraction and decrease in the ceramic volume fraction, which reduces the shells' stiffness. Homogeneous ceramic shells display the highest frequencies, while homogeneous metal shells have the lowest. **Figure 4.4** further shows that CCCC shells consistently have higher frequencies than SSSS shells.

Table 4.6 The effects of power-law index (k) on the DFFs ($\bar{\bar{\omega}}$) of FG (Al/Al_2O_3) CY shells for different radius-to-length ratios (R/a).

k	**BCs**	**References**	**Models**	***R/a***					
				***R/a* = 0.5**	***R/a* = 1**	***R/a* = 5**	***R/a* = 10**	***R/a* = 50**	**Plate**
0	SSSS	Present	SQ8-IFSDT	70.2768	52.3676	42.6816	42.3181	42.2008	42.1959
		Neves et al. [305]	HSDT	70.1594	52.1938	42.6701	42.3153	42.2008	42.1961
		Pradyumna and Bandyopadhyay [249]	Q8-HSDT	68.8645	51.5216	42.2543	41.9080	41.7963	41.7917
	CCCC	Present	SQ8-IFSDT	132.9793	95.6351	73.1096	72.2699	71.9989	71.9876
		Neves et al. [305]	HSDT	133.6037	95.5849	73.1640	72.3304	72.0614	72.0502
		Pradyumna and Bandyopadhyay [249]	Q8-HSDT	129.9808	94.4973	71.8861	71.0394	70.7660	70.7546
0.2	SSSS	Present	SQ8-IFSDT	65.4511	48.3040	39.0263	38.6865	38.5837	38.5817
		Neves et al. [305]	HSDT	65.3889	47.9338	38.7168	38.3840	38.2842	38.2827
		Pradyumna and Bandyopadhyay [249]	Q8-HSDT	64.4001	47.5968	40.1621	39.8472	39.7465	39.7426
	CCCC	Present	SQ8-IFSDT	122.1349	88.4132	67.1132	66.3258	66.0791	66.0714
		Neves et al. [305]	HSDT	121.8612	87.8148	66.6620	65.8808	65.6371	65.6299
		Pradyumna and Bandyopadhyay [249]	Q8-HSDT	119.6109	87.3930	68.1152	67.3320	67.0801	67.0698
0.5	SSSS	Present	SQ8-IFSDT	60.1472	43.8757	35.0463	34.7303	34.6411	34.6419
		Neves et al. [305]	HSDT	60.4255	43.6883	34.8768	34.5672	34.4809	34.4820
		Pradyumna and Bandyopadhyay [249]	Q8-HSDT	59.4396	43.3019	37.2870	36.9995	36.9088	36.9057
	CCCC	Present	SQ8-IFSDT	110.1514	80.4596	60.4870	59.7537	59.5311	59.5268
		Neves et al. [305]	HSDT	110.2017	80.0146	60.2477	59.5215	59.3022	59.2985
		Pradyumna and Bandyopadhyay [249]	Q8-HSDT	108.1546	79.5689	63.1896	62.4687	62.2380	62.2291
1	SSSS	Present	SQ8-IFSDT	54.3333	39.2196	31.0007	30.7130	30.6377	30.6407
		Neves et al. [305]	HSDT	54.8909	39.1753	30.9306	30.6485	30.5759	30.5792
		Pradyumna and Bandyopadhyay [249]	Q8-HSDT	53.9296	38.7715	33.2268	32.9585	32.8750	32.8726
	CCCC	Present	SQ8-IFSDT	97.5381	71.9929	53.6108	52.9399	52.7427	52.7413
		Neves et al. [305]	HSDT	97.9069	71.6716	53.5430	52.8800	52.6864	52.6856
		Pradyumna and Bandyopadhyay [249]	Q8-HSDT	96.0666	71.2453	56.5546	55.8911	55.6799	55.6722
2	SSSS	Present	SQ8-IFSDT	48.0327	34.6997	27.5296	27.2868	27.2288	27.2335
		Neves et al. [305]	HSDT	48.7807	34.7654	27.5362	27.2979	27.2423	27.2472
		Pradyumna and Bandyopadhyay [249]	Q8-HSDT	47.8259	34.3338	27.4449	27.1789	27.0961	27.0937
	CCCC	Present	SQ8-IFSDT	85.6285	63.6310	47.4525	46.8691	46.7030	46.7039
		Neves et al. [305]	HSDT	86.3088	63.4398	47.5205	46.9447	46.7820	46.7835
		Pradyumna and Bandyopadhyay [249]	Q8-HSDT	84.4431	62.9748	36.2487	35.6633	35.4745	35.4669

Table 4.6 Continued

10	SSSS	Present	SQ8-IFSDT	37.6144	28.6359	24.0993	23.9541	23.9217	23.9253
		Neves et al. [305]	HSDT	38.2792	28.8072	24.2472	24.1063	24.0762	24.0802
		Pradyumna and Bandyopadhyay [249]	Q8-HSDT	37.2593	28.2757	19.3892	19.1562	19.0809	19.0778
	CCCC	Present	SQ8-IFSDT	70.8227	51.9144	40.5104	40.1104	39.9959	39.9962
		Neves et al. [305]	HSDT	71.7634	52.0900	40.8099	40.4145	40.3028	40.3037
		Pradyumna and Bandyopadhyay [249]	Q8-HSDT	69.8224	51.3803	33.6611	33.1474	32.9812	32.9743
∞	SSSS	Present	SQ8-IFSDT	31.7979	23.7119	19.3437	19.1800	19.1273	19.1252
		Neves et al. [305]	HSDT	31.7000	23.5827	19.2796	19.1193	19.0675	19.0654
		Pradyumna and Bandyopadhyay [249]	Q8-HSDT	31.9866	24.1988	19.0917	18.9352	18.8848	18.8827
	CCCC	Present	SQ8-IFSDT	60.2024	43.2974	33.1225	32.7435	32.6213	32.6162
		Neves et al. [305]	HSDT	60.3660	43.1880	33.0576	32.6810	32.5594	32.5543
		Pradyumna and Bandyopadhyay [249]	Q8-HSDT	61.0568	44.2962	32.4802	32.0976	31.9741	31.9689

Table 4.7 The effects of power-law index (k) on the DFFs ($\bar{\bar{\omega}}$) of FG (Al/Al_2O_3) SP shells for different radius-to-length ratios (R/a).

k	**BCs**	**References**	**Models**	***R/a***					
				***R/a* = 0.5**	***R/a* = 1**	***R/a* = 5**	***R/a* = 10**	***R/a* = 50**	**Plate**
0	SSSS	Present	SQ8-IFSDT	125.9402	79.1503	44.4425	42.7701	42.2190	42.1959
		Neves et al. [305]	HSDT	126.2994	79.2626	44.4455	42.7709	42.2192	42.1961
		Pradyumna and Bandyopadhyay [249]	Q8-HSDT	124.1581	78.2306	44.0073	42.3579	41.8145	41.7917
	CCCC	Present	SQ8-IFSDT	176.4617	122.0283	74.7629	72.6923	72.0159	71.9876
		Neves et al. [305]	HSDT	176.8125	122.0934	74.8207	72.7536	72.0784	72.0502
		Pradyumna and Bandyopadhyay [249]	Q8-HSDT	173.9595	120.9210	73.5550	71.4659	70.7832	70.7546
0.2	SSSS	Present	SQ8-IFSDT	117.3811	73.4592	40.6879	39.1067	38.5984	38.5817
		Neves et al. [305]	HSDT	117.3053	73.2663	40.3936	38.8074	38.2988	38.2827
		Pradyumna and Bandyopadhyay [249]	Q8-HSDT	115.7499	72.6343	41.7782	40.2608	39.7629	39.7426
	CCCC	Present	SQ8-IFSDT	163.5725	113.1691	68.6616	66.7140	66.0922	66.0714
		Neves et al. [305]	HSDT	163.0852	112.7143	68.2142	66.2686	65.6498	65.6299
		Pradyumna and Bandyopadhyay [249]	Q8-HSDT	161.3704	112.2017	69.6597	67.7257	67.0956	67.0698
0.5	SSSS	Present	SQ8-IFSDT	107.9893	67.2395	36.6030	35.1180	34.6525	34.6419
		Neves et al. [305]	HSDT	108.0044	67.1623	36.4453	34.9574	34.4922	34.4820
		Pradyumna and Bandyopadhyay [249]	Q8-HSDT	106.5014	66.5025	38.7731	37.3785	36.9234	36.9057
	CCCC	Present	SQ8-IFSDT	149.3293	103.4264	61.9270	60.1076	59.5406	59.5268
		Neves et al. [305]	HSDT	149.0931	103.1804	61.6902	59.8745	59.3112	59.2985
		Pradyumna and Bandyopadhyay [249]	Q8-HSDT	147.4598	102.5983	64.6114	62.8299	62.2519	62.2291
1	SSSS	Present	SQ8-IFSDT	97.5959	60.5004	32.4299	31.0637	30.6460	30.6407
		Neves et al. [305]	HSDT	97.6938	60.5121	32.3691	31.0012	30.5840	30.5792
		Pradyumna and Bandyopadhyay [249]	Q8-HSDT	96.2587	59.8521	34.6004	33.3080	32.8881	32.8726
	CCCC	Present	SQ8-IFSDT	133.8674	92.9025	54.9262	53.2568	52.7489	52.7413
		Neves et al. [305]	HSDT	133.8751	92.8282	54.8597	53.1956	52.6921	52.6856
		Pradyumna and Bandyopadhyay [249]	Q8-HSDT	132.3396	92.2147	57.8619	56.2222	55.6923	55.6722
2	SSSS	Present	SQ8-IFSDT	86.0033	53.3588	28.7678	27.5853	27.2340	27.2335
		Neves et al. [305]	HSDT	86.2288	53.4659	28.7833	27.5984	27.2474	27.2472
		Pradyumna and Bandyopadhyay [249]	Q8-HSDT	84.8206	52.7875	28.7459	27.5110	27.1085	27.0937
	CCCC	Present	SQ8-IFSDT	117.7538	81.9981	48.5959	47.1391	46.7064	46.7039
		Neves et al. [305]	HSDT	118.0167	82.0948	48.6656	47.2135	46.7849	46.7835
		Pradyumna and Bandyopadhyay [249]	Q8-HSDT	116.4386	81.3963	37.3914	35.9568	35.4861	35.4669

Table 4.7 Continued

10	SSSS	Present	SQ8-IFSDT	66.1520	42.1234	24.9188	24.1492	23.9247	23.9253
		Neves et al. [305]	HSDT	66.7088	42.4365	25.0772	24.3034	24.0791	24.0802
		Pradyumna and Bandyopadhyay [249]	Q8-HSDT	65.2296	41.6702	20.4691	19.4357	19.0922	19.0778
	CCCC	Present	SQ8-IFSDT	93.1927	65.3824	41.2994	40.2967	39.9986	39.9962
		Neves et al. [305]	HSDT	93.9111	65.8103	41.6016	40.5998	40.3049	40.3037
		Pradyumna and Bandyopadhyay [249]	Q8-HSDT	92.1387	64.8773	34.6658	33.4057	32.9916	32.9743
∞	SSSS	Present	SQ8-IFSDT	56.9618	35.8132	20.1382	19.3838	19.1355	19.1252
		Neves et al. [305]	HSDT	57.0657	35.8131	20.0818	19.3251	19.0759	19.0654
		Pradyumna and Bandyopadhyay [249]	Q8-HSDT	57.2005	36.2904	19.8838	19.1385	18.8930	18.8827
	CCCC	Present	SQ8-IFSDT	79.8423	55.2251	33.8687	32.9340	32.6289	32.6162
		Neves et al. [305]	HSDT	79.8889	55.1653	33.8061	32.8722	32.5671	32.5543
		Pradyumna and Bandyopadhyay [249]	Q8-HSDT	80.7722	56.2999	33.2343	32.2904	31.9819	31.9689

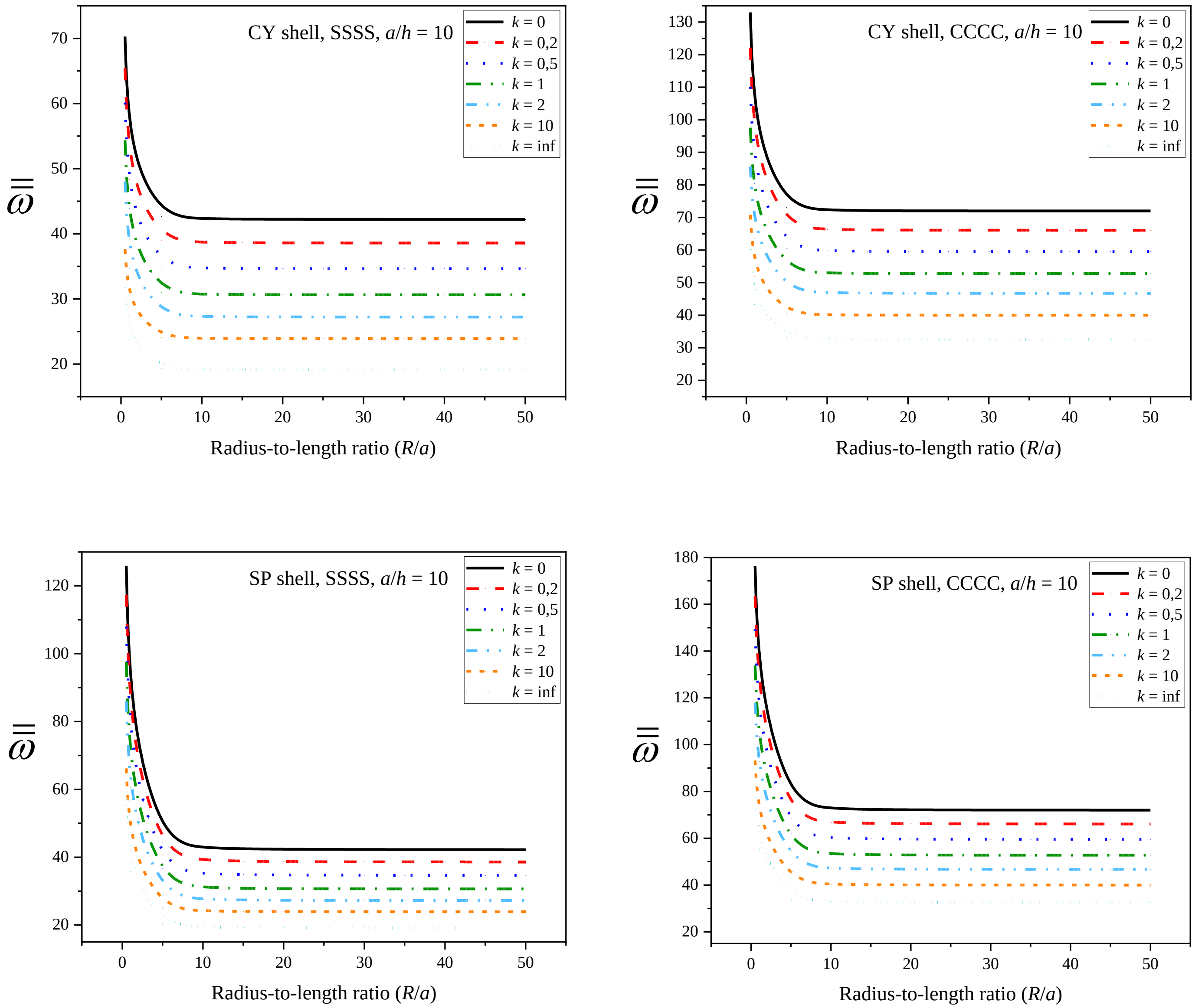

Figure 4.4 The effects of radius-to-length ratio (R/a) on the DFFs of FG (Al/Al_2O_3) CY and SP shells with different index (k) under SSSS and CCCC conditions.

Example 4:

Table 4.8 presents the DFF of SP FG (Al/Al_2O_3) shells with different power-law index (k) and a/h = 10. The results are compared with solutions from Neves et al. [305], Fares et al. [306], Sayyad and Ghugal [223], and Pradyumna and Bandyopadhyay [249]. The comparison reveals excellent agreement, thereby validating the accuracy of the proposed model. Overall, the DFFs decrease with increasing values of the power-law index (k), which corresponds to a higher metal volume fraction and, consequently, reduced stiffness of the shell. At k = 0, the material is entirely ceramic, resulting in maximum stiffness and the highest frequencies. In contrast, as k approaches ∞, the composition becomes fully metallic, leading to minimum stiffness and the lowest frequencies.

Table 4.8 The effects of the power-law index (k) on the DFFs ($\bar{\bar{\omega}}$) of FG (Al/Al_2O_3) SP shells.

R_x/a	R_y/b	References	Models	Power-law (k)				
				k = 0	k = 1	k = 2	k = 10	$k = \infty$
1	1	Present	SQ8-IFSDT	79.1503	60.5004	53.3588	42.1234	35.8132
		Neves et al. [305]	HSDT	79.2626	60.5121	53.4659	42.4365	35.8131
		Fares et al. [306]	LW-FSDT	-	61.1339	53.9021	42.3232	-
		Sayyad and Ghugal [223]	FSDT	80.7278	61.6277	54.3885	43.1749	36.4940
			HSDT	80.6496	61.5875	54.3427	43.0656	36.4586
		Pradyumna and Bandyopadhyay [249]	Q8-HSDT	-	59.8521	52.7875	41.6702	-
5	5	Present	SQ8-IFSDT	44.4425	32.4299	28.7678	24.9188	20.1382
		Neves et al. [305]	HSDT	44.4455	32.3691	28.7833	25.0772	20.0818
		Fares et al. [306]	LW-FSDT	-	32.5494	28.8368	24.6444	-
		Sayyad and Ghugal [223]	FSDT	44.7919	32.7308	29.0914	25.3157	20.2496
			HSDT	44.6271	32.6273	28.9656	25.0724	20.1751
		Pradyumna and Bandyopadhyay [249]	Q8-HSDT	-	34.6004	28.7459	20.4691	-
10	10	Present	SQ8-IFSDT	42.7701	31.0637	27.5853	24.1492	19.3838
		Neves et al. [305]	HSDT	42.7709	31.0012	27.5984	24.3034	19.3251
		Fares et al. [306]	LW-FSDT	-	31.1043	27.5692	23.8077	-
		Sayyad and Ghugal [223]	FSDT	43.0456	31.2826	27.8307	24.4868	19.4602
			HSDT	42.8732	31.1729	27.6972	24.2324	19.3822
		Pradyumna and Bandyopadhyay [249]	Q8-HSDT	-	33.3080	27.5110	19.4357	-
50	50	Present	SQ8-IFSDT	42.2190	30.6460	27.2340	23.9247	19.1350
		Neves et al. [305]	HSDT	42.2192	30.5840	27.2474	24.0791	19.0759
		Fares et al. [306]	LW-FSDT	-	30.6378	27.1630	23.5415	-
		Sayyad and Ghugal [223]	FSDT	42.4696	30.8208	27.4344	24.2300	19.1998
			HSDT	42.2946	30.7088	27.2979	23.9713	19.1207
		Pradyumna and Bandyopadhyay [249]	Q8-HSDT	-	32.8881	27.1085	19.0922	-

Example 5:

Table 4.9 presents the DFFs of thick FG (Al/Al_2O_3) DCSSs for various power-law indices (k), with a/h = 5. The DFFs are computed using the SQ8-IFSDT model and compared with results obtained by Sayyad and Ghugal using the FSDT and HSDT models [223]. The table demonstrates that, as the index (k) increases, the DFFs consistently decrease across all shell types, indicating a softening effect caused by the material gradient. The SQ8-IFSDT results show excellent agreement with Sayyad and Ghugal's HSDT results [223], confirming the accuracy and reliability of the proposed model. Among the different shell types, CY and HYP shells exhibit slightly lower DFFs compared to SP and ELP shells for the same value of k. The results for FL plates are included as a reference case, showing similar trends but without the additional influence of curvature.

Table 4.9 The effects of the power-law index (k) on the DFFs ($\bar{\omega}$) of thick FG (Al/Al_2O_3) DCSSs.

Types of shell	References	Models	Power-law (k)				
			k = 0	k = 1	k = 5	k = 10	k = ∞
CY shell (Rx/a = 5, Ry/b = ∞)	Present	SQ8-IFSDT	0.21139	0.16268	0.13528	0.12942	0.10779
	Sayyad and Ghugal [223]	FSDT	0.21482	0.16546	0.14013	0.13458	0.10953
		HSDT	0.21199	0.16352	0.13600	0.13019	0.10809
SP Shell (R_x/a = 5, R_y/b = 5)	Present	SQ8-IFSDT	0.21387	0.16429	0.13622	0.13031	0.10904
	Sayyad and Ghugal [223]	FSDT	0.21744	0.16748	0.14142	0.13574	0.11086
		HSDT	0.21465	0.16558	0.13738	0.13143	0.10944
HYP shell (R_x/a = 5, R_y/b = -5)	Present	SQ8-IFSDT	0.20927	0.16159	0.13461	0.12866	0.10671
	Sayyad and Ghugal [223]	FSDT	0.21333	0.16452	0.13955	0.13400	0.10877
		HSDT	0.21050	0.16256	0.13537	0.12957	0.10732
ELP shell (R_x/a = 5, R_y/b = 7.5)	Present	SQ8-IFSDT	0.21301	0.16370	0.13588	0.13000	0.10861
	Sayyad and Ghugal [223]	FSDT	0.21644	0.16669	0.14091	0.13530	0.11036
		HSDT	0.21364	0.16478	0.13684	0.13095	0.10893
FL plate (R_x/a = ∞, R_y/b = ∞)	Present	SQ8-IFSDT	0.21121	0.16303	0.13583	0.12986	0.10770
	Sayyad and Ghugal [223]	FSDT	0.21424	0.16521	0.14014	0.13458	0.10924
		HSDT	0.21139	0.16324	0.13595	0.13014	0.10779

Example 6:

Table 4.10 presents the DFFs of FG DCSSs with varying radii-to-length ratios (R/a), for a/h = 5 and k = 2. The results are compared with those obtained by Sayyad and Ghugal [223], using the FSDT and HSDT models. Additionally, the table includes the percentage differences between the present results and those derived from the other models. The key observations are as follows:

- For all shell types, the DFFs exhibit minimal variation as the radii-to-length ratios increase. This suggests that the DFFs stabilize at higher curvature values, indicating a stabilization of the dynamic behavior.
- The SQ8-IFSDT results consistently show excellent agreement with the HSDT results, with differences generally below 1%, validating the accuracy and reliability of the proposed method.
- As the radii-to-length ratio increases, the frequencies of CY and HYP shells increase, while those of SP and ELP shells decrease.

Table 4.10 The effects of the radii-to-length ratios on the DFFs ($\bar{\omega}$) of FG (Al/Al_2O_3) shells.

Types of shell	R_x/a	R_y/b	Present	Sayyad and Ghugal [223]			
			SQ8-IFSDT	FSDT	Difference (%)	HSDT	Difference (%)
CY shell	5	∞	0.14657	0.14996	-2.2606	0.14760	-0.6978
	10	∞	0.14675	0.14978	-2.0230	0.14739	-0.4342
	20	∞	0.14689	0.14978	-1.9295	0.14739	-0.3392
	50	∞	0.14699	0.14981	-1.8824	0.14741	-0.2849
	100	∞	0.14703	0.14983	-1.8688	0.14743	-0.2713
SP shell	5	5	0.14785	0.15167	-2.5186	0.14936	-1.0110
	10	10	0.14689	0.15012	-2.1516	0.14775	-0.5821
	20	20	0.14683	0.14982	-1.9957	0.14743	-0.4070
	50	50	0.14694	0.14980	-1.9092	0.14740	-0.3121
	100	100	0.14699	0.14982	-1.8889	0.14741	-0.2849
HYP shell	5	-5	0.14577	0.14922	-2.3120	0.14683	-0.7219
	10	-10	0.14674	0.14969	-1.9707	0.14729	-0.3734
	20	-20	0.14698	0.14981	-1.8891	0.14740	-0.2849
	50	-50	0.14705	0.14984	-1.8620	0.14744	-0.2645
	100	-100	0.14706	0.14985	-1.8619	0.14744	-0.2577
ELP shell	5	7.5	0.14737	0.15100	-2.4040	0.14867	-0.8744
	10	15	0.14683	0.14998	-2.1003	0.14760	-0.5217
	20	30	0.14685	0.14980	-1.9693	0.14741	-0.3799
	50	75	0.14695	0.14980	-1.9025	0.14740	-0.3053
	100	150	0.14700	0.14982	-1.8823	0.14742	-0.2849

Difference (%) = [(Present result - Analytical result) / Analytical result] × 100

Example 7:

In the last example, the effects of both the thickness ratio (a/h) and power-law index (k) on the DFFs of CCCC FG (Al/Al_2O_3) CY shells are summarized in **Table 4.11** and **Figure 4.5**, with R/a =10. The present results are also compared with those from Neves et al. [305], Fares et al. [306], and Pradyumna and Bandyopadhyay [249], showing strong agreement with published data. From **Figure 4.5**, it can be seen that an increase in the index (k) leads to a sharp decrease in CY shell frequencies, especially from k = 0 to 2. This trend occurs because an increasing power-law index reduces the ceramic fraction while increasing the metal fraction, thereby reducing shell rigidity. Conversely, frequencies increase with a higher a/h ratio, highlighting the influence of shell thickness on its vibrational behavior.

Table 4.11 The DFFs ($\overline{\omega}$) of CCCC FG (Al/Al_2O_3) CY shells for various side-to-thickness ratios (a/h) and power-law index (k).

k	**References**	**Models**	**Side-to-thickness ratios (*a*/*h*)**					
			***a*/*h* =5**	***a*/*h* =10**	***a*/*h* =15**	***a*/*h* =20**	***a*/*h* =50**	***a*/*h* =100**
0	Present	SQ8-IFSDT	58.7906	72.2699	76.4775	78.4950	85.6155	102.4167
	Neves et al. [21]	HSDT	59.0433	72.3272	76.4904	78.4918	85.6073	102.3351
	Fares et al. [37]	LW-FSDT	60.6930	73.1994	76.2482	77.2742	86.3801	103.5890
	Pradyumna and Bandyopadhyay [78]	Q9-HSDT	58.2858	71.7395	75.0439	77.0246	84.8800	102.9227
0.5	Present	SQ8-IFSDT	49.3529	59.7537	62.9578	64.5334	70.7172	85.8410
	Neves et al. [21]	HSDT	49.3050	59.5188	62.6780	64.2371	70.4237	85.4780
	Fares et al. [37]	LW-FSDT	49.2813	59.2366	62.4537	64.4322	70.5642	86.6801
	Pradyumna and Bandyopadhyay [78]	Q9-HSDT	48.7185	58.5305	61.5835	63.1381	69.8604	86.5452
1	Present	SQ8-IFSDT	43.8515	52.9399	55.7458	57.1421	62.8228	76.8258
	Neves et al. [21]	HSDT	43.9548	52.8776	55.6437	57.0255	62.7088	76.6386
	Fares et al. [37]	LW-FSDT	43.8218	52.7402	55.3350	58.2602	62.8351	78.7569
	Pradyumna and Bandyopadhyay [78]	Q9-HSDT	43.4243	52.0173	54.7015	56.0880	62.2152	77.0774

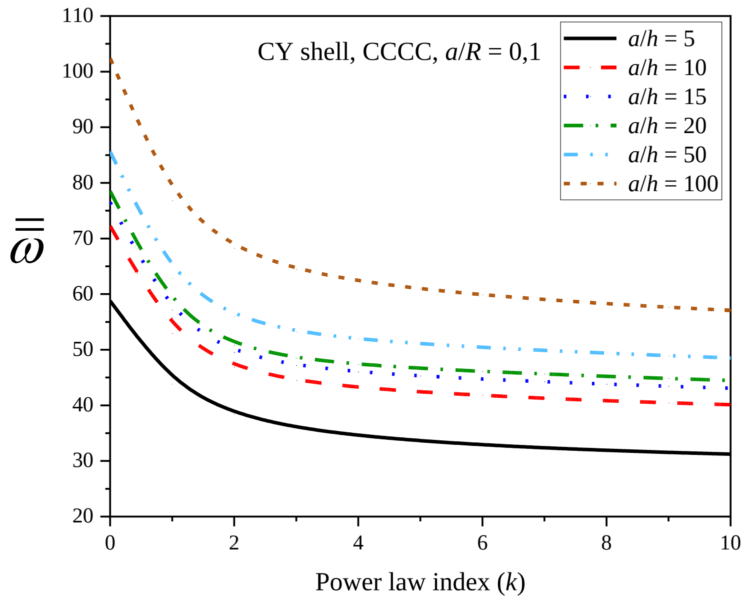

Figure 4.5 The effect of side-to-thickness ratio (a/h) and power-law index (k) on the DFFs of CCCC FG (Al/Al_2O_3) CY shells.

4.4 Conclusion

An advanced FE model, SQ8-IFSDT, has been developed to analyze the vibration behavior of FG DCSs. This model surpasses traditional approaches by implementing a parabolic function to correct the distribution of transverse shear stresses through the shell thickness. A convergence study demonstrates that the proposed FE model is both computationally efficient and stable, even at lower mesh densities. Comparisons with existing literature confirm the accuracy of the model. Furthermore, new findings—previously unreported—are presented, offering novel insights into the free vibration analysis of FG DCSSs. The key findings include:

- The power-law index (k), controlling the FG material's ceramic-to-metal ratio, strongly affects the DFFs. Increasing the metal fraction (higher k) reduces rigidity, decreasing frequency values, while a ceramic-rich composition (low k) yields higher frequencies due to increased stiffness.
- The radius-to-length ratio (R/a) and side-to-thickness ratio (a/h) affect the natural frequencies. Generally, higher radius-to-length ratios decrease frequency values for CY shells, while increasing the thickness ratio raises the frequency.
- The FE model results exhibit excellent agreement with HSDT analytical solutions, confirming its robustness as a tool for the analysis of FG DCSSs.

This work offers valuable insights for engineering applications requiring precise control of vibrational properties in FG DCSSs, supporting the advanced design and manufacturing of these structures.

General conclusion

General conclusion

This work aims to analyze the static and free vibration response of doubly curved shallow shells (DCSSs) composed of functionally graded materials (FGMs). Traditional composite materials often encounter limitations when subjected to extreme conditions, such as high thermal gradients, intense mechanical loads, or aggressive environmental factors. These limitations may lead to stress concentrations, material failure, and reduced durability. In contrast, FGMs provide enhanced performance by gradually varying material properties across the thickness of the structure. This gradation improves resistance to thermal stresses and mechanical loads while minimizing stress discontinuities at material interfaces, thereby enhancing structural integrity and durability. As a result, FGMs are particularly well suited for complex structures like DCSSs, which are widely employed in aerospace, marine, and civil engineering applications where both mechanical strength and thermal resistance are essential.

A C^0 8-node isoparametric quadrilateral element with five degrees of freedom per node, referred to as QS8-IFSDT, has been developed based on the improved first-order shear deformation theory. The theory corrects the distribution of the shear stresses by replacing the shear correction factor with a parabolic function that satisfies the traction condition of being zero at both the top and bottom surfaces of the FG DCSSs. a result, the model provides a more realistic and precise representation of the actual shear stress distribution through the shell thickness.

In this work, five types of DCSs has been analyzed: flat (FL) plates, cylindrical (CY) shells, spherical (SP) shells, hyperbolic paraboloid (HYP) shells, and elliptical (ELP) shells—each characterized by distinct curvature profiles and structural responses. To evaluate the mechanical behavior of the FG DCSSs, a power-law distribution was adopted, enabling a smooth gradation of material properties through the thickness. The classical Hamilton's principle was employed to derive the governing equations of motion for these structures.

The obtained results were compared with 2D analytical solutions and finite element models available in the literature. The comparison demonstrated that the proposed FE model offers superior accuracy, faster convergence, and broader applicability in analyzing FG DCSSs. Additionally, a detailed parametric including the power-law index (k), side-to-thickness ratio (a/h), radius-to-thickness ratio (R/h), radius-to-length ratio (R/a), boundary conditions on the transverse displacement, normal and shear stresses, natural frequency, dynamic mode shapes of FG DCSSs.

In the following, some of the important observations can be concluded from this work:

- Convergence studies with increasing mesh refinement confirm the stability and accuracy of the numerical model, with results consistently approaching reliable solutions—demonstrating the model's precision and robustness.
- The Q8-IFSDT model accurately predicts deflections, normal and shear stresses, and natural frequencies, showing excellent agreement with HSDT analytical solutions and thereby validating the effectiveness of the proposed approach.
- The study also presents new results that have not been previously reported in the literature, offering fresh insights into the mechanical and dynamic behavior of FG DCSSs.
- The results provide valuable insights for the design and manufacturing of

The current FE model combines high accuracy with simplicity, making it an efficient and effective tool for analyzing bending and free vibration in various types of FG DCSSs. This robustness underscores its broad applicability to practical engineering challenges.

The presented FE model, Q8-IFSDT, combines high accuracy with computational simplicity, making it an efficient and effective tool for analyzing both bending and free vibration behaviors in various types of FG DCSSs. Its robustness highlights its wide applicability to real-world engineering challenges.

Perspectives

The FE model QS8-IFSDT is distinguished by its simplicity among existing models. Its results are exceptionally promising, highlighting its strong potential for extension to investigate a broader spectrum of phenomena. The next step will involve:

- Developing another efficient model, named SQ4-RHSDT, which is a four-node C^1-continuous isoparametric quadrilateral element based on a refined higher-order shear deformation theory.
- Exploring other phenomena such as buckling, post-buckling, thermal and hygrothermal, nonlinear dynamics, wave propagation, and viscoelastic responses on FG DCSSs.
- Investigating other structural configurations, such as sandwich structures with and without auxetic cores, bio-inspired laminated structures, and bidirectional and multidirectional gradient distribution structures

Bibliography

[1] Alkunte, S., et al. Advancements and Challenges in Additively Manufactured Functionally Graded Materials: A Comprehensive Review. Journal of Manufacturing and Materials Processing, 2024. 8, DOI: 10.3390/jmmp8010023.

[2] Tarlochan, F., Functionally graded material: a new breed of engineered material. J Appl Mech Eng, 2012. 1(5): p. 1-2.

[3] Kanu, N.J., et al., Fracture problems, vibration, buckling, and bending analyses of functionally graded materials: A state-of-the-art review including smart FGMS. Particulate Science and Technology, 2019. 37(5): p. 583-608.

[4] Parihar, R.S., S.G. Setti, and R.K. Sahu, Recent advances in the manufacturing processes of functionally graded materials: a review. 2018. 25(2): p. 309-336.

[5] Birman, V. and L.W. Byrd, Modeling and analysis of functionally graded materials and structures. 2007.

[6] Hasselman, D. and G.E. Youngblood, Enhanced thermal stress resistance of structural ceramics with thermal conductivity gradient. Journal of the American Ceramic Society, 1978. 61(1-2): p. 49-52.

[7] Koizumi, M. and M. Niino, Overview of FGM research in Japan. Mrs Bulletin, 1995. 20(1): p. 19-21.

[8] Mahamood, R.M. and E.T. Akinlabi, Introduction to Functionally Graded Materials, in Functionally Graded Materials, R.M. Mahamood and E.T. Akinlabi, Editors. 2017, Springer International Publishing: Cham. p. 1-8.

[9] Zhang, C., et al., Additive manufacturing of functionally graded materials: A review. Materials Science and Engineering: A, 2019. 764: p. 138209.

[10] Radwan, M., et al., Fabrication of crack-free SUS316L/Al2O3 functionally graded materials by spark plasma sintering. Journal of Materials Science, 2011. 46(17): p. 5807-5814.

[11] Mahamood, R.M. and E.T. Akinlabi, Types of Functionally Graded Materials and Their Areas of Application, in Functionally Graded Materials, R.M. Mahamood and E.T. Akinlabi, Editors. 2017, Springer International Publishing: Cham. p. 9-21.

[12] Knoppers, G., et al., The reality of functionally graded material products. 2004.

[13] He, L.-H. and M.V. Swain, Enamel—A functionally graded natural coating. Journal of Dentistry, 2009. 37(8): p. 596-603.

[14] Flynn, C.O. and B.A.O. McCormack, A three-layer model of skin and its application in simulating wrinkling. Computer Methods in Biomechanics and Biomedical Engineering, 2009. 12(2): p. 125-134.

[15] Niino, M., Functionally gradient materials as thermal barrier for space plane. J. Jpn. Composite Mater., 1987. 13: p. 257-264.

[16] Saleh, B., et al., 30 Years of functionally graded materials: An overview of manufacturing methods, Applications and Future Challenges. Composites Part B: Engineering, 2020. 201: p. 108376.

[17] Sajjad, A., et al., Functionally graded materials: an overview of dental applications. World Journal of Dentistry, 2017. 9(2): p. 137-144.

[18] Sato, M., A. Inoue, and H. Shima, Bamboo-inspired optimal design for functionally graded hollow cylinders. PLoS One, 2017. 12(5): p. e0175029.

[19] Bever, M.B. and P.E. Duwez, Gradients in composite materials. Materials Science and Engineering, 1972. 10: p. 1-8.

[20] Shen, M. and M.B. Bever, Gradients in polymeric materials. Journal of Materials Science, 1972. 7(7): p. 741-746.

[21] Koizumi, M., The concept of FGM. 1993.

[22] Koizumi, M., FGM activities in Japan. Composites Part B: Engineering, 1997. 28(1): p. 1-4.

[23] Mohammadi, M., M. Rajabi, and M. Ghadiri, Functionally graded materials (FGMs): A review of classifications, fabrication methods and their applications. Processing and Application of Ceramics, 2021. 15(4): p. 319-343.

[24] Hirai, T., Functional gradient materials. Materials science and technology, 1996: p. 293-341.

[25] Koppad, P.G., et al., Gaseous Phase Processing Techniques for Functionally Graded Materials, in Functionally Graded Materials (FGMs). 2021, CRC Press. p. 49-76.

[26] Sharma, N.K., M. Bhandari, and A. Dean, Applications of functionally graded materials (FGMs). Int J Eng Res Technol, 2014. 2: p. 334-339.

[27] Bharti, I., N. Gupta, and K. Gupta, Novel applications of functionally graded nano, optoelectronic and thermoelectric materials. International Journal of Materials, Mechanics and Manufacturing, 2013. 1(3): p. 221-224.

[28] Mahamood, R.M., et al. Functionally Graded Material: An overview. 2012.

[29] Mahamood, R.M. and E.T. Akinlabi, Laser metal deposition of functionally graded Ti6Al4V/TiC. Materials & Design, 2015. 84: p. 402-410.

[30] Miao, X. and D. Sun, Graded/Gradient Porous Biomaterials. Materials, 2010. 3(1): p. 26-47.

[31] Mahamood, R. M., & Akinlabi, E. T. (2015). Modelling of process parameters influence on degree of porosity in laser metal deposition process. In Transactions on Engineering Technologies: International MultiConference of Engineers and Computer Scientists 2014 (pp. 31-42). Springer Netherlands.

[32] Lu, L., et al., Mechanical properties estimation of functionally graded materials using surface waves recorded with a laser interferometer. NDT & E International, 2011. 44(2): p. 169-177.

[33] Schneider, M.J. and M.S. Chatterjee, Introduction to surface hardening of steels. 2013.

[34] Patricia, P., et al., Laser Engineering Net Shaping Method in the Area of Development of Functionally Graded Materials (FGMs) for Aero Engine Applications - A Review, in Fiber Laser, P. Mukul Chandra, Editor. 2016, IntechOpen: Rijeka. p. Ch. 17.

[35] Gabbrielli, R., I.G. Turner, and C.R. Bowen, Development of Modelling Methods for Materials to be Used as Bone Substitutes. Key Engineering Materials, 2008. 361-363: p. 903-906.

[36] Popovich, V.A., et al., Functionally graded Inconel 718 processed by additive manufacturing: Crystallographic texture, anisotropy of microstructure and mechanical properties. Materials & Design, 2017. 114: p. 441-449.

[37] Mortensen, A. and S. Suresh, Functionally graded metals and metal-ceramic composites: Part 1 Processing. International Materials Reviews, 1995. 40(6): p. 239-265.

[38] Saad, A.R., A Review on Functionally Graded Materials and Their Applications in the Field of Prosthetics. ERJ. Engineering Research Journal, 2022. 45(4): p. 553-560.

[39] Malinina, M., T. Sammi, and M.M. Gasik. Corrosion resistance of homogeneous and FGM coatings. in Materials Science Forum. 2005. Trans Tech Publ.

[40] Lian, Y., et al., Preparation and properties of CVD-W coated W/Cu FGM mock-ups. Fusion Engineering and Design, 2013. 88(9): p. 1694-1698.

[41] CPM, S.A., B. Varghese, and A. Baby, A review on functionally graded materials. Int. J. Eng. Sci, 2014. 3: p. 90-101.

[42] Ansari, A.A., et al., Prospects of Nanotechnology in Clinical Immunodiagnostics. Sensors, 2010. 10(7): p. 6535-6581.

[43] Seol, Y.-J., T.-Y. Kang, and D.-W. Cho, Solid freeform fabrication technology applied to tissue engineering with various biomaterials. Soft matter, 2012. 8(6): p. 1730-1735.

[44] Malandrino, G., Chemical Vapour Deposition. Precursors, Processes and Applications. Edited by Anthony C. Jones and Michael L. Hitchman. 2009, WILEY-VCH Verlag Weinheim.

[45] Groves, J.F. and H.N.G. Wadley, Functionally graded materials synthesis via low vacuum directed vapor deposition. Composites Part B: Engineering, 1997. 28(1): p. 57-69.

[46] Kawasaki, A. and R. Watanabe, Concept and P/M fabrication of functionally gradient materials. Ceramics International, 1997. 23(1): p. 73-83.

[47] Gasik, M., A. Kawasaki, and S. Ueda, Design and Powder Metallurgy Processing of Functionally Graded Materials, in Materials Development and Processing - Bulk Amorphous Materials, Undercooling and Powder Metallurgy. 2000. p. 258-264.

[48] Kırmızı, G., H. Arık, and H. Çinici, Experimental study on mechanical and ballistic behaviours of silicon carbide reinforced functionally graded aluminum foam composites. Composites Part B: Engineering, 2019. 164: p. 345-357.

[49] Surya, M.S. and G. Prasanthi, Tribological behaviour of aluminum silicon carbide functionally graded material. Tribology in Industry, 2018. 40(2): p. 247.

[50] Saxena, A., et al., Improved functional response of spark plasma sintered hydroxyapatite based functionally graded materials: An impedance spectroscopy perspective. Ceramics International, 2019. 45(6): p. 6673-6683.

[51] Watanabe, Y., H. Sato, and E. Miura-Fujiwara, Functionally Graded Metallic Biomaterials, in Advances in Metallic Biomaterials: Processing and Applications, M. Niinomi, T. Narushima, and M. Nakai, Editors. 2015, Springer Berlin Heidelberg: Berlin, Heidelberg. p. 181-209.

[52] Diouf, P. and A. Jones, Investigation of Bond Strength in Centrifugal Lining of Babbitt on Cast Iron. Metallurgical and Materials Transactions A, 2010. 41(3): p. 603-609.

[53] Kieback, B., A. Neubrand, and H. Riedel, Processing techniques for functionally graded materials. Materials Science and Engineering: A, 2003. 362(1): p. 81-106.

[54] El-Galy, I.M., B.I. Saleh, and M.H. Ahmed, Functionally graded materials classifications and development trends from industrial point of view. SN Applied Sciences, 2019. 1(11): p. 1378.

[55] Watanabe, Y., et al., A Novel Fabrication Method for Functionally Graded Materials under Centrifugal Force: The Centrifugal Mixed-Powder Method. Materials, 2009. 2(4): p. 2510-2525.

[56] Xu, A. and L.L. Shaw, Equal distance offset approach to representing and process planning for solid freeform fabrication of functionally graded materials. Computer-Aided Design, 2005. 37(12): p. 1308-1318.

[57] Boboulos, M.A., CAD-CAM & rapid prototyping application evaluation. 2010: Bookboon.

[58] Hutmacher, D.W., M. Sittinger, and M.V. Risbud, Scaffold-based tissue engineering: rationale for computer-aided design and solid free-form fabrication systems. TRENDS in Biotechnology, 2004. 22(7): p. 354-362.

[59] Pei, Y.T. and J.T.M. De Hosson, Functionally graded materials produced by laser cladding. Acta Materialia, 2000. 48(10): p. 2617-2624.

[60] Chung, H. and S. Das, Functionally graded Nylon-11/silica nanocomposites produced by selective laser sintering. Materials Science and Engineering: A, 2008. 487(1): p. 251-257.

[61] Dimitrov, D., K. Schreve, and N. de Beer, Advances in three dimensional printing – state of the art and future perspectives. Rapid Prototyping Journal, 2006. 12(3): p. 136-147.

[62] Mumtaz, K.A. and N. Hopkinson, Laser melting functionally graded composition of Waspaloy® and Zirconia powders. Journal of Materials Science, 2007. 42(18): p. 7647-7656.

[63] Gasik, M.M., Functionally Graded Materials: bulk processing techniques. International Journal of Materials and Product Technology, 2010. 39(1-2): p. 20-29.

[64] Gayen, D., R. Tiwari, and D. Chakraborty, Static and dynamic analyses of cracked functionally graded structural components: A review. Composites Part B: Engineering, 2019. 173: p. 106982.

[65] Toudehdehghan, A., et al. A brief review of functionally graded materials. in MATEC Web Conferences. 2017. EDP Sciences.

[66] Pompe, W., et al., Functionally graded materials for biomedical applications. Materials Science and Engineering: A, 2003. 362(1): p. 40-60.

[67] Matsuo, S., F. Watari, and N. Ohata, Fabrication of a Functionally Graded Dental Composite Resin Post and Core by Laser Lithography and Finite Element Analysis of its Stress Relaxation Effect on Tooth Root. Dental Materials Journal, 2001. 20(4): p. 257-274.

[68] Watari, F., et al., Biocompatibility of materials and development to functionally graded implant for bio-medical application. Composites Science and Technology, 2004. 64(6): p. 893-908.

[69] Lin, D., et al., Design optimization of functionally graded dental implant for bone remodeling. Composites Part B: Engineering, 2009. 40(7): p. 668-675.

[70] Müller, E., et al., Functionally graded materials for sensor and energy applications. Materials Science and Engineering: A, 2003. 362(1): p. 17-39.

[71] Niino, M., K. Kisara, and M. Mori. Feasibility study of FGM technology in space solar power systems (SSPS). in Materials Science Forum. 2005. Trans Tech Publ.

[72] Bergmann, C.P. and A. Stumpf, Topics in mining, metallurgy and materials engineering. (No Title), 2017.

[73] Mathew, C. and O. Ejiofor, Mechanics and Computational Homogenization of Effective Material Properties of Functionally Graded (Composite) Material Plate FGM. International Journal of Scientific and Research Publications, 2023. 13: p. 128-150.

[74] Voigt, W., Ueber die Beziehung zwischen den beiden Elasticitätsconstanten isotroper Körper. Annalen der Physik, 1889. 274(12): p. 573-587.

[75] Mori, T. and K. Tanaka, Average stress in matrix and average elastic energy of materials with misfitting inclusions. Acta Metallurgica, 1973. 21(5): p. 571-574.

[76] Benveniste, Y., A new approach to the application of Mori-Tanaka's theory in composite materials. Mechanics of Materials, 1987. 6(2): p. 147-157.

[77] Vel, S.S. and R.C. Batra, Exact Solution for Thermoelastic Deformations of Functionally Graded Thick Rectangular Plates. AIAA Journal, 2002. 40(7): p. 1421-1433.

[78] Zaoui, F.Z., et al., Mathematical Approach for Mechanical Behaviour Analysis of FGM Plates on Elastic Foundation. Mathematics, 2022. 10(24): p. 4764.

[79] Delfosse, D., Fundamentals of Functionally Graded Materials. Materials Today, 1998. 1(4): p. 18.

[80] Pu, N., Y. Zhang, and W. Ma, Fracture mechanics analysis of functionally graded materials by an efficient and accurate meshless method. Theoretical and Applied Fracture Mechanics, 2024. 130: p. 104313.

[81] Chung, Y.-L. and S. Chi, The residual stress of functionally graded materials. 2001.

[82] Chi, S. and Y. Chung, Cracking in sigmoid functionally graded coating. J Mech, 2002. 18(2002): p. 41-53p.

[83] Cauchy, A.-L., Sur l'equilibre et le mouvement d'une plaque solide. Exercises de Matematique, 1828. 3(1828): p. 328-355.

[84] Poisson, S.-D., Mémoire sur l'équilibre et le mouvement des corps élastiques. 1828: F. Didot.

[85] Kirchhoff, G., Über das Gleichgewicht und die Bewegung einer elastischen Scheibe. Journal für die reine und angewandte Mathematik (Crelles Journal), 1850. 1850(40): p. 51-88.

[86] Carrera, E. and S. Brischetto, A Survey With Numerical Assessment of Classical and Refined Theories for the Analysis of Sandwich Plates. Applied Mechanics Reviews, 2008. 62(1).

[87] Giorgio, I., Lattice shells composed of two families of curved Kirchhoff rods: an archetypal example, topology optimization of a cycloidal metamaterial. Continuum Mechanics and Thermodynamics, 2021. 33(4): p. 1063-1082.

[88] Reddy, J.N., Mechanics of laminated composite plates and shells: theory and analysis. 2003: CRC press.

[89] Aron, H., Das Gleichgewicht und die Bewegung einer unendlich dünnen, beliebig gekrümmten elastischen Schale. Journal für die reine und angewandte Mathematik, 1874. 1874(78): p. 136-174.

[90] Love, A.E.H. and G.H. Darwin, XVI. The small free vibrations and deformation of a thin elastic shell. Philosophical Transactions of the Royal Society of London. (A.), 1888. 179: p. 491-546.

[91] Reissner, E., The Effect of Transverse Shear Deformation on the Bending of Elastic Plates. Journal of Applied Mechanics, 2021. 12(2): p. A69-A77.

[92] Reissner, E., ON BENDING OF ELASTIC PLATES. Quarterly of Applied Mathematics, 1947. 5(1): p. 55-68.

[93] Mindlin, R.D., Influence of Rotatory Inertia and Shear on Flexural Motions of Isotropic, Elastic Plates. Journal of Applied Mechanics, 2021. 18(1): p. 31-38.

[94] BENBAKHTI, A.D., et al., A NEW HIGHER ORDER SHEAR AND NORMAL DEFORMATION THEORY FOR BENDING ANALYSIS OF ADVANCED COMPOSITE PLATES.

[95] Nguyen, T.N., C.H. Thai, and H. Nguyen-Xuan, On the general framework of high order shear deformation theories for laminated composite plate structures: A novel unified approach. International Journal of Mechanical Sciences, 2016. 110: p. 242-255.

[96] Reissner, E., A Consistent Treatment of Transverse Shear Deformations in Laminated Anisotropic Plates. AIAA Journal, 1972. 10(5): p. 716-718.

[97] Reissner, E., Reflections on the Theory of Elastic Plates. Applied Mechanics Reviews, 1985. 38(11): p. 1453-1464.

[98] Ayad, R., Eléments finis de plaque et coque en formulation mixte avec projection en cisaillement. 1993, Compiègne.

[99] Noor, A.K. and W.S. Burton, Assessment of Shear Deformation Theories for Multilayered Composite Plates. Applied Mechanics Reviews, 1989. 42(1): p. 1-13.

[100] Noor, A.K. and W. Scott Burton, Stress and free vibration analyses of multilayered composite plates. Composite Structures, 1989. 11(3): p. 183-204.

[101] Noor, A.K. and W.S. Burton, Assessment of computational models for multilayered anisotropic plates. Composite Structures, 1990. 14(3): p. 233-265.

[102] Hildebrand, F., E. Reissner, and G. Thomas, Notes on the foundations of the theory of small displacements of orthotropic shells. 1949.

[103] Naghdi, P., On the theory of thin elastic shells. Quarterly of applied Mathematics, 1957. 14(4): p. 369-380.

[104] Pister, K.S. and R.A. Westmann, Bending of Plates on an Elastic Foundation. Journal of Applied Mechanics, 1962. 29(2): p. 369-374.

[105] Whitney, J.M. and C.T. Sun, A higher order theory for extensional motion of laminated composites. Journal of Sound and Vibration, 1973. 30(1): p. 85-97.

[106] Nelson, R.B. and D.R. Lorch, A Refined Theory for Laminated Orthotropic Plates. Journal of Applied Mechanics, 1974. 41(1): p. 177-183.

[107] Reddy, J.N., A Simple Higher-Order Theory for Laminated Composite Plates. Journal of Applied Mechanics, 1984. 51(4): p. 745-752.

[108] Ambartsumian, S.A., On the theory of bending of anisotropic plates and shallow shells. Journal of Applied Mathematics and Mechanics, 1960. 24(2): p. 500-514.

[109] Panc, V., Theories of elastic plates. Vol. 2. 1975: Springer Science & Business Media.

[110] Reissner, E., On tranverse bending of plates, including the effect of transverse shear deformation. 1974.

[111] Levinson, M., An accurate, simple theory of the statics and dynamics of elastic plates. Mechanics Research Communications, 1980. 7(6): p. 343-350.

[112] Murthy, M., An improved transverse shear deformation theory for laminated antisotropic plates. 1981.

[113] Nguyen-Xuan, H., C.H. Thai, and T. Nguyen-Thoi, Isogeometric finite element analysis of composite sandwich plates using a higher order shear deformation theory. Composites Part B: Engineering, 2013. 55: p. 558-574.

[114] Levy, M., Memoire sur la theorie des plaques elastiques planes. Journal de mathématiques pures et appliquées, 1877. 3: p. 219-306.

[115] Stein, M., Nonlinear theory for plates and shells including the effects of transverse shearing. AIAA Journal, 1986. 24(9): p. 1537-1545.

[116] Touratier, M., An efficient standard plate theory. International Journal of Engineering Science, 1991. 29(8): p. 901-916.

[117] Arya, H., R.P. Shimpi, and N.K. Naik, A zigzag model for laminated composite beams. Composite Structures, 2002. 56(1): p. 21-24.

[118] Thai, C.H., et al., Isogeometric analysis of laminated composite and sandwich plates using a new inverse trigonometric shear deformation theory. European Journal of Mechanics - A/Solids, 2014. 43: p. 89-108.

[119] Soldatos, K.P., A transverse shear deformation theory for homogeneous monoclinic plates. Acta Mechanica, 1992. 94(3): p. 195-220.

[120] El Meiche, N., et al., A new hyperbolic shear deformation theory for buckling and vibration of functionally graded sandwich plate. International Journal of Mechanical Sciences, 2011. 53(4): p. 237-247.

[121] Akavci, S.S. and A.H. Tanrikulu, Buckling and free vibration analyses of laminated composite plates by using two new hyperbolic shear-deformation theories. Mechanics of Composite Materials, 2008. 44(2): p. 145-154.

[122] Karama, M., K.S. Afaq, and S. Mistou, Mechanical behaviour of laminated composite beam by the new multi-layered laminated composite structures model with transverse shear stress continuity. International Journal of Solids and Structures, 2003. 40(6): p. 1525-1546.

[123] Aydogdu, M., A new shear deformation theory for laminated composite plates. Composite Structures, 2009. 89(1): p. 94-101.

[124] Mantari, J.L., A.S. Oktem, and C. Guedes Soares, Static and dynamic analysis of laminated composite and sandwich plates and shells by using a new higher-order shear deformation theory. Composite Structures, 2011. 94(1): p. 37-49.

[125] Mantari, J.L., A.S. Oktem, and C. Guedes Soares, A new higher order shear deformation theory for sandwich and composite laminated plates. Composites Part B: Engineering, 2012. 43(3): p. 1489-1499.

[126] Thai, C.H., et al., Generalized shear deformation theory for functionally graded isotropic and sandwich plates based on isogeometric approach. Computers & Structures, 2014. 141: p. 94-112.

[127] Shimpi, R.P., Refined Plate Theory and Its Variants. AIAA Journal, 2002. 40(1): p. 137-146.

[128] Daikh, A.A., M.S.A. Houari, and M.A. Eltaher, A novel nonlocal strain gradient Quasi-3D bending analysis of sigmoid functionally graded sandwich nanoplates. Composite Structures, 2021. 262: p. 113347.

[129] Thai, H.-T. and S.-E. Kim, A review of theories for the modeling and analysis of functionally graded plates and shells. Composite Structures, 2015. 128: p. 70-86.

[130] Sofiyev, A.H., Review of research on the vibration and buckling of the FGM conical shells. Composite Structures, 2019. 211: p. 301-317.

[131] Loy, C.T., K.Y. Lam, and J.N. Reddy, Vibration of functionally graded cylindrical shells. International Journal of Mechanical Sciences, 1999. 41(3): p. 309-324.

[132] Reddy, J.N., C.M. Wang, and S. Kitipornchai, Axisymmetric bending of functionally graded circular and annular plates. European Journal of Mechanics - A/Solids, 1999. 18(2): p. 185-199.

[133] Pradhan, S.C., et al., Vibration characteristics of functionally graded cylindrical shells under various boundary conditions. Applied Acoustics, 2000. 61(1): p. 111-129.

[134] Naeem, M.N., S.H. Arshad, and C.B. Sharma, The Ritz formulation applied to the study of the vibration frequency characteristics of functionally graded circular cylindrical shells. Proceedings of the Institution of Mechanical Engineers, Part C: Journal of Mechanical Engineering Science, 2009. 224(1): p. 43-54.

[135] Ng, T.Y., K.Y. Lam, and K.M. Liew, Effects of FGM materials on the parametric resonance of plate structures. Computer Methods in Applied Mechanics and Engineering, 2000. 190(8): p. 953-962.

[136] Woo, J. and S.A. Meguid, Nonlinear analysis of functionally graded plates and shallow shells. International Journal of Solids and Structures, 2001. 38(42): p. 7409-7421.

[137] Yang, J. and H.-S. Shen, Dynamic response of initially stressed functionally graded rectangular thin plates. Composite Structures, 2001. 54(4): p. 497-508.

[138] Najafizadeh, M.M. and M.R. Eslami, Buckling analysis of circular plates of functionally graded materials under uniform radial compression. International Journal of Mechanical Sciences, 2002. 44(12): p. 2479-2493.

[139] Ma, L.S. and T.J. Wang, Nonlinear bending and post-buckling of a functionally graded circular plate under mechanical and thermal loadings. International Journal of Solids and Structures, 2003. 40(13): p. 3311-3330.

[140] Tsukamoto, H., Analytical method of inelastic thermal stresses in a functionally graded material plate by a combination of micro- and macromechanical approaches. Composites Part B: Engineering, 2003. 34(6): p. 561-568.

[141] Woo, J., S.A. Meguid, and L.S. Ong, Nonlinear free vibration behavior of functionally graded plates. Journal of Sound and Vibration, 2006. 289(3): p. 595-611.

[142] Arshad, S.H., M.N. Naeem, and N. Sultana, Frequency analysis of functionally graded material cylindrical shells with various volume fraction laws. Proceedings of the Institution of Mechanical Engineers, Part C: Journal of Mechanical Engineering Science, 2007. 221(12): p. 1483-1495.

[143] Ebrahimi, F. and A. Rastgo, An analytical study on the free vibration of smart circular thin FGM plate based on classical plate theory. Thin-Walled Structures, 2008. 46(12): p. 1402-1408.

[144] Alinia, M.M. and S.A.M. Ghannadpour, Nonlinear analysis of pressure loaded FGM plates. Composite Structures, 2009. 88(3): p. 354-359.

[145] Alijani, F., et al., Nonlinear vibrations of functionally graded doubly curved shallow shells. Journal of Sound and Vibration, 2011. 330(7): p. 1432-1454.

[146] Yuda, H. and Z. Xiaoguang, Parametric Vibrations and Stability of a Functionally Graded Plate. Mechanics Based Design of Structures and Machines, 2011. 39(3): p. 367-377.

[147] Ebrahimi, M.J. and M.M. Najafizadeh, Free vibration analysis of two-dimensional functionally graded cylindrical shells. Applied Mathematical Modelling, 2014. 38(1): p. 308-324.

[148] Du, C. and Y. Li, Nonlinear resonance behavior of functionally graded cylindrical shells in thermal environments. Composite Structures, 2013. 102: p. 164-174.

[149] Du, C., Y. Li, and X. Jin, Nonlinear forced vibration of functionally graded cylindrical thin shells. Thin-Walled Structures, 2014. 78: p. 26-36.

[150] Chakraverty, S. and K.K. Pradhan, FREE VIBRATION OF FUNCTIONALLY GRADED THIN RECTANGULAR PLATES RESTING ON WINKLER ELASTIC FOUNDATION WITH GENERAL BOUNDARY CONDITIONS USING RAYLEIGH–RITZ METHOD. International Journal of Applied Mechanics, 2014. 06(04): p. 1450043.

[151] Chakraverty, S. and K.K. Pradhan, Free vibration of exponential functionally graded rectangular plates in thermal environment with general boundary conditions. Aerospace Science and Technology, 2014. 36: p. 132-156.

[152] Ruan, M. and Z.-M. Wang, Transverse vibrations of moving skew plates made of functionally graded material. Journal of Vibration and Control, 2014. 22(16): p. 3504-3517.

[153] Davar, A. and R. Azarafza, Free Vibration Analysis of Functionally Graded Annular Circular Plates Using Classical Thin Plate Theory Based on Physical Neutral Surface. Journal of Vibration Engineering & Technologies, 2024. 12(3): p. 3873-3896.

[154] Zhang, D.-G. and Y.-H. Zhou, A theoretical analysis of FGM thin plates based on physical neutral surface. Computational Materials Science, 2008. 44(2): p. 716-720.

[155] Damanpack, A.R., et al., Boundary element method applied to the bending analysis of thin functionally graded plates. Latin American Journal of Solids and Structures, 2013. 10.

[156] Chen, C.-S., Nonlinear vibration of a shear deformable functionally graded plate. Composite Structures, 2005. 68(3): p. 295-302.

[157] Liew, K.M., J. Yang, and Y.F. Wu, Nonlinear vibration of a coating-FGM-substrate cylindrical panel subjected to a temperature gradient. Computer Methods in Applied Mechanics and Engineering, 2006. 195(9): p. 1007-1026.

[158] Ferreira, A.J.M., et al., Natural frequencies of functionally graded plates by a meshless method. Composite Structures, 2006. 75(1): p. 593-600.

[159] Sheng, G.G. and X. Wang, Thermal Vibration, Buckling and Dynamic Stability of Functionally Graded Cylindrical Shells Embedded in an Elastic Medium. Journal of Reinforced Plastics and Composites, 2007. 27(2): p. 117-134.

[160] Tornabene, F. and E. Viola, Free vibration analysis of functionally graded panels and shells of revolution. Meccanica, 2009. 44(3): p. 255-281.

[161] Tornabene, F., Free vibration analysis of functionally graded conical, cylindrical shell and annular plate structures with a four-parameter power-law distribution. Computer Methods in Applied Mechanics and Engineering, 2009. 198(37): p. 2911-2935.

[162] Tornabene, F. and E. Viola, Free vibrations of four-parameter functionally graded parabolic panels and shells of revolution. European Journal of Mechanics - A/Solids, 2009. 28(5): p. 991-1013.

[163] Zhao, X., Y.Y. Lee, and K.M. Liew, Free vibration analysis of functionally graded plates using the element-free kp-Ritz method. Journal of Sound and Vibration, 2009. 319(3): p. 918-939.

[164] Zhao, X., Y.Y. Lee, and K.M. Liew, Mechanical and thermal buckling analysis of functionally graded plates. Composite Structures, 2009. 90(2): p. 161-171.

[165] Zhao, X. and K.M. Liew, An element-free analysis of mechanical and thermal buckling of functionally graded conical shell panels. International Journal for Numerical Methods in Engineering, 2011. 86(3): p. 269-285.

[166] Zhao, X. and K.M. Liew, Geometrically nonlinear analysis of functionally graded plates using the element-free kp-Ritz method. Computer Methods in Applied Mechanics and Engineering, 2009. 198(33): p. 2796-2811.

[167] Zhao, X., Y.Y. Lee, and K.M. Liew, Thermoelastic and vibration analysis of functionally graded cylindrical shells. International Journal of Mechanical Sciences, 2009. 51(9): p. 694-707.

[168] Lee, Y.Y., X. Zhao, and K.M. Liew, Thermoelastic analysis of functionally graded plates using the element-free kp-Ritz method. Smart Materials and Structures, 2009. 18(3): p. 035007.

[169] Hosseini-Hashemi, S., et al., Free vibration of functionally graded rectangular plates using first-order shear deformation plate theory. Applied Mathematical Modelling, 2010. 34(5): p. 1276-1291.

[170] Hosseini-Hashemi, S., M. Fadaee, and S.R. Atashipour, A new exact analytical approach for free vibration of Reissner–Mindlin functionally graded rectangular plates. International Journal of Mechanical Sciences, 2011. 53(1): p. 11-22.

[171] Zhang, W. and Y.-x. Hao, Nonlinear Dynamic of Functionally Graded Cylindrical Shells Under the Thermalmechanical Loads. 2009. p. 331-336.

[172] Alijani, F., F. Bakhtiari-Nejad, and M. Amabili, Nonlinear vibrations of FGM rectangular plates in thermal environments. Nonlinear Dynamics, 2011. 66(3): p. 251-270.

[173] Fallah, A., M.M. Aghdam, and M.H. Kargarnovin, Free vibration analysis of moderately thick functionally graded plates on elastic foundation using the extended Kantorovich method. Archive of Applied Mechanics, 2013. 83(2): p. 177-191.

[174] Kiani, Y., M. Shakeri, and M.R. Eslami, Thermoelastic free vibration and dynamic behaviour of an FGM doubly curved panel via the analytical hybrid Laplace–Fourier transformation. Acta Mechanica, 2012. 223(6): p. 1199-1218.

[175] Banijamali, S.M. and A.A. Jafari, Vibration analysis and critical speeds of a rotating functionally graded conical shell stiffened with Anisogrid lattice structure based on FSDT. Thin-Walled Structures, 2023. 188: p. 110841.

[176] Thai, H.-T. and D.-H. Choi, Improved refined plate theory accounting for effect of thickness stretching in functionally graded plates. Composites Part B: Engineering, 2014. 56: p. 705-716.

[177] Memar Ardestani, M., B. Soltani, and S. Shams, Analysis of functionally graded stiffened plates based on FSDT utilizing reproducing kernel particle method. Composite Structures, 2014. 112: p. 231-240.

[178] Isvandzibaei, M.R., H. Jamaluddin, and R.I. Raja Hamzah, Vibration analysis of supported thick-walled cylindrical shell made of functionally graded material under pressure loading. Journal of Vibration and Control, 2014. 22(4): p. 1023-1036.

[179] Su, Z., G. Jin, and T. Ye, Free vibration analysis of moderately thick functionally graded open shells with general boundary conditions. Composite Structures, 2014. 117: p. 169-186.

[180] Xiang, S., Y.-T. Chen, and G.-W. Kang, Local Collocation Method for Prediction of Natural Frequency of Functionally Graded Cylindrical Shells. Mechanics of Advanced Materials and Structures, 2015. 22(12): p. 969-977.

[181] Rezaei, A.S., et al., Natural frequencies of functionally graded plates with porosities via a simple four variable plate theory: An analytical approach. Thin-Walled Structures, 2017. 120: p. 366-377.

[182] Zhang, W., et al., A series solution for free vibration of moderately thick cylindrical shell with general boundary conditions. Engineering Structures, 2018. 165: p. 422-440.

[183] Dinh Duc, N., et al., Nonlinear Dynamic Response of Functionally Graded Porous Plates on Elastic Foundation Subjected to Thermal and Mechanical Loads. Journal of Applied and Computational Mechanics, 2018. 4(4): p. 245-259.

[184] Fan, J., et al., The Walsh series method for free vibration analysis of functionally graded cylindrical shells. Composite Structures, 2018. 206: p. 853-864.

[185] Awrejcewicz, J., L. Kurpa, and T. Shmatko, Linear and nonlinear free vibration analysis of laminated functionally graded shallow shells with complex plan form and different boundary conditions. International Journal of Non-Linear Mechanics, 2018. 107: p. 161-169.

[186] Chen, D., J. Yang, and S. Kitipornchai, Buckling and bending analyses of a novel functionally graded porous plate using Chebyshev-Ritz method. Archives of Civil and Mechanical Engineering, 2019. 19(1): p. 157-170.

[187] Trinh, M.-C., D.-D. Nguyen, and S.-E. Kim, Effects of porosity and thermomechanical loading on free vibration and nonlinear dynamic response of functionally graded sandwich shells with double curvature. Aerospace Science and Technology, 2019. 87: p. 119-132.

[188] Babaei, H., Y. Kiani, and M.R. Eslami, Large amplitude free vibrations of long FGM cylindrical panels on nonlinear elastic foundation based on physical neutral surface. Composite Structures, 2019. 220: p. 888-898.

[189] Shahbaztabar, A., et al., Free vibration analysis of FGM circular cylindrical shells resting on the Pasternak foundation and partially in contact with stationary fluid. Applied Acoustics, 2019. 153: p. 87-101.

[190] Baghlani, A., M. Khayat, and S.M. Dehghan, Free vibration analysis of FGM cylindrical shells surrounded by Pasternak elastic foundation in thermal environment considering fluid-structure interaction. Applied Mathematical Modelling, 2020. 78: p. 550-575.

[191] Liu, T., et al., Wave based method for free vibration characteristics of functionally graded cylindrical shells with arbitrary boundary conditions. Thin-Walled Structures, 2020. 148: p. 106580.

[192] Cao, Y., et al., Mechanical analysis of functionally graded spherical panel resting on elastic foundation under external pressure. Structural Engineering and Mechanics, 2020. 74(2): p. 297-311.

[193] Anamagh, M.R. and B. Bediz, Free vibration and buckling behavior of functionally graded porous plates reinforced by graphene platelets using spectral Chebyshev approach. Composite Structures, 2020. 253: p. 112765.

[194] Bagheri, H., Y. Kiani, and M.R. Eslami, Free vibration of FGM conical–spherical shells. Thin-Walled Structures, 2021. 160: p. 107387.

[195] Vinh, P.V. and L.Q. Huy, Influence of Variable Nonlocal Parameter and Porosity on the Free Vibration Behavior of Functionally Graded Nanoplates. Shock and Vibration, 2021. 2021(1): p. 1219429.

[196] Van Vinh, P. and A. Tounsi, Free vibration analysis of functionally graded doubly curved nanoshells using nonlocal first-order shear deformation theory with variable nonlocal parameters. Thin-Walled Structures, 2022. 174: p. 109084.

[197] Van Vinh, P., A. Tounsi, and M.-O. Belarbi, On the nonlocal free vibration analysis of functionally graded porous doubly curved shallow nanoshells with variable nonlocal parameters. Engineering with Computers, 2023. 39(1): p. 835-855.

[198] Kurpa, L. and T. Shmatko, Research of Vibration Behavior of Porous FGM Panels by the Ritz Method, in Selected Problems of Solid Mechanics and Solving Methods, H. Altenbach, et al., Editors. 2024, Springer Nature Switzerland: Cham. p. 325-338.

[199] Yang, J. and H.-S. Shen, Free vibration and parametric resonance of shear deformable functionally graded cylindrical panels. Journal of Sound and Vibration, 2003. 261(5): p. 871-893.

[200] Carrera, E., et al., Refined and Advanced Models for Multilayered Plates and Shells Embedding Functionally Graded Material Layers. Mechanics of Advanced Materials and Structures, 2010. 17(8): p. 603-621.

[201] Alijani, F., M. Amabili, and F. Bakhtiari-Nejad, Thermal effects on nonlinear vibrations of functionally graded doubly curved shells using higher order shear deformation theory. Composite Structures, 2011. 93(10): p. 2541-2553.

[202] Oktem, A.S., J.L. Mantari, and C.G. Soares, Static response of functionally graded plates and doubly-curved shells based on a higher order shear deformation theory. European Journal of Mechanics - A/Solids, 2012. 36: p. 163-172.

[203] Thai, H.-T. and T.P. Vo, A new sinusoidal shear deformation theory for bending, buckling, and vibration of functionally graded plates. Applied Mathematical Modelling, 2013. 37(5): p. 3269-3281.

[204] Zidi, M., et al., Bending analysis of FGM plates under hygro-thermo-mechanical loading using a four variable refined plate theory. Aerospace Science and Technology, 2014. 34: p. 24-34.

[205] Shen, H.-S. and H. Wang, Nonlinear vibration of shear deformable FGM cylindrical panels resting on elastic foundations in thermal environments. Composites Part B: Engineering, 2014. 60: p. 167-177.

[206] Tornabene, F., N. Fantuzzi, and M. Bacciocchi, Free vibrations of free-form doubly-curved shells made of functionally graded materials using higher-order equivalent single layer theories. Composites Part B: Engineering, 2014. 67: p. 490-509.

[207] Akavci, S.S. and A.H. Tanrikulu, Static and free vibration analysis of functionally graded plates based on a new quasi-3D and 2D shear deformation theories. Composites Part B: Engineering, 2015. 83: p. 203-215.

[208] Fantuzzi, N., et al., 2D and 3D shell models for the free vibration investigation of functionally graded cylindrical and spherical panels. Composite Structures, 2016. 154: p. 573-590.

[209] Tornabene, F., et al. A Numerical Investigation on the Natural Frequencies of FGM Sandwich Shells with Variable Thickness by the Local Generalized Differential Quadrature Method. Applied Sciences, 2017. 7, DOI: 10.3390/app7020131.

[210] Dong, D.T. and D. Van Dung, A third-order shear deformation theory for nonlinear vibration analysis of stiffened functionally graded material sandwich doubly curved shallow shells with four material models. Journal of Sandwich Structures & Materials, 2017. 21(4): p. 1316-1356.

[211] Wang, Y.Q. and J.W. Zu, Large-amplitude vibration of sigmoid functionally graded thin plates with porosities. Thin-Walled Structures, 2017. 119: p. 911-924.

[212] Punera, D. and T. Kant, Free vibration of functionally graded open cylindrical shells based on several refined higher order displacement models. Thin-Walled Structures, 2017. 119: p. 707-726.

[213] Chen, H., et al., Free vibration of FGM sandwich doubly-curved shallow shell based on a new shear deformation theory with stretching effects. Composite Structures, 2017. 179: p. 50-60.

[214] Mehar, K. and S.K. Panda, Thermoelastic flexural analysis of FG-CNT doubly curved shell panel. Aircraft Engineering and Aerospace Technology, 2018. 90(1): p. 11-23.

[215] Sayyad, A.S. and Y.M. Ghugal, A unified five-degree-of-freedom theory for the bending analysis of softcore and hardcore functionally graded sandwich beams and plates. Journal of Sandwich Structures & Materials, 2019. 23(2): p. 473-506.

[216] Sayyad, A. and S. Ghumare, A New Quasi-3D Model for Functionally Graded Plates. Journal of Applied and Computational Mechanics, 2019. 5(2): p. 367-380.

[217] Sayyad, A.S. and B.M. Shinde, A new higher-order theory for the static and dynamic responses of sandwich FG plates. Journal of Computational Applied Mechanics, 2021. 52(1): p. 102-125.

[218] Zuxiang, L. and T. Lihong, Semi-analytical solutions of free and force vibration behaviors of GRC-FG cylindrical shells. Steel and Composite Structures, An International Journal, 2019. 32(5): p. 687-699.

[219] Huu Quoc, T., T. Minh Tu, and V. Van Tham, Free Vibration Analysis of Smart Laminated Functionally Graded CNT Reinforced Composite Plates via New Four-Variable Refined Plate Theory. Materials, 2019. 12(22): p. 3675.

[220] Van Tham, V., T. Huu Quoc, and T. Minh Tu, Free Vibration Analysis of Laminated Functionally Graded Carbon Nanotube-Reinforced Composite Doubly Curved Shallow Shell Panels Using a New Four-Variable Refined Theory. Journal of Composites Science, 2019. 3(4): p. 104.

[221] Hong, C.-C., Vibration frequency of thick functionally graded material cylindrical shells with fully homogeneous equation and third-order shear deformation theory under thermal environment. Journal of Vibration and Control, 2020. 27(17-18): p. 2004-2017.

[222] Guellil, M., et al., Influences of porosity distributions and boundary conditions on mechanical bending response of functionally graded plates resting on Pasternak foundation. Steel and Composite Structures, 2021. 38권(1호): p. 1-15.

[223] Sayyad, A.S. and Y.M. Ghugal, Static and free vibration analysis of doubly-curved functionally graded material shells. Composite Structures, 2021. 269: p. 114045.

[224] Djilali, K., et al., An original four-variable quasi-3D shear deformation theory for the static and free vibration analysis of new type of sandwich plates with both FG face sheets and FGM hard core. Steel and Composite Structures, An International Journal, 2021. 41(2): p. 167-191.

[225] Shinde, B.M. and A.S. Sayyad, A new higher order shear and normal deformation theory for FGM sandwich shells. Composite Structures, 2022. 280: p. 114865.

[226] Rachid, A., et al., Mechanical behavior and free vibration analysis of FG doubly curved shells on elastic foundation via a new modified displacements field model of 2D and quasi-3D HSDTs. Thin-Walled Structures, 2022. 172: p. 108783.

[227] Rachid, A., et al., An analytical study of thermal environment's effect on the free vibration of FGM double curved FG shells. Mechanics Based Design of Structures and Machines: p. 1-37.

[228] Nassira, D., et al., Large cylindrical deflection analysis of FG carbon nanotube-reinforced plates in thermal environment using a simple integral HSDT. Steel and Composite Structures, An International Journal, 2022. 42(6): p. 779-789.

[229] Talebi, S., et al., Dynamic thermal buckling of spherical porous shells. Thin-Walled Structures, 2022. 172: p. 108737.

[230] Shmatko, T., L. Kurpa, and J. Awrejcewicz, Dynamic analysis of functionally graded sandwich shells resting on elastic foundations. Acta Mechanica, 2022. 233(5): p. 1895-1910.

[231] Ali, A., et al., Buckling and free vibration analysis of multi-directional functionally graded sandwich plates. Structural Engineering and Mechanics, An Int ' l Journal, 2022. 84(6): p. 813-822.

[232] Aris, H. and H. Ahmadi, Using the higher-order shear deformation theory to analyze the free vibration of stiffened rotating FGM conical shells in a thermal environment. Thin-Walled Structures, 2023. 183: p. 110366.

[233] Draiche, K., et al., An improved mathematical model for static and dynamic analysis of functionally graded doubly-curved shells. Archive of Applied Mechanics, 2024. 94(6): p. 1589-1611.

[234] Tamnar, R.B. and A.S. Sayyad, A refined shell theory considering the effects of transverse normal strain for the analysis of functionally graded porous shallow shells with double curvature. Mechanics of Advanced Materials and Structures: p. 1-17.

[235] Belhachemi, A.A., et al., Assessment of new four variables 2D and quasi-3D higher order shear theories for bending analysis of different double curved FG shells. Mechanics of Advanced Materials and Structures: p. 1-21.

[236] Daikh, A.A., et al., An Assessment of a New Hyperbolic Shear Deformation Theory for the Free Vibration Analysis of Cosine Functionally Graded Doubly Curved Shells under Various Boundary Conditions. Physical Mesomechanics, 2024. 27(3): p. 338-354.

[237] Belarbi, M.-O., et al., Nonlocal finite element model for the bending and buckling analysis of functionally graded nanobeams using a novel shear deformation theory. Composite Structures, 2021. 264: p. 113712.

[238] Hirane, H., et al., On the layerwise finite element formulation for static and free vibration analysis of functionally graded sandwich plates. Engineering with Computers, 2022. 38(5): p. 3871-3899.

[239] Belarbi, M.-O., et al., Bending and free vibration analysis of porous functionally graded sandwich plate with various porosity distributions using an extended layerwise theory. Archives of Civil and Mechanical Engineering, 2022. 23(1): p. 15.

[240] Della Croce, L. and P. Venini, Finite elements for functionally graded Reissner–Mindlin plates. Computer Methods in Applied Mechanics and Engineering, 2004. 193(9): p. 705-725.

[241] Patel, B.P., et al., Free vibration analysis of functionally graded elliptical cylindrical shells using higher-order theory. Composite Structures, 2005. 69(3): p. 259-270.

[242] Das, M., et al., A triangular plate element for thermo-elastic analysis of sandwich panels with a functionally graded core. International Journal for Numerical Methods in Engineering, 2006. 68(9): p. 940-966.

[243] Arciniega, R.A. and J.N. Reddy, Large deformation analysis of functionally graded shells. International Journal of Solids and Structures, 2007. 44(6): p. 2036-2052.

[244] Reddy, J.N. and C.D. Chin, Thermomechanical analysis of functionally graded cylinders and plates. Journal of Thermal Stresses, 1998. 21(6): p. 593-626.

[245] Kim, K.-D., L. Gilson Rescober, and S.-C. Han, Geometrically Non-linear Analysis of Functionally Graded Material (FGM) Plates and Shells using a Four-node Quasi-Conforming Shell Element. Journal of Composite Materials, 2008. 42(5): p. 485-511.

[246] Prakash, T., M.K. Singha, and M. Ganapathi, Influence of neutral surface position on the nonlinear stability behavior of functionally graded plates. Computational Mechanics, 2009. 43(3): p. 341-350.

[247] Singha, M.K., T. Prakash, and M. Ganapathi, Finite element analysis of functionally graded plates under transverse load. Finite Elements in Analysis and Design, 2011. 47(4): p. 453-460.

[248] Pradyumna, S. and J.N. Bandyopadhyay, Free vibration analysis of functionally graded curved panels using a higher-order finite element formulation. Journal of Sound and Vibration, 2008. 318(1): p. 176-192.

[249] Pradyumna, S. and J.N. Bandyopadhyay, Free vibration and buckling of functionally graded shell panels in thermal environments. International Journal of Structural Stability and Dynamics, 2010. 10(05): p. 1031-1053.

[250] Santos, H., et al., A semi-analytical finite element model for the analysis of cylindrical shells made of functionally graded materials under thermal shock. Composite Structures, 2008. 86(1): p. 10-21.

[251] Asgari, M., M. Akhlaghi, and S.M. Hosseini, Dynamic analysis of two-dimensional functionally graded thick hollow cylinder with finite length under impact loading. Acta Mechanica, 2009. 208(3): p. 163-180.

[252] Talha, M. and B.N. Singh, Static response and free vibration analysis of FGM plates using higher order shear deformation theory. Applied Mathematical Modelling, 2010. 34(12): p. 3991-4011.

[253] Yas, M.H., et al., Layer-wise finite element analysis of functionally graded cylindrical shell under dynamic load. Journal of Mechanical Science and Technology, 2011. 25(3): p. 597-604.

[254] Nguyen-Xuan, H., et al., Analysis of functionally graded plates using an edge-based smoothed finite element method. Composite Structures, 2011. 93(11): p. 3019-3039.

[255] Nguyen-Xuan, H., et al., Analysis of functionally graded plates by an efficient finite element method with node-based strain smoothing. Thin-Walled Structures, 2012. 54: p. 1-18.

[256] Cinefra, M., et al., Refined shell elements for the analysis of functionally graded structures. Composite Structures, 2012. 94(2): p. 415-422.

[257] Taghvaeipour, A., M. Bonakdar, and M.T. Ahmadian, Application of a new cylindrical element formulation in finite element structural analysis of FGM hollow cylinders. Finite Elements in Analysis and Design, 2012. 50: p. 1-7.

[258] Natarajan, S. and G. Manickam, Bending and vibration of functionally graded material sandwich plates using an accurate theory. Finite Elements in Analysis and Design, 2012. 57: p. 32-42.

[259] Kar, V.R. and S.K. Panda, Nonlinear free vibration of functionally graded doubly curved shear deformable panels using finite element method. Journal of Vibration and Control, 2014. 22(7): p. 1935-1949.

[260] Ferreira, A.J.M., Analysis of composite plates using a layerwise theory and multiquadrics discretization. Mechanics of Advanced Materials and Structures, 2005. 12(2): p. 99-112.

[261] Pandey, S. and S. Pradyumna, A new C0 higher-order layerwise finite element formulation for the analysis of laminated and sandwich plates. Composite Structures, 2015. 131: p. 1-16.

[262] Pandey, S. and S. Pradyumna, Free vibration of functionally graded sandwich plates in thermal environment using a layerwise theory. European Journal of Mechanics - A/Solids, 2015. 51: p. 55-66.

[263] Pandey, S. and S. Pradyumna, A finite element formulation for thermally induced vibrations of functionally graded material sandwich plates and shell panels. Composite Structures, 2017. 160: p. 877-886.

[264] Pandey, S. and S. Pradyumna, Analysis of functionally graded sandwich plates using a higher-order layerwise theory. Composites Part B: Engineering, 2018. 153: p. 325-336.

[265] Kar, V.R. and S.K. Panda, Geometrical nonlinear free vibration analysis of FGM spherical panel under nonlinear thermal loading with TD and TID properties. Journal of Thermal Stresses, 2016. 39(8): p. 942-959.

[266] Nasirmanesh, A. and S. Mohammadi, Eigenvalue buckling analysis of cracked functionally graded cylindrical shells in the framework of the extended finite element method. Composite Structures, 2017. 159: p. 548-566.

[267] Mehar, K. and S. Kumar Panda, Thermal free vibration behavior of FG-CNT reinforced sandwich curved panel using finite element method. Polymer Composites, 2018. 39(8): p. 2751-2764.

[268] Van Do, T., et al., Analysis of bi-directional functionally graded plates by FEM and a new third-order shear deformation plate theory. Thin-Walled Structures, 2017. 119: p. 687-699.

[269] Sushmita, D., et al., Modal analysis of FG sandwich doubly curved shell structure. Structural Engineering and Mechanics, An International Journal, 2018. 68(6): p. 721-733.

[270] Dash, S., et al., Finite element solution of stress and flexural strength of functionally graded doubly curved sandwich shell panel. Earthquakes and Structures, 2019. 16(1): p. 55-67.

[271] Pham, T.D., et al., Free vibration analysis of functionally graded shells using an edge-based smoothed finite element method. Symmetry, 2019. 11. DOI: 10.3390/sym11050684.

[272] Pham, Q.-H., et al., Geometrically nonlinear analysis of functionally graded shells using an edge-based smoothed MITC3 (ES-MITC3) finite elements. Engineering with Computers, 2020. 36(3): p. 1069-1082.

[273] Tran, T.-V., et al., An ES-MITC3 finite element method based on higher-order shear deformation theory for static and free vibration analyses of FG porous plates reinforced by GPLs. Mathematical Problems in Engineering, 2020. 2020(1): p. 7520209.

[274] Tran, T.T., P.-C. Nguyen, and Q.-H. Pham, Vibration analysis of FGM plates in thermal environment resting on elastic foundation using ES-MITC3 element and prediction of ANN. Case Studies in Thermal Engineering, 2021. 24: p. 100852.

[275] Pham, Q.-H., et al., Free vibration of functionally graded porous non-uniform thickness annular-nanoplates resting on elastic foundation using ES-MITC3 element. Alexandria Engineering Journal, 2022. 61(3): p. 1788-1802.

[276] Nguyen, P.-C., et al., Effects of partially supported elastic foundation on free vibration of FGP plates using ES-MITC3 elements. Ain Shams Engineering Journal, 2022. 13(3): p. 101615.

[277] Pham, Q.-H., T.T. Tran, and P.-C. Nguyen, Dynamic response of functionally graded porous-core sandwich plates subjected to blast load using ES-MITC3 element. Composite Structures, 2023. 309: p. 116722.

[278] Pandey, S., S. Pradyumna, and S.S. Gupta, Static and dynamic analyses of functionally graded sandwich skew shell panels. Journal of Sandwich Structures & Materials, 2021. 23(8): p. 4135-4169.

[279] Karakoti, A., S. Pandey, and V.R. Kar, Nonlinear transient analysis of porous P-FGM and S-FGM sandwich plates and shell panels under blast loading and thermal environment. Thin-Walled Structures, 2022. 173: p. 108985.

[280] Sahoo, B., et al., Nonlinear vibration analysis of FGM sandwich structure under thermal loadings. Structures, 2022.

[281] Van Vinh, P., N. Van Chinh, and A. Tounsi, Static bending and buckling analysis of bi-directional functionally graded porous plates using an improved first-order shear deformation theory and FEM. European Journal of Mechanics - A/Solids, 2022. 96: p. 104743.

[282] Nguyen, V.-C., H.-Q. Tran, and V.-V. Pham, Nonlinear static analysis of bi-directional functionally graded sandwich plates in thermal environments by a higher-order finite element model. Thin-Walled Structures, 2023. 188: p. 110819.

[283] Nguyen, V.-C., H.-Q. Tran, and M.-T. Tran, Nonlinear free vibration analysis of multi-directional functionally graded porous sandwich plates. Thin-Walled Structures, 2024. 203: p. 112204.

[284] Benounas, S., et al., Finite Element Analysis of the Free Vibration Characteristics of Power–Law, Exponential, and Sigmoid Functionally Graded Plates Under Different Boundary Conditions and Material Grades. Journal of Vibration Engineering & Technologies, 2025. 13(1): p. 137.

[285] Belarbi, M.-O., et al., An enhanced finite element model for static bending analysis of functionally graded plates with power-law, exponential, and sigmoid material gradients. Archive of Applied Mechanics, 2024. 95(1): p. 25.

[286] Jiammeepreecha, W., et al., Free vibration analysis of FGM spherical and elliptical shells under nonlinear thermal environments. Thin-Walled Structures, 2024. 196: p. 111497.

[287] Lakhdar, Z., et al., Free vibration and bending analysis of porous bi-directional FGM sandwich shell using a TSDT p-version finite element method. Acta Mechanica, 2024. 235(6): pp. 3657–3686.

[288] Zeddoune, L., S.M. Chorfi, and S.A. Belalia, Thermal buckling analysis of bi-directional FGM doubly curved shell panels using a TSDT p-version finite element method. Archive of Applied Mechanics, 2024.

[289] Belarbi, M.-O., et al., A comprehensive investigation of the bending and vibration behavior of size-dependent functionally graded nanoplates via an enhanced nonlocal finite element shear model. Mechanics Based Design of Structures and Machines: pp. 1–40.

[290] Belarbi, M.-O., et al., Bending, free vibration and buckling finite element analysis of porous functionally graded plates with various porosity distributions using an improved FSDT. Mechanics Based Design of Structures and Machines: pp. 1–45.

[291] Belarbi, M.-O., et al., Vibration of a Functionally Graded Doubly Curved Shallow Nanoshell: An Improved FSDT Model and its Nonlocal Finite Element Implement. Journal of Vibration Engineering & Technologies, 2025. 13(1): p. 93.

[292] Zenkour, A.M., Generalized shear deformation theory for bending analysis of functionally graded plates. Applied Mathematical Modelling, 2006. 30(1): pp. 67–84.

[293] Reddy, J.N., Analysis of functionally graded plates. International Journal for Numerical Methods in Engineering, 2000. 47(1–3): pp. 663–684.

[294] Pham, V.V., et al., A comprehensive analysis of in-plane functionally graded plates using improved first-order mixed finite element model. Mechanics Based Design of Structures and Machines, 2024. 52(8): pp. 5040–5070.

[295] Van Vinh, P., et al., An improved first-order mixed plate element for static bending and free vibration analysis of functionally graded sandwich plates. Archive of Applied Mechanics, 2023. 93(5): pp. 1841–1862.

[296] Reddy, J.N., Energy principles and variational methods in applied mechanics. 2017: John Wiley & Sons.

[297] Huan, D.T., T.M. Tu, and T.H. Quoc, Analytical solutions for bending, buckling and vibration analysis of functionally graded cylindrical panel. Vietnam Journal of Science and Technology, 2017. 55(5): pp. 587–597.

[298] Viola, E., L. Rossetti, and N. Fantuzzi, Numerical investigation of functionally graded cylindrical shells and panels using the generalized unconstrained third order theory coupled with the stress recovery. Composite Structures, 2012. 94(12): pp. 3736–3758.

[299] Tati, A., A five unknowns high order shear deformation finite element model for functionally graded plates bending behavior analysis. Journal of the Brazilian Society of Mechanical Sciences and Engineering, 2021. 43(1): p. 45.

[300] Benyoucef, S., et al., Bending of thick functionally graded plates resting on Winkler–Pasternak elastic foundations. Mechanics of Composite Materials, 2010. 46(4): pp. 425–434.

[301] Mechab, I., et al., A two variable refined plate theory for the bending analysis of functionally graded plates. Acta Mechanica Sinica, 2010. 26(6): pp. 941–949.

[302] Matsunaga, H., Free vibration and stability of functionally graded plates according to a 2-D higher-order deformation theory. Composite Structures, 2008. 82(4): pp. 499–512.

[303] Trinh, M.-C. and S.-E. Kim, A three variable refined shear deformation theory for porous functionally graded doubly curved shell analysis. Aerospace Science and Technology, 2019. 94: p. 105356.

[304] Chorfi, S.M. and A. Houmat, Non-linear free vibration of a functionally graded doubly-curved shallow shell of elliptical plan-form. Composite Structures, 2010. 92(10): pp. 2573–2581.

[305] Neves, A.M.A., et al., Free vibration analysis of functionally graded shells by a higher-order shear deformation theory and radial basis functions collocation, accounting for through-the-thickness deformations. European Journal of Mechanics - A/Solids, 2013. 37: pp. 24–34.

[306] Fares, M.E., et al., Bending and free vibration of multilayered functionally graded doubly curved shells by an improved layerwise theory. Composites Part B: Engineering, 2018. 154: pp. 272–284.